NASA Technical Paper 2641

April 1987

Aerothermal Evaluation of a Spherically Blunted Body With a Trapezoidal Cross Section in the Langley 8-Foot High-Temperature Tunnel

Cindy W. Albertson

NASA

NASA Technical Paper 2641

1987

Aerothermal Evaluation of a Spherically Blunted Body With a Trapezoidal Cross Section in the Langley 8-Foot High-Temperature Tunnel

Cindy W. Albertson

Langley Research Center
Hampton, Virginia

National Aeronautics and Space Administration

Scientific and Technical Information Branch

Summary

A model to be used in flow studies and thermal protection system (TPS) evaluations in three-dimensional boundary layers with pressure gradients has been tested in the Langley 8-Foot High-Temperature Tunnel at a nominal Mach number of 6.8. The purposes of the present study were (1) to define the surface pressure and heating rates at high angles of attack (in support of curved metallic TPS studies) and (2) to determine the range of conditions (particularly angle of attack) for which the model would be suitable as a test bed for aerothermal loads studies. Predictions obtained through the use of established methods were used to determine the appropriate levels and trends for evaluating the data. Angle of attack ranged from $-20.9°$ to $20.4°$, free-stream dynamic pressure ranged from 2.3 to 10.9 psia, and free-stream Reynolds number ranged from 0.4×10^6 to 1.7×10^6 ft^{-1}. The study was conducted at nominal total temperatures of 2400°R and 3300°R. For this range of test conditions, the effectiveness of boundary-layer-trip height in promoting turbulent flow was also evaluated. Most of the measurements consisted of surface pressures and cold-wall ($\approx$ 530°R) heating rates on the model. In addition, Mach number profiles within the shock layer and oil flow photographs were obtained at selected test conditions to help characterize the flow field.

The results show that for this configuration, aerothermal tests should be limited to angles of attack between $10°$ and $-10°$. This can be concluded from qualitative comparisons between predictions and the pressure and heating-rate data. This narrow range of angles of attack is a result of the long length of the model (107.63 in.). Outside this range, the effects of free-stream flow nonuniformity appear in the data. However, for TPS testing this is not a concern and tests can be performed at angles of attack between $20°$ and $-20°$. At an angle of attack of $25°$, it was found that the tunnel will unstart. Laminar and naturally turbulent boundary layers are available over limited ranges of test conditions. However, the turbulent range is extendable through the use of trips.

Introduction

Various models are used in the Langley 8-Foot High-Temperature Tunnel (8-ft HTT) as test beds for aerothermal loads studies and thermal protection system (TPS) concept evaluations. The primary model used for these tests has been the two-dimensional panel holder (refs. 1 to 4), although axisymmetric configurations have been used for aerothermal loads studies (refs. 5 and 6). A non-axisymmetric model, which is representative of the forward portion of a hypersonic lifting body, has recently been added to the family of test beds and is designated as the curved surface test apparatus (CSTA). The CSTA has been used to evaluate the curved metallic tile system shown in figure 1, and it will be used for aerothermal loads tests of the chine tile-gap heating model shown in figure 2 (ref. 7). The purpose of the present study is to measure heating-rate and pressure distributions and, through comparison with theory, assess the adequacy of the CSTA as a test bed for both detailed aerothermal loads studies and structural concept evaluations. The test was performed over a range of flow conditions and angles of attack to define the limiting conditions for both types of studies in the 8-ft HTT.

Distributions of surface pressures and cold-wall ($T_w \approx$ 530°R) aerodynamic heating rates were obtained at a nominal Mach number of 6.8 for angles of attack ranging from $-20.9°$ to $20.4°$ and for nominal total temperatures of 2400°R and 3300°R. For the methane-air test medium, these total temperatures correspond to total enthalpies of 750 and 1000 Btu/lb, respectively. Dynamic pressures ranged from 2.3 to 10.9 psia and free-stream Reynolds number ranged from 0.4×10^6 to 1.7×10^6 ft^{-1}. For this range of test conditions, the effectiveness of boundary-layer-trip height in promoting turbulent flow was also evaluated. Mach number profiles within the shock layer and oil flow photographs were obtained at selected test conditions.

Predictions, obtained by use of established methods, were used to determine the appropriate levels and trends for evaluating the data. Surface pressures and shock-layer Mach number profiles were obtained with computer code for inviscid three-dimensional flow. Laminar heat-transfer rates were obtained with an analog code for axisymmetric models, and turbulent heat-transfer rates were obtained with semiempirical methods using reference temperatures and with a turbulent-boundary-layer code.

Symbols

c_p	specific heat, Btu/lb-°R
d	boundary-layer trip diameter, in.
H	enthalpy, Btu/lb
k	thermal conductivity, Btu/ft-sec-°R
M	Mach number
$N^{\star}_{\mathrm{Pr}}$	Prandtl number based on reference temperature, $(c_p\mu/k)^{\star}$
N_{Re}	free-stream unit Reynolds number, $\rho_\infty V_\infty/\mu_\infty$, ft^{-1}

$N^{\star}_{\mathrm{Re}}$ local Reynolds number based on reference temperature, $\rho^{\star}V_e s/\mu^{\star}$

$N^{\star}_{\mathrm{St}}$ Stanton number based on reference temperature, $\dot{q}/(H_{aw} - H_w)\,\rho^{\star}V_e$

p pressure, psia

q dynamic pressure, psia

$\dot{q}$ heat flux, Btu/ft^2-sec

r, β, x cylindrical coordinates (see fig. 17)

$\bar{r}, \beta, \theta$ spherical coordinates (see fig. 17)

r_n nose radius, in.

s surface distance from stagnation point on centerline axis (see fig. 9(b)), in.

T temperature, °R

V velocity, ft/sec

y distance normal to model surface (see fig. 8), in.

z distance normal to tunnel centerline (see fig. 14), in.

α angle of attack (see fig. 9(b)), deg

γ ratio of specific heats

δ calculated laminar boundary-layer height at trip location, in.

μ viscosity, lb/ft-sec

ρ density, lb/ft^3

Subscripts:

aw adiabatic wall

b model base

c combustor

e edge of boundary layer

m minimum surface pressure

s stagnation

t total condition of tunnel (combustor)

w model wall

∞ free stream

$t2$ stagnation behind normal shock

Superscript:

$\star$ condition at Eckert's reference temperature (see eq. (2)), described in reference 6

Apparatus and Tests

Model

The model used for the present study (fig. 3) is 107.63 in. long and 36.28 by 24.20 in. at the base. The nose of the model is made of copper and is spherical with a 3.00 in. radius. The model has surface angles of 8.2° and 5.0°, as shown in the top and side views in figure 3. The cross section geometry varies along the length of the model as follows. From $x = 0$ to 2.57 in. (section A-A), the cross section is circular. Because of the difference in top and side surface angles, the side flat surfaces begin ahead of the top and bottom flat surfaces. Therefore, from $x = 2.57$ to 2.74 in. (section B-B), the cross section is defined by two nearly circular arcs with straight lines on either side. The top and bottom flat surfaces begin at $x = 2.74$ in. and the cross section is defined by four nearly circular arcs separated by four straight lines through $x = 107.63$ in. (section C-C). Pertinent dimensions of each cross section are tabulated in figure 3.

A photograph of the model in the 8-ft HTT is shown in figure 4 and a sketch of the model structural components is shown in figure 5. The test surface is constructed of 0.375-in-thick nickel with a surface roughness of 0.125×10^{-6} in. rms. Contour measurements were taken of each cross section at which the model was instrumented for heat-transfer measurements. Comparisons with design indicate that the surface contour does not vary more than 0.05 in. measuring normal from the model axis to the surface. For this study the back side of the test surface was uninsulated. As shown in figure 5, the test surface is divided into forward and aft sections at a bulkhead ($x/r_n = 15.2$) where a 0.5-in-thick steel inner support structure (or strongback) is attached. This support structure is also attached to the aft test surface along its length through standoff assemblies with no rotational restraint. Therefore, both forward and aft test surfaces are free to expand thermally from the bulkhead. A hinge plate at the base of the support structure allows the model to be opened for access to instrumentation located in the interior (fig. 6). A space of approximately 4.0 in. exists between the strongback and the outer mold line of the test surface to allow access to surface-mounted instrumentation and installation of structural concepts such as the metallic TPS shown in figure 1. The base of the model is covered by a plate to protect instrumentation and wires from the recirculating hot gases in the base region (fig. 5). Holes (1.0 in. in diameter) are drilled into the base plate to allow the interior of the model to vent during testing.

The boundary-layer trips consisted of stainless steel spheres located at $x = 2.99$ in. as shown in figure 7. For a given test condition, the same trip diameter was used around the circumference of the model. Two trip diameters, 0.094 and 0.190 in., were used. These trip diameters were between one and three times the laminar boundary-layer thickness at the trip location along the pitch plane at $\beta = -90°$. (See front view, fig. 3.) The boundary-layer thickness at the trip location was calculated along the pitch plane with the method described in references 8 and 9. The trips were spaced four sphere diameters apart, center to center, around the circumference of the model. Trip size and spacing were based on the results from reference 10.

The pitot pressure rake shown in figure 8 was used to survey the flow within the shock layer. The rake consists of seven probes which were aligned parallel with the model surface. The inside diameter (I.D.) and outside diameter (O.D.) of each probe are 0.040 and 0.060 in., respectively, and the average tube length is 36.0 in. The rake was mounted such that the ends of the pitot tubes were aligned normal to the test surface at the same axial location as the static pressure orifice ($x/r_n = 34.54$ orifice number 54 or 68, depending on rake location) and at the same circumferential distance from the windward symmetry line, as shown in figure 8. The rake was always located on the windward side of the model.

Instrumentation

The surface instrumentation for the model included 69 pressure orifices (fig. 9(a)) and 68 heat flux sensors (fig. 9(b)). The coordinates of the instrumentation are given in tables I and II. The axial coordinate x and the circumferential coordinate β are defined in figure 9(a). Stagnation heating rates were obtained from a single heat flux sensor mounted in the nose on the centerline of the model, as shown in figure 10. Stagnation pressures were obtained from the pressure orifice tubes located in the pitch plane 15° above and below the centerline. The remaining pressure orifices and heat flux sensors were paired such that the pressure orifices were located 1.0 in. upstream of the heat sensors (fig. 11).

The pressure tubing measured 0.090 in. O.D. and 0.060 in. I.D. Each tube was no more than 36.0 in. in length and was connected to a strain-gage-type pressure transducer located inside the model. Additional pressure gages were located inside the model to monitor interior pressures. To measure wall temperatures, 12 chromel-alumel 30-gage thermocouples were spot-welded to the inside surface. The coordinates of these thermocouples are given in table III.

The Gardon-type heat flux sensors used in the present study were installed such that the sensor surface was mounted flush with the model surface. (See fig. 11.) The body of each sensor was threaded directly into the test surface to ensure good thermal contact. The sensors were sealed on the inside of the model surface with RTV[1] silicone rubber to prevent leaks around the threads of the sensors. A schematic of the sensors is shown in figure 12. The heat flux incident on the surface of the chromel foil disk is conducted radially to the nickel heat sink body and causes the temperature at the center of the disk to rise above the edge temperature. This temperature difference is directly proportional to the incident heat flux and is measured by constantan center and edge wires which form relative hot and cold thermocouple junctions with the chromel foil. Gardon-type sensors are typically used without active cooling in walls which behave as heat sinks; that is, the wall temperature does not rise appreciably. However, they can be calibrated over a range of wall temperatures, as was done for the present test series. More details about the principles of operation are given in reference 11. The sensors used for the present tests were 1.000 in. long and 0.312 in. in diameter. The radii of the sensing disks were 0.091 and 0.041 in. for the 15 and 60 Btu/ft^2-sec sensors, respectively.

Oil flow patterns were obtained as an aid in interpreting pressure and heating-rate data through use of a mixture of silicone oil (having a viscosity of 350 centistokes) and titanium dioxide. Photographs were taken after the model was withdrawn from the test stream.

Test Facility

The Langley 8-Foot High-Temperature Tunnel, shown schematically in figure 13, is a hypersonic blowdown wind tunnel which operates at a nominal Mach number of 7 and simulates pressure altitudes between 80 000 and 120 000 ft. The high-energy test medium is obtained by burning a mixture of methane and air under high pressure in the combustor. The combustion products are expanded to the test chamber Mach number by means of an axisymmetric conical contoured nozzle having an exit diameter of 8 ft. The stream in the test chamber is a free jet which enters a straight tube supersonic diffuser where it is pumped to the atmosphere by means of a single-stage annular air ejector. The tunnel operates at total temperatures from 2300°R to 3600°R, at free-stream dynamic pressures from 1.7 to 12.5 psia, and

[1] RTV: Family of silicone rubber manufactured by General Electric Co.

at free-stream Reynolds numbers from 0.3×10^6 to 3.0×10^6 ft^{-1}. The maximum run time is 120 sec.

The model is stored in the pod below the test section during tunnel start-up and shutdown to minimize loads (fig. 14). Once flow conditions are established, the model is inserted into the stream on a hydraulically actuated elevator. The insertion time from the edge of the flow to the tunnel centerline for the present model is typically 1.3 sec. For this study, the tip of the model was positioned 0.5 ft downstream of the nozzle exit at 0° angle of attack. Additional details of this test facility may be found in reference 12.

Test Conditions and Procedures

The tests were conducted by starting the tunnel while the model was held out of the stream in the pod below the test section. The model was at ambient temperature (about 530°R) prior to entering the stream since cold-wall heating rates were to be obtained. This was confirmed by temperature measurements obtained from thermocouples spot-welded to the inside surface of the model. Once flow conditions were established, the model was pitched to the desired angle of attack and inserted into the stream. Exposure time in the stream (see fig. 15) was generally limited to 10 sec to avoid overheating the heat flux sensors. This length of time was sufficient for the outputs of all pressure transducers to stabilize. For certain runs in which the heating rates were expected to be relatively low (exposure times lasting up to 26 sec), the model was pitched through a series of angles of attack. The model was held at each angle of attack long enough for the pressures and heating rates to stabilize (about 7 sec). The model was then withdrawn from the stream prior to tunnel shutdown. Nominal time histories indicating when the data were taken is shown for both single and multiple angle of attack exposures in figure 15.

During the latter part of the present study, test section flow surveys were obtained. However, the survey rake used was not fully operational at that time; therefore, only a limited amount of information, in the form of pitot pressure distributions, was obtained. Surveys were typically taken after the model had returned to the pod.

The model was tested at a total of 39 test conditions, as summarized in table IV, with and without boundary-layer trips. The run numbers given in the table include the test series number for the facility (99) and the run number in the series. A letter following the run number indicates that the angle of attack was varied during the run. (For example, the letter "A" indicates the first angle of attack for a given run.) Angle of attack was varied from −20.9° to 20.4° and free-stream Reynolds number was varied from about 0.4×10^6 to 1.7×10^6 ft^{-1}. The model was tested at nominal total temperatures of 2400°R and 3300°R. More details of each run are given in table V. Free-stream unit Reynolds number, dynamic pressure, and Mach number were calculated with measured pressures and temperatures from test section flow surveys and the thermodynamic and transport properties of methane-air combustion products (ref. 13). Because the test section flow survey data obtained during the present study were limited to pitot pressures, previous test section flow surveys (e.g., test 44, ref. 12) in which pitot pressures, static pressures, and total temperatures were obtained over a wide range of flow conditions were used to calculate free-stream unit Reynolds number, dynamic pressure, and Mach number. The nominal data selection time is also given in table V.

The pitot pressure distributions across the test stream obtained from flow surveys during test 44 of reference 12 and during the present test series (test 99) are shown in figure 16. Pressures measured on the nose of the model and corrected to the stagnation point value by use of the modified Newtonian pressure law (ref. 14) are also shown. The pressures were normalized by total pressure measured in the combustor. A parallel scale is presented that relates the model angle of attack to the distance z from the tunnel centerline to the model stagnation point. Test 44 and test 99 surveys were made 20 and 12 in. from the nozzle exit plane, respectively. The data from the nose of the model were measured from 6 to 17 in. from the nozzle exit plane, depending on angle of attack. The survey data shown were obtained at $N_{\mathrm{Re}} = 1.5 \times 10^6$ ft^{-1}, which was one of the higher Reynolds numbers for the present study. The survey data indicate a uniform test core of about 24 in. in diameter. Data from the nose of the model are shown for three different free-stream unit Reynolds numbers, but these data show very little Reynolds number effect. Overall, the results indicate that at small angles of attack, the model stagnation point moves out of the uniform pitot pressure test core. This is because of the long length of the model (107.63 in.). Differences between flow surveys, which were obtained at different distances from the nozzle exit plane, and model nose data are a result of the flow continuing to expand past the nozzle exit plane. The Mach number distributions given in reference 12 are relatively uniform across 36 in. in diameter, although the static pressure distributions show a variation which is similar to the pitot pressure variation.

Data Reduction and Uncertainties

Pressure transducer, heat flux sensor, and thermocouple outputs were recorded at a rate of 20 frames per second with a digital data recording system. The signals from the sensors were filtered with 10-Hz low-pass filters and digitized prior to being recorded on magnetic tape. A more detailed description of the equipment is given in reference 6.

Pressure data were obtained with strain-gage transducers having nonlinearity errors of less than 0.25 percent of full scale. Gage ranges were selected to be compatible with anticipated measurements. The full-scale values of the gages used were 1, 3, and 5 psia for surface pressure measurements, 25 psia for the pressure measurements on the nose of the model, and 100 psia for the pitot pressure rake measurements within the model shock layer. These values correspond to nonlinearity errors of no more than 0.0025, 0.0075, 0.0125, 0.0625, and 0.2500 psia, respectively. To correct for gage offset, all surface pressure measurements were adjusted to equal measurements from a precision low-pressure gage (mounted in the tunnel pod) made prior to model insertion into the flow. (Checks of pod pressure variation with location made during previous tests in the 8-ft HTT showed no appreciable variation.) This affected only a small number of measurements, in particular some leeward-side measurements obtained at high angles of attack and low combustor pressures. The gages used for pitot pressure measurements were corrected to the barometric pressure prior to tunnel start-up. Overall, the uncertainty of the windward-side pressure measurements was less than ± 1 percent.

Heating rates were obtained from Gardon-type heat flux gages. Possible sources of heating rate errors included errors associated with the time response of the gages, the determination of the calibration constant accurately, the alignment of the sensor surface properly with the model surface, and the heating-rate deviations from the cold-wall values. The error associated with the time response of the gages was considered insignificant because the data were selected after the output of the gages had stabilized. The time constants for the gages were 0.008 sec for the 60 Btu/ft^2-sec sensors and 0.25 sec for the 15 Btu/ft^2-sec sensors.

The gage calibration repeatability error is considered to be one of the largest errors affecting heating rates measured using these gages. Primary factors of concern include the uniformity of the radiant furnace used to calibrate the gages, possible variance of the calibration standard, and emissivity matching errors between the gages and the calibration standard. An attempt is made to match emissivity by coating the sensor surface of each gage with soot prior to calibration. For the present study, the average change in the calibration constant of the gages performed before and after the study was 2.8 percent, with a standard deviation of ± 3.0 percent.

Another source of error is possible surface misalignment effects associated with gage installation. A numerical assessment of this error is not currently available, but the errors were minimized as much as possible. The sensor surface was installed flush with the model surface; however, because the threads used for installation extend the full length of the sensor (see figs. 11 and 12), a groove was present around the edges of the sensor. The surface irregularity effects of the groove were minimized by filling the region with ceramic. In addition, the 60 Btu/ft^2-sec sensors were manufactured with a 0.005-in. protrusion of the sensor surface. The effects of this irregularity were minimized by installing the sensor flush with the model surface.

The heating rates measured with the Gardon-type gages corresponded to a model surface temperature which was generally above the cold-wall value ($T_w \approx 530°$R). Actual measurements of the outer-surface temperature were not available; however, temperatures on the inside surface of the model were measured at a limited number of locations. (See table III.) To estimate the outer-surface temperature, the finite-element thermal analysis program described in reference 15 was used along with the temperatures measured on the inner surface. However, these values were only used to give an estimate of how close the measured heating rates were to the cold-wall heating rates and were not used to correct the data because the thermocouples were sparsely located and because of additional inaccuracies imposed by the technique. For the exposure runs at a single angle of attack, the percent difference between cold-wall and measured heating rates along the windward symmetry line was estimated to be no more than -2.0 percent because the data were selected as soon as the model was on the flow centerline and the readings had stabilized (approximately 1.5 sec). The errors for the runs at multiple angles of attack, conducted at a nominal total temperature of 3300°R, ranged from -0.1 to -5.0 percent, depending on exposure time and test conditions. The maximum errors for the runs at multiple angles of attack conducted at a nominal total temperature of 2400°R ranged from -5.0 to -10.0 percent. However, there were few of these runs and the data were not used for determining the range of test conditions at which the model would be suitable as a test bed for aerothermal loads studies. None of the data presented was corrected

to cold-wall temperatures ($T_w \approx 530°R$) because the temperature measurements were sparse.

All pressures and heating rates presented were normalized by the stagnation-point values. To obtain stagnation-point pressures, the pressures measured in the nose region above and below the stagnation point were corrected with the modified Newtonian pressure law (ref. 14). Stagnation-point heating was measured with a heat flux sensor located in the nose of the model. However, the sensor output became erratic after the first few runs, apparently because of the impingement of particles carried by the flow (indicated by pitting and erosion on the sensor surface). Therefore, the heating-rate measurements from the sensor were not used to normalize the data. The stagnation-point heating rates used for normalization were calculated from the corrected stagnation pressure measured on the model, the total temperature measured in the combustor, and the theory of Fay and Riddell (ref. 16) with the properties of methane-air combustion products. A comparison between the measured stagnation-point heating rate with that predicted with the Fay and Riddell theory for the first few runs (before the sensor at the stagnation point become severely damaged) agreed within 5 percent.

Shock-layer Mach numbers were calculated from static and pitot pressure measurements by use of the Rayleigh pitot formula with $\gamma = 1.38$. The pitot pressures were obtained from a pitot rake and the static pressures were obtained from a static pressure orifice at the wall of the model. It was assumed that the static pressure variation was negligible across the height of the rake, which is a good assumption for the range of angles of attack considered, according to the inviscid calculations. For example, at $\alpha = 15°$, the inviscid predictions indicated a static pressure variation of 1.1 percent across the height of the rake. Mach number uncertainties ranged from ± 0.3 percent near the wall to ± 0.1 percent at the top of the rake for angles of attack of 15.0° and −14.8° (runs 99-7 and 99-31, respectively). The corresponding Mach number uncertainty at $\alpha = 0°$ (run 8) ranged from ± 6.0 to ± 0.9 percent. Mach number uncertainty decreased with increasing distance from the wall.

Prediction Methods

Predictions of surface pressures, heating rates, and Mach number profiles through the shock layer were obtained by use of inviscid-flow-field and axisymmetric analog methods (refs. 8, 9, and 17 to 20) and by use of a semiempirical method for turbulent boundary layers (refs. 21 to 23). For the laminar flow data (run 99-21A), predictions (documented in ref. 24) from a parabolized Navier-Stokes code developed by Li (refs. 25 to 27) are compared with measurements.

Inviscid-Flow-Field and Axisymmetric Analog Methods

Predictions were obtained through use of a computer code which computes the outer inviscid flow field and another code which predicts the boundary-layer flow properties. Perfect-gas thermodynamic and transport properties for air at $\gamma = 1.4$ were used in the analysis. For the nominal flow condition, the calculated free-stream Mach number, Reynolds number, static pressure, and static temperature were 6.8, 1.4×10^6 ft^{-1}, 0.29 psia, and 400°R, respectively. Calculations were performed for angles of attack of −15°, −5°, 0°, 5°, and 15°. These calculations were done prior to the present test series and the results were used to help select gage ranges and locations. The calculations were not repeated after the test series because predicted trends are more important than exact levels for evaluating the data. Pressures and heating rates were nondimensionalized by the stagnation-point values. The stagnation-point heating rate was calculated from the theory of Fay and Riddell (ref. 16) with the properties for air. The total enthalpy (1000 Btu/lb) used in the analysis corresponded to that for methane-air combustion products at a total temperature of 3300°R.

The inviscid flow field was obtained by first computing the subsonic-transonic flow over the nose of the model with the BLUNT code (ref. 17). This code uses a time-asymptotic technique to integrate the three-dimensional, time-dependent Euler equations. The solution was continued downstream, where the local flow is supersonic, with the STEIN (supersonic three-dimensional external inviscid) code (refs. 18 and 19) to integrate the three-dimensional, steady-state Euler equations.

The coordinate system used for the computational grid is shown in figure 17. As indicated in the figure, only half the flow field was computed because of model symmetry about the pitch plane. The BLUNT code was used from the stagnation point to $x/r_n = 0.7$, where the axial Mach number was sufficiently supersonic. The grid specified in this region was $11 \times 9 \times 19$ points in the $\bar{r}$-, β-, and θ-directions, respectively. At $x/r_n = 0.7$, an 11- × 19-point starting plane grid in the r- and β-directions was specified for the supersonic inviscid solution. The grid was increased to 21 points in the $\bar{r}$-direction at $x/r_n = 1.5$ and to 60 points in the β-direction at $x/r_n = 2.0$. For $\alpha = 0°$, 100 points were needed in the β-direction to provide a good solution.

Heat-transfer distributions on the model were obtained from two separate codes for the laminar and turbulent calculations. Surface pressures and velocity vectors from the inviscid analysis were used as inputs to a code which calculated laminar heating rates (ref. 20) with a code based on the axisymmetric analog method developed by Cooke (ref. 28). Boundary-layer edge properties for the heat-transfer calculation were obtained with the assumption of isentropic flow from the stagnation point. The inviscid velocity vectors were used to calculate streamlines and metric coefficients along the body. Heating rates were calculated along streamlines with the axisymmetric analog approach. Rather than solving the complete axisymmetric boundary-layer equations, an approximation technique described in appendix C of reference 20 was used to calculate laminar heating rates.

Since these relations apply only to laminar boundary layers, a second code described in references 8 and 9 was used to calculate heating rates for turbulent boundary layers. This code uses the local radii of curvature and pressures from the inviscid solution to calculate the edge conditions (again with the assumption of isentropic flow from the stagnation point) needed to solve the equations for turbulent axisymmetric boundary-layers along a streamline.

Semiempirical Method for Turbulent Boundary Layers

Because the turbulent-boundary-layer code (refs. 8 and 9) tended to underpredict heating rates for both this and a previous study in the 8-ft HTT (ref. 6), a second approach based on the semiempirical method discussed in references 21 to 23 was used. This method was only used to calculate heating rates along the windward symmetry line because of the difficulty in defining the local surface angle to the flow away from this region. Also the method assumes low cross-flow and pressure gradients and would therefore be inaccurate away from the windward symmetry line. This method relates Stanton number to Reynolds and Prandlt number as shown below:

$$N^{\star}_{\mathrm{St}} = C(N^{\star}_{\mathrm{Pr}})^{-2/3}(N^{\star}_{\mathrm{Re}})^{-1/5} \qquad (1)$$

Reynolds number was calculated with the wetted distance along the windward symmetry line originating from the geometric stagnation point. Here $C = 0.0296$ for flat plate flow and 0.0348 for conical flow. The * signifies that the gas properties were evaluated at Eckert's reference temperature $T^{\star}$, given by

$$T^{\star} = T_e + 0.50(T_w - T_e) + 0.22(T_{aw} - T_e) \qquad (2)$$

Heating rates can be calculated from the Stanton number as follows:

$$\dot{q} = N^{\star}_{\mathrm{St}}(H_{aw} - H_w)\rho^{\star}V_e \qquad (3)$$

Through use of the thermodynamic and transport properties of methane-air combustion products, the edge and reference temperature properties for equations (2) and (3) were obtained for the following two cases: (1) the flow follows a streamline isentropically from the stagnation point on the model to the local static pressure predicted by the inviscid code, and (2) the flow is conical with no entropy gradient.

Discussion of Results

The results consist primarily of longitudinal and circumferential distributions of surface pressures and heating rates measured on the model. Predicted values are presented where appropriate to compare with the measured data and to assist in characterizing the flow field around the model. A limited number of Mach number distributions, inferred from pitot pressure surveys, and oil flow photographs also were obtained to help characterize the flow field, and these results are presented first. The pitot pressures and computed Mach numbers are presented in table VI. Next, surface pressure and heating-rate data are presented in overview format to characterize and validate data trends through comparisons with theory. The surface pressure and heating-rate data for each run are presented in tables VII and VIII, respectively. Detailed results of the effects of boundary-layer trips, Reynolds number, and angle of attack are discussed in subsequent sections. In addition, correlations of the effects of total temperature, of Reynolds number, and of angle of attack on heating rates are presented.

Shock-Layer Flow Field

Mach number distributions. Mach number distributions (fig. 18) are plotted as a function of the distance normal to the surface of the model at $x/r_n = 34.54$. The data presented are for a tripped boundary layer (0.094-in-diameter trips) at $N_{\mathrm{Re}} = 1.5 \times 10^6$ ft^{-1}. The data are generally smooth, showing no discontinuities in the shock-layer flow field (at least within about 3 in. normal to the model surface). The predicted Mach number distributions shown in figure 18 are from the inviscid calculations (ref. 19) with a constant γ of 1.4, which is within about 1 percent of the free-stream value of γ for the 8-ft HTT. Estimates of laminar and turbulent boundary-layer thickness at the rake location were obtained from boundary-layer calculations with the

code described in reference 9. Agreement with theory is best at the higher angles of attack ($\alpha = 15.0°$ and $-14.8°$). This agreement is attributed, in part, to thinning of the boundary layer. Based on the results of reference 6, better agreement between data and predictions at the intermediate angles of attack probably could be obtained through use of an effective γ in the inviscid codes based on the normal-shock density ratio.

Predicted surface streamlines and oil flow photographs. Streamlines obtained from inviscid predictions are shown for $\alpha = 0°$, $5°$, $-5°$, $15°$, and $-15°$ in figure 19 to give a qualitative indication of flow behavior over the model. Front views are shown; therefore, the free-stream velocity vector is directed into the page at the angle of attack indicated. The oil flow photographs obtained during the present test series were generally limited to a small portion of the model and a limited number of patterns were successfully obtained; hence, only a sample obtained at $\alpha = 15.0°$ is shown (see fig. 20).

The streamlines shown generally show a shift in streamline divergence with angle of attack. At $\alpha = 0°$ (fig. 19(a)), the streamlines diverge from the small-chine region and flow around into the other regions of the model. The streamlines at $\alpha = 5°$ (fig. 19(b)) show similar behavior, except the line of streamline divergence has shifted around the small-chine region slightly. At $\alpha = 15°$ (fig. 19(c)), the streamlines diverge from the tangent line between the large-flat and small-chine regions of the model and flow around the small-chine, side-flat, and large-chine regions. The streamlines then coalesce along the tangent line between the large-chine and small-flat regions. However, the solution is probably no longer valid in this region because of boundary-layer separation. This suspicion is confirmed by the oil flow photograph in figure 20, which indicates cross-flow separation in the large-chine region. The oil flow pattern shown is presumed to be unaffected by the tunnel shutdown process because the oil streaks show no sudden change in direction along their length.

At $\alpha = -5°$ (fig. 19(d)), the divergence has shifted into the large-chine region. At $\alpha = -15°$ (fig. 19(e)), streamlines appear to diverge from the windward symmetry line, flow around the small-flat, large-chine, side-flat, and small-chine regions and coalesce in the large-flat region. Again the solution is probably no longer valid in this region because of separation.

Pressure Distributions

Measured and predicted axial and circumferential surface pressure distributions at $N_{Re} = 1.5 \times 10^6$ ft^{-1} normalized with the stagnation point values are presented for various angles of attack in figure 21. Inviscid predictions (ref. 19) were only obtained for $\alpha = 0°$, $5°$, $-5°$, $15°$, and $-15°$ and for a nominal free-stream Mach number of 6.8. For the data presented, the free-stream Mach number was about 6.5 and there were slight differences in angles of attack between data and theory for some cases presented. Therefore, there should be slight differences in pressure levels between data and theory; however, qualitative comparisons can still be made. Tangent cone and tangent wedge predictions (ref. 29) are also presented in the windward axial distribution plots for each angle of attack to help evaluate the overall pressure levels. Data from a second ray of orifices, the location of which is given in figure 22, are also presented in the figure. The pressure levels measured in the base region of the model are also shown in the circumferential plots for $\alpha \geq |10°|$ to help evaluate any base pressure effects on the data. For $\alpha < |10°|$, the base pressure is below the scale of the plots.

For angles of attack between $5°$ and $-5°$ (figs. 21(a) to 21(c)), the measurements agree reasonably well with the longitudinal distributions of inviscid predictions and the data of ray 2 are supportive of the data of ray 1. The asymptotic levels of both the data and the inviscid predictions agree best with tangent cone predictions, indicating that the flow is more conical than wedge-like. Some data scatter is evident in the axial distributions at $\alpha = 0°$, but the data generally show the proper trend. The measured axial distributions of pressure for $\alpha = 4.8°$ are below predictions, but the data points again show the proper trend. For this case, the difference in levels between data and theory is probably due to differences in free-stream Mach number and angle of attack. The measured axial distributions obtained at $\alpha = -4.8°$ are more sparse and are scattered about the predicted inviscid pressure line. In the measured axial pressure distributions for $\alpha = 9.7°$ (fig. 21(d)), a decrease in pressure, which is uncharacteristic of spherically blunted bodies, is indicated by the two data points at $x/r_n = 16.54$ and 21.04 along ray 1. At $\alpha = -9.7°$ (fig. 21(e)), both rays show smooth levels just below the tangent cone prediction. At $\alpha = 15.0°$ (fig. 21(f)), however, the data along ray 1 show a greater decrease in pressure at $x/r_n = 16.54$ and 21.04 than do the $\alpha = -9.7°$ data, a trend which is supported by the data along ray 2. This decrease is also evident, but to a lesser degree, in the data obtained at $\alpha = 14.8°$, $20.4°$, and $-20.9°$ (figs. 21(g) to 21(i)). One cause for this behavior may be that as angle of attack is increased, the model is exposed to larger variations in free-stream pitot pressure. (See fig. 16.) When the model is at relatively low angles of

attack, it is exposed primarily to a relatively uniform pitot pressure distribution.

The measured circumferential pressure distributions are generally smooth and agree reasonably well with the predicted distributions in windward regions, where the boundary layer is attached. The measurements obtained in relatively leeward regions of the model for $\alpha = 4.8°$, $-4.8°$, $9.7°$, $15.0°$, $20.4°$, and $-20.4°$ show a gradient reversal which, if sufficiently large, would indicate cross-flow separation. Oil flow patterns are only shown for $\alpha = 15.0°$, and separation is indicated for this angle of attack (fig. 20). Although the trends are generally what one would expect, base pressure may influence the leeward-side flow for $\alpha = 9.7°$, $15.0°$, $20.4°$, and $-20.9°$, since the base pressure levels are equal to or higher than the leeward-side pressures. The trends obtained for $\alpha = -14.8°$ and $-9.7°$ show a much more pronounced effect of base pressure on the leeward-side data. For these two cases, the pressures measured on the leeward side are nearly at the same level as the pressures along the side flat area of the model. The base pressure measured during these two runs exceeds the full-scale range of the transducer; therefore, these pressures are actually higher than what is indicated.

These surface pressures indicate that the model is suitable for detailed aerothermal loads testing for nominal angles of attack between $-10°$ and $10°$. Above $\alpha = |10°|$, the axial pressure distributions show effects of variation in the free-stream pitot pressure.

Heating-Rate Distributions

Turbulent-boundary-layer heating rates. Measured and predicted axial and circumferential heating-rate distributions at $N_{Re} = 1.5 \times 10^6$ ft^{-1} normalized with the stagnation point values are presented for various angles of attack in figure 23. For the data presented, the boundary layer was tripped and appears to be turbulent in the attached-flow region in the aft section ($x/r_n \geq 16.88$) of the model. Turbulent-boundary-layer predictions (ref. 9) were only obtained at selected angles of attack (i.e., at $\alpha = 0°$, $5°$, $-5°$, $15°$, and $-15°$) and generally tended to underpredict the measurements. This discrepancy tended to increase with increasing angle of attack. For this reason, predictions were also obtained with the turbulent-boundary-layer semiempirical method for the following two inviscid flow cases: (1) the flow expands isentropically from the stagnation point to the surface pressure predicted by STEIN (ref. 19), and (2) the flow is conical, with no cross flow in the shock layer and no entropy gradient (sharp cone theory). The assumption of conical flow was chosen over wedge flow because the pressure data show better agreement with this assumption. To assist in evaluating the data, data from an adjacent ray (the general location of which is shown in fig. 22) are given in the axial distributions of heating rates.

In the axial distribution at $\alpha = 0°$ (fig. 23(a)), the data along ray 1 appear smooth and fall between the turbulent-boundary-layer predictions and the semiempirical isentropic expansion predictions. The data along ray 2 show an upward trend with increasing x/r_n, and this trend is due to the circumferential gradient in heating rates. At $\alpha = 4.8°$ (fig. 23(b)), the data along ray 1 initially follow the isentropic expansion prediction and then slowly approach the sharp cone predictions. This same trend in the data can also be observed in figure 23(c) for $\alpha = -4.8°$. The most probable reason for this behavior is entropy-layer swallowing by the boundary layer, a phenomenon which is not taken into account by any of the theories used. Entropy-layer swallowing can be described as follows. As the boundary layer grows along the surface of the model, an increasing amount of mass crossing the edge of the boundary layer is near the entropy level corresponding to the sharp cone case. As distance from the leading edge continues to increase, the mass which crosses the normal portion of the shock eventually washes out of the boundary layer. As this happens, the heating rates measured on the model slowly approach the level predicted with the sharp cone theory. The data obtained at $\alpha = 9.7°$ and $-9.7°$ (figs. 23(d) and 23(e), respectively) also show entropy-layer swallowing, and the swallowing appears to be complete closer to the nose. At $\alpha = 15.0°$ and $-14.8°$ (figs. 23(f) and 23(g)) the measured heating rates show an unusual increase in heating with increasing axial distance, and these rates are well above all predictions. This high level of heating is shown by the data obtained at $\alpha = 20.4°$ and $-20.9°$ (figs. 23(h) and 23(i)) as well. Note that as angle of attack increases, circumferential heating-rate gradients on the windward surface decrease, and the axial distributions along rays 1 and 2 tend to follow each other more closely.

The semiempirical method is limited to regions where the cross flow is low and where the angle to the flow can be easily defined. Therefore, it was not used to obtain circumferential distributions. However, the turbulent-boundary-layer code shows good agreement with the trends in the circumferential data distributions. As expected, the circumferential heating-rate data distributions show trends similar to the pressure data distributions, particularly in attached-flow regions. At $\alpha = 20.4°$ and $-20.9°$, windward- and leeward-side heating rates vary by as

much as two orders of magnitude. In the separated-flow regions, the pressure and heating rate minimums do not necessarily correspond to the same locations on the model. The experimental heating rates obtained at $\alpha = -9.7°$ and $-14.8°$ show the effects of high pressure in the base region of the model feeding forward into the leeward-side region, similar to the trends shown by the pressure distributions.

The above trends in both the axial pressure and heating-rate data show that the model is suitable for use as an aerothermal test bed, but tests should be limited to $\alpha < |10°|$. Above $\alpha = |10°|$, the axial distribution of data shows effects of variations in the free-stream pitot pressure. However, for TPS testing this is not a concern, and the model can be tested up to $\alpha = |20°|$. At $\alpha = 25°$, it was found that the tunnel will unstart.

Laminar heating rates. Measured heating rates are compared with predicted heating rates from two laminar flow methods at $\alpha = 0.4°$ and $N_{\mathrm{Re}} = 0.4 \times 10^6$ ft^{-1}. One prediction is from the axisymmetric analog method of Hamilton (ref. 20), and the other is from the parabolic Navier-Stokes (PNS) method developed by Li (refs. 25 to 27). These results were previously documented in reference 24, but are included here for completeness.

In the axial heating-rate distributions (fig. 24), measured heating rates are shown with predictions from both the axisymmetric analog method and the PNS code. The measured heating rates appear to be laminar up to $x/r_n = 25.9$ for both $\beta = -90°$ and 90°. The measurements in the laminar region along the $\beta = -90°$ symmetry line fall between the two theories, whereas the measurements along the $\beta = 90°$ symmetry line agree best with the PNS predictions. The predictions from the axisymmetric analog method are considered to be inaccurate along the $\beta = 90°$ symmetry line because of numerical difficulties which could not be resolved. This is more strongly suggested by the sharp gradients in the axisymmetric analog solution near $\beta = 90°$ in the circumferential plots (fig. 25). However, the two theories appear to agree qualitatively away from this region.

The measured circumferential distribution of heating rates (fig. 25) appears to be laminar, except possibly in the small-chine region, through $x/r_n = 7.21$. At $x/r_n = 16.88$, transition appears to occur in the large-flat and small-chine regions. By $x/r_n = 34.88$, the heating rates appear to be mostly transitional around the circumference of the model. In the regions of the model where the data appear to be laminar, the data agree best with the PNS predictions. The PNS predictions appear to capture the peak heating in the small-chine region better than the axisymmetric analog predictions. This may be because streamline spreading in the boundary layer is not taken into account in the axisymmetric analog method.

Effect of Boundary-Layer Trips

In table IX, an overview of the effect of diameter of boundary-layer trips on heating rates in the windward aft region ($x/r_n \geq 16.88$) of the model is given. The region of the model between $x/r_n = 16.88$ and 34.88 is of particular importance because it is where gap heating models and TPS panels will be located for testing (ref. 30). There is some uncertainty in determining where the boundary layer is fully turbulent for this model in regions other than along the windward symmetry line because the boundary-layer code used tends to underpredict the turbulent-boundary-layer heating levels. For table IX, the boundary layer is considered to be turbulent if the axial distribution of heating rates appears to be either leveling off near the turbulent-boundary-layer semiempirical isentropic-expansion predictions at $x/r_n = 16.88$ or climbing above the isentropic-expansion predictions towards the sharp cone predictions. When no trips are used, the boundary layer is laminar over much of the model for $\alpha = 0.4°$ and $N_{\mathrm{Re}} = 0.4 \times 10^6$ ft^{-1}. If free-stream Reynolds number or angle of attack is increased, the boundary layer becomes transitional, and for $\alpha = 15.0°$ and $N_{\mathrm{Re}} = 1.5 \times 10^6$ ft^{-1}, the boundary layer is fully turbulent over the aft region of the model. Although trips are not needed to produce turbulent flow at this condition, comparisons between tripped and untripped data show no adverse effects of the trips.

Selected axial and circumferential distributions of measured heating rates showing the effect of boundary-layer-trip diameter at $N_{\mathrm{Re}} = 0.4 \times 10^6$ ft^{-1} are presented in figures 26 and 27, respectively. Laminar flow heating-rate predictions (ref. 20) are presented to help evaluate the data. Turbulent-boundary-layer predictions from the semiempirical method with the assumption of isentropic expansion are shown with the axial distributions (fig. 26). The level of the semiempirical method predictions is indicated by ticks at $\beta = 90°$ and $-90°$ in the circumferential plots (fig. 27). The circumferential distribution of heating rates at $x/r_n = 7.21$ indicates that when no trips are used, the boundary layer is mostly laminar except in the small-chine region, where transition appears to occur first. However, as shown in a previous section, the axisymmetric analog predictions for $\alpha = 0.4°$ do not capture the peak heating in this region as well as the PNS predictions do. Therefore, the boundary layer may still be laminar here.

The data obtained with the 0.094-in-diameter trips installed show no trip effect until $x/r_n = 16.88$, but the boundary layer never becomes fully turbulent, as indicated by the axial and circumferential distributions of heating rate. As expected, the largest trips (0.190 in. in diameter) are more effective in promoting turbulence over a greater area of the model for this case. Comparing the axial distribution with theory indicates that the boundary layer is fully turbulent by $x/r_n = 21$.

Effect of Reynolds Number on Heating Rates

In figure 28, axial distributions of heating rate are shown at $\alpha = 0°$ for various free-stream Reynolds numbers. Boundary-layer trips were not used during these runs. Also shown with the data are laminar predictions (ref. 20) and turbulent-boundary-layer predictions for the semiempirical isentropic-expansion method. The axial distributions show a forward movement of transition with increasing Reynolds number, as anticipated. The data obtained at $N_{Re} = 1.5 \times 10^6$ ft^{-1} indicate that the boundary layer is turbulent over much of the model. However, the circumferential distributions (fig. 29) indicate that the flow is transitional over much of the model away from the $\beta = -90°$ symmetry line. The level of heating predicted with the semiempirical method is indicated by ticks at $\beta = 90°$ and $-90°$ in the circumferential plots. The circumferential distributions also show that transition does not occur uniformly around the circumference of the model but occurs first in the small-chine and small-flat regions. This behavior is expected because the local Reynolds number varies around the circumference because of the variation in surface angle.

Effect of Angle of Attack

Pressure data. Figure 30 shows the effect of angle of attack on surface pressure at $x/r_n = 21.04$ and $\beta = -90°$. This location was chosen because the axial distributions show less of an effect of free-stream pitot pressure variations at the higher angles of attack. As expected, the pressures generally increase with angle of attack, except near $\alpha = -10°$ and $-15°$. A comparison with the pressure measured in the base region of the model indicates that the base pressure may be feeding forward into the low-pressure, leeward-side region of the model and affecting measurements at these angles of attack. The data show good agreement with both the inviscid predictions and the tangent cone theory for $\alpha \geq 0°$.

Turbulent-boundary-layer heating data. Figure 31 presents the effect of angle of attack on heating rates measured at $x/r_n = 21.38$ and $\beta = -90°$. The data from the present test show good agreement with the semiempirical isentropic-expansion predictions for $\alpha = 0°$ and 5°. For $\alpha = 10°$ to 20°, the data generally agree with the sharp cone theory. This shows the effect of entropy-layer swallowing with increasing angle of attack.

Correlation of Flow Variables

Logarithmic correlations of Reynolds and Stanton number calculated at Eckert's reference temperature are shown in figure 32. Correlations are shown for various total temperatures, free-stream Reynolds numbers, and angles of attack. The edge properties for the data were calculated with the assumption of isentropic flow along the windward symmetry line for $\beta = -90°$ from the stagnation point pressure to the local static pressure. The wetted distance along the windward symmetry line originating from the geometric stagnation point was used as the length scale in the Reynolds number calculations. Laminar and turbulent flow predictions from a semiempirical method are shown to bracket the data.

A correlation for measurements obtained at two ratios of total temperature to wall temperature is shown in figure 32(a). The data were obtained at $\alpha = 0°$ for a tripped boundary layer. The Stanton and Reynolds numbers calculated from the data adequately account for variations in total temperature. There is also a slight variation in free-stream Mach number and Reynolds number (as shown in table V), which are also adequately accounted for by this correlation technique. The line faired through the data is below the turbulent cone theory, but it appears to have the same slope.

Free-stream Reynolds number is correlated in figure 32(b). Again, the faired line through the data is below turbulent cone theory, but it appears to have the same slope (for other than the transition effect). The measurements were obtained for a tripped boundary layer at $\alpha = 0°$.

Reynolds and Stanton numbers calculated from measurements obtained at various angles of attack (fig. 32(c)) do not appear to correlate well. For the data obtained at $\alpha = 0°$, 4.8°, and 9.7°, this lack of correlation may be due to entropy-layer swallowing, as discussed previously. However, at $\alpha = 15.0°$ the variation in free-stream pitot pressure probably also has an adverse effect on the correlation.

Conclusions

A model to be used in flow studies and thermal protection system (TPS) evaluations in three-dimensional boundary layers with pressure

gradients has been tested in the Langley 8-Foot High-Temperature Tunnel. The purposes of the present study were: (1) to define the surface pressures and heating rates at high angles of attack (in support of curved metallic TPS studies and (2) to determine the range of conditions (particularly angle of attack) for which the model would be suitable as a test bed for aerothermal loads studies. Predictions obtained through the use of established methods were used to determine the appropriate levels and trends for evaluating the data. The study was conducted at a nominal free-stream Mach number of 6.8. Angle of attack α ranged from $-20.9°$ to $20.4°$, free-stream dynamic pressure ranged from 2.3 to 10.9 psia, and free-stream Reynolds number ranged from 0.4×10^6 to 1.7×10^6 ft^{-1}. The study was conducted at nominal total temperatures of 2400°R and 3300°R. Most of the measurements consisted of surface pressures and cold-wall ($\approx$ 530°R) heating rates. In addition, Mach number profiles within the shock layer and oil flow photographs were obtained at selected test conditions to help characterize the flow field.

The results show that for this configuration, aerothermal tests should be limited to angles of attack between 10° and −10°. This can be concluded from qualitative comparisons between predictions and the pressure and heating-rate data. This narrow range of angles of attack is a result of the long length of the model (107.63 in.). Above $\alpha \geq |10°|$ the effects of free-stream flow nonuniformity appear in the data. However, for TPS testing this is not a concern and tests can be performed up to $\alpha = |20°|$. At $\alpha = 25°$, the tunnel will unstart.

The experimental heating rates indicate that natural laminar and turbulent boundary layers are available over limited ranges of conditions; however, the turbulent range is extendable through the use of trips. Comparisons between tripped- and untripped-boundary-layer pressure and heating-rate distributions show no adverse effect of the trips on the overall levels and trends of the turbulent data. A laminar boundary layer is available over much of the model at $\alpha = 0.4°$ and a free-stream Reynolds number of 0.4×10^6 ft^{-1}. Logarithmic correlations of Stanton and Reynolds numbers calculated from the measured pressures and heating rates adequately account for effects of both free-stream Reynolds number and ratio of wall temperature to total temperature on heating rates.

NASA Langley Research Center
Hampton, VA 23665-5225
December 30, 1986

References

1. Deveikis, William D.: *Effects of Flow Separation and Cove Leakage on Pressure and Heat-Transfer Distributions Along a Wing-Cove-Elevon Configuration at Mach 6.9.* NASA TP-2127, 1983.
2. Avery, Don E.: *Experimental Aerodynamic Heating to Simulated Space Shuttle Tiles in Laminar and Turbulent Boundary Layers With Variable Flow Angles at a Nominal Mach Number of 7.* NASA TP-2307, 1985.
3. Hunt, L. Roane; Shideler, John L.; and Weinstein, Irving: *Performance of LI-1542 Reusable Surface Insulation System in a Hypersonic Stream.* NASA TN D-8150, 1976.
4. Avery, Don E.; Shideler, John L.; and Stuckey, Robert N.: *Thermal and Aerothermal Performance of a Titanium Multiwall Thermal Protection System.* NASA TP-1961, 1981.
5. Weinstein, Irving; Avery, Don E.; and Hunt, L. Roane: *Aerodynamic Heating on the Corrugated Surface of a 10.2° Half-Angle Blunted Cone at Mach 6.7.* NASA TP-1928, 1981.
6. Nowak, Robert J.; Albertson, Cindy W.; and Hunt, L. Roane: *Aerothermal Tests of a 12.5° Cone at Mach 6.7 for Various Reynolds Numbers, Angles of Attack, and Nose Shapes.* NASA TP-2345, 1985.
7. Gardner, James E.; and Dixon, S. C.: *Loads and Aeroelasticity Division Research and Technology Accomplishments for FY 1984 and Plans for FY 1985.* NASA TM-86356, 1985.
8. Anderson, E. C.; and Lewis, C. H.: *Laminar or Turbulent Boundary-Layer Flows of Perfect Gases or Reacting Gas Mixtures in Chemical Equilibrium.* NASA CR-1893, 1971.
9. Miner, E. W.; Anderson, E. C.; and Lewis, Clark H.: *A Computer Program for Two-Dimensional and Axisymmetric Nonreacting Perfect Gas and Equilibrium Chemically Reacting Laminar, Transitional and-or Turbulent Boundary Layer Flows.* VPI-E-71-8 (Contract NAS1-9337), Dep. Aerosp. Eng., Virginia Polytechnic Inst., Jan. 1975. (Available as NASA CR-132601.)
10. Sterrett, James R.; Morrisette, E. Leon; Whitehead, Allen H., Jr.; and Hicks, Raymond M.: *Transition Fixing for Hypersonic Flow.* NASA TN D-4129, 1967.
11. Gardon, Robert: An Instrument for the Direct Measurement of Intense Thermal Radiation. *Rev. Sci. Instr.*, vol. 24, no. 5, May 1953, pp. 366–370.
12. Deveikis, William D.; and Hunt, L. Roane: *Loading and Heating of a Large Flat Plate at Mach 7 in the Langley 8-Foot High-Temperature Structures Tunnel.* NASA TN D-7275, 1973.
13. Leyhe, E. W.; and Howell, R. R.: *Calculation Procedure for Thermodynamic, Transport, and Flow Properties of the Combustion Products of a Hydrocarbon Fuel Mixture Burned in Air With Results for Ethylene-Air and Methane-Air Mixtures.* NASA TN D-914, 1962.
14. Anderson, John D., Jr.: *Modern Compressible Flow—With Historical Perspective.* McGraw-Hill, Inc., c.1982.

15. Marlowe, M. B.; Moore, R. A.; and Whetstone, W. D.: *SPAR Thermal Analysis Processors Reference Manual, System Level 16.* NASA CR-159162, 1979.
16. Fay, J. A.; and Riddell, F. R.: Theory of Stagnation Point Heat Transfer in Dissociated Air. *J. Aeronaut. Sci.*, vol. 25, no. 2, Feb. 1958, pp. 73–85, 121.
17. Moretti, Gino; and Bleich, Gary: Three-Dimensional Flow Around Blunt Bodies. *AIAA J.*, vol. 5, no. 9, Sept. 1967, pp. 1557–1562.
18. Marconi, Frank; Salas, Manuel; and Yaeger, Larry: *Development of a Computer Code for Calculating the Steady Super/Hypersonic Inviscid Flow Around Real Configurations. Volume I—Computational Technique.* NASA CR-2675, 1976.
19. Marconi, Frank; and Yaeger, Larry: *Development of a Computer Code for Calculating the Steady Super/Hypersonic Inviscid Flow Around Real Configurations. Volume II—Code Description.* NASA CR-2676, 1976.
20. Hamilton, H. Harris, II: *Calculation of Laminar Heating Rates on Three-Dimensional Configurations Using the Axisymmetric Analogue.* NASA TP-1698, 1980.
21. Kays, W. M.: *Convective Heat and Mass Transfer.* McGraw-Hill Book Co., Inc., c.1966.
22. Johnson, H. A.; and Rubesin, M. W.: Aerodynamic Heating and Convective Heat Transfer—Summary of Literature Survey. *Trans. ASME*, vol. 71, no. 5, July 1949, pp. 447–456.
23. Gazley, C., Jr.: *Theoretical Evaluation of the Turbulent Skin-Friction and Heat Transfer on a Cone in Supersonic Flight.* Rep. No. R49A0524, General Electric Co., Nov. 1949.
24. Martin, F. W., Jr.; and Albertson, C. W.: *Aerothermal Environment of a Blunted Three-Dimensional Nonaxisymmetric Body at Mach 6.8.* AIAA-84-1698, June 1984.
25. Li, C. P.: Numerical Simulation of Reentry Flow Around the Shuttle Orbiter Including Real Gas Effects. *Computers in Flow Predictions and Fluid Dynamics Experiments,* K. N. Ghia, T. J. Mueller, and B. R. Patel, eds., American Soc. Mech. Eng., 1981, pp. 141–149.
26. Li, C. P.: A Numerical Study of Laminar Flow Separation on Blunt Flared Cones at Angle of Attack. AIAA Paper No. 74-585, June 1974.
27. Li, C. P.: Implicit Solution for the Shock-Layer Flow Around General Bodies. *AIAA J.*, vol. 20, no. 2, Feb. 1982, pp. 175–183.
28. Cooke, J. C.: *An Axially Symmetric Analogue for General Three-Dimensional Boundary Layers.* R. & M. No. 3200, British A.R.C., 1961.
29. Ames Research Staff: *Equations, Tables, and Charts for Compressible Flow.* NACA Rep. 1135, 1953. (Supersedes NACA TN 1428.)
30. Albertson, Cindy W.: Aerothermal Environment of an Apparatus for Testing Curved TPS Concepts. *Advances in TPS and Structures for Space Transportation Systems,* H. Neale Kelly and James E. Gardner, compilers, NASA CP-2315, 1984, pp. 345–360.

Table I. Pressure Orifice Locations on Model

Orifice	x/r_n	β, deg	Orifice	x/r_n	β, deg
1	0.034	90	36	25.545	−88
2	0.034	−90	37	↓	−62
3	2.877	−87	38	↓	−52
4	2.877	0	39	↓	−43
5	6.877	−87	40	↓	−39
6	↓	−62	41	↓	−34
7	↓	−50	42	↓	−28
8	↓	−38	43	↓	−23
9	↓	−25	44	↓	−12
10	↓	−15	45	↓	0
11	↓	0	46	↓	15
12	↓	18	47	↓	31
13	↓	36	48	↓	48
14	↓	55	49	↓	66
15	↓	87	50	↓	88
16	↓	180	51	↓	180
17	10.877	−88	52	30.045	−89
18	10.877	0	53	30.045	0
19	16.545	−88	54	34.545	−89
20	↓	−66	55	↓	−60
21	↓	−56	56	↓	−46
22	↓	−48	57	↓	−41
23	↓	−42	58	↓	−38
24	↓	−35	59	↓	−34
25	↓	−28	60	↓	−29
26	↓	−21	61	↓	−25
27	↓	0	62	↓	−13
28	↓	16	63	↓	0
29	↓	32	64	↓	15
30	↓	50	65	↓	31
31	↓	69	66	↓	47
32	↓	88	67	↓	64
33	↓	180	68	↓	89
34	21.045	−88	69	↓	180
35	21.045	0			

Table II. Heat Flux Sensor Locations on Model

Heat flux sensor	x/r_n	β, deg	Heat flux sensor	x/r_n	β, deg
1	0		35	25.877	−88
2	3.209	−87	36	↓	−62
3	3.209	0	37	↓	−52
4	7.209	−87	38	↓	−43
5	↓	−62	39	↓	−39
6	↓	−50	40	↓	−34
7	↓	−38	41	↓	−28
8	↓	−25	42	↓	−23
9	↓	−15	43	↓	−12
10	↓	0	44	↓	0
11	↓	18	45	↓	15
12	↓	36	46	↓	31
13	↓	55	47	↓	48
14	↓	87	48	↓	66
15	↓	180	49	↓	88
16	11.209	−88	50	↓	180
17	11.209	0	51	30.377	−89
18	16.877	−88	52	30.377	0
19	↓	−66	53	34.877	−89
20	↓	−56	54	↓	−60
21	↓	−48	55	↓	−46
22	↓	−42	56	↓	−41
23	↓	−35	57	↓	−38
24	↓	−28	58	↓	−34
25	↓	−21	59	↓	−29
26	↓	0	60	↓	−25
27	↓	16	61	↓	−13
28	↓	32	62	↓	0
29	↓	50	63	↓	15
30	↓	69	64	↓	31
31	↓	88	65	↓	47
32	↓	180	66	↓	64
33	21.377	−88	67	↓	89
34	21.377	0	68	↓	180

Table III. Thermocouple Locations on Model

Thermocouple	x/r_n	β, deg
1	3.209	87
2	7.209	−74
3	11.209	88
4	16.877	−76
5	16.877	−11
6	16.877	79
7	21.377	88
8	30.377	89
9	34.877	−77
10	↓	−69
11		80
12		71

Table IV. Summary of Test Conditions

			Runs performed at angle of attack, deg, of—								
d, in.	N_{Re}, ft^{-1}	T_t, °R	0	4.6	9.6	15.0	20.4	−4.5	−9.5	−14.9	−20.9
0	0.4×10^6	3300	99-17,21A	99-21B	99-21C	99-21D					
	.9	3300	99-4								
	1.5	3300	99-5			99-6					
0.094	0.4×10^6	3300	99-9								
	.9	3300	99-10			99-15					
	1.5	3300	99-8,27	99-16	99-13	99-7	99-18	99-28	99-29	99-31	99-30
	1.7	2400	99-19D	99-19C	99-19B	99-19A		99-26C	99-26B	99-26A	
0.190	0.4×10^6	3300	99-11,12D	99-12C	99-12B	99-12A		99-23C	99-23B	99-23A	
	.9	2400						99-24C	99-24B	99-24A	

Table V. Detailed Flow Conditions

Run	α, deg	[a]N_{Re}, ft^{-1}	T_t, °R	[a]q_∞, psia	[a]M_∞	d, in.	$\dot{q}_s$, Btu/ft^2-sec	p_s, psia	Nominal data selection time, sec
99-30	−20.9	1.44×10^6	3400	8.33	6.6	0.094	74.6	15.5	1.5
99-26A	−14.9	1.66×10^6	2380	9.16	5.6	0.094	43.6	17.1	1.5
[b]99-31	−14.8	1.57	3200	8.97	6.4	.094	70.5	16.7	1.5
99-24A	−14.9	.95	3200	5.42	6.5	.190	54.7	10.1	1.5
99-23A	−14.9	.40	3270	2.33	6.8	.190	36.9	4.34	1.5
99-26B	−9.4	1.66×10^6	2360	9.05	5.6	0.094	42.8	16.9	9.2
[b]99-29	−9.7	1.49	3310	9.99	6.5	.094	78.2	18.6	1.5
99-24B	−9.4	.95	3200	5.85	6.5	.190	56.8	10.9	9.2
99-23B	−9.5	.39	3360	2.52	6.9	.190	40.5	4.68	9.2
99-26C	−4.5	1.67×10^6	2430	8.73	5.7	0.094	43.7	16.3	16.8
[b]99-28	−4.8	1.41	3320	10.9	6.5	.094	82.4	20.4	1.5
99-24C	−4.4	.87	3400	6.55	6.6	.190	65.9	12.2	16.8
99-23C	−4.4	.40	3300	2.69	6.9	.190	41.1	5.01	16.8
99-19D	−0.1	1.67×10^6	2400	8.56	5.6	0.094	42.7	16.0	19.7
[b]99-27	−.1	1.41	3450	10.8	6.6	.094	87.0	20.2	1.5
[b]99-8	0	1.49	3300	10.6	6.5	.094	80.2	19.8	1.5
99-5	0	1.58	3200	10.6	6.4	0	76.6	19.8	1.5
99-10	0	0.91×10^6	3300	6.45	6.6	0.094	62.6	12.0	1.5
99-4	0	.93	3250	6.44	6.5	0	61.2	12.0	1.5
99-12D	.1	.40	3400	2.57	6.9	.190	43.3	5.23	19.7
99-11	0	.39	3450	2.57	7.0	.190	43.7	5.10	1.5
99-9	0	.41	3300	2.50	6.8	.094	40.3	4.94	1.5
99-21A	.4	.41	3350	2.57	6.9	0	41.6	5.14	1.5
[b]99-17	.1	.38	3420	2.43	7.0	0	42.8	4.97	1.5
99-19C	4.6	1.67×10^6	2410	7.71	5.6	0.094	43.2	16.3	12.5
[b]99-16	4.8	1.41	3450	9.93	6.6	.094	86.9	20.2	1.5
99-12C	4.4	.39	3475	2.57	7.0	.190	45.1	5.34	12.5
99-21B	4.8	.41	3330	2.57	6.8	0	41.6	5.14	7.3
99-19B	9.5	1.67×10^6	2420	7.78	5.6	0.094	44.0	16.7	7.3
[b]99-13	9.7	1.56	3200	9.86	6.4	.094	73.8	18.4	1.5
99-12B	9.5	.40	3380	2.57	6.9	.190	41.5	4.85	7.3
99-21C	9.8	.41	3310	2.57	6.8	0	40.5	4.93	12.5
99-19A	14.8	1.67×10^6	2490	7.99	5.7	0.094	46.4	17.2	1.5
[b]99-7	15.0	1.49	3300	9.93	6.5	.094	73.0	16.3	1.5
99-6	15.5	1.55	3250	10.1	6.5	0	72.3	16.7	1.5
99-15	14.9	.92	3280	6.04	6.5	.094	57.6	10.4	1.5
99-12A	14.7	.40	3400	2.57	6.9	.190	40.6	4.55	1.5
99-21D	14.9	.40	3370	2.57	6.9	0	40.1	4.55	19.7
99-18	20.4	1.51	3290	9.93	6.5	0.094	70.2	15.2	1.5

[a]Based on tunnel surveys from test 44, averaged over a 20-in. stream 20 in. from nozzle exit.
[b]Shock-layer rake used.

Table VI. Pitot Pressures and Computed Mach Numbers From Shock-Layer Rake

Run	α, deg	p_{t2}, psia, at probe number[a]—							Mach number at probe number[a]—						
		1	2	3	4	5	6	7	1	2	3	4	5	6	7
99-31	−14.8	37.40	48.40	59.40	62.60	63.80	65.40	65.60	3.21	3.66	4.06	4.18	4.22	4.27	4.28
99-29	−9.7	24.00	32.80	45.80	56.10	58.00	57.60	56.50	3.22	3.78	4.48	4.97	5.05	5.04	4.99
99-28	−4.8	8.08	10.70	16.50	28.70	38.30	41.40	41.90	2.43	2.87	3.53	4.69	5.43	5.64	5.68
99-27	−.1	2.86	3.58	4.43	5.90	7.85	10.70	14.30	1.88	2.13	2.40	2.78	3.23	3.79	4.40
99-8	0	2.90	3.57	4.33	5.77	7.47	10.20	13.40	1.86	2.09	2.31	2.69	3.08	3.63	4.17
99-17	.1	0.60	0.73	0.87	1.72	1.97	2.64	3.41	1.59	1.79	1.96	2.84	3.04	3.54	4.04
99-16	4.8	7.42	8.53	11.80	19.40	32.00	39.40	42.20	2.22	2.39	2.85	3.69	4.75	5.29	5.48
99-13	9.7	20.20	26.70	37.80	53.80	60.40	60.50	59.20	2.83	3.28	3.92	4.68	4.97	4.97	4.92
99-7	15.0	34.40	45.40	56.40	61.90	62.60	63.20	64.90	2.98	3.45	3.85	4.04	4.06	4.08	4.14

[a]See figure 8 for probe locations.

Table VII. Pressure Data

(a) Surface pressures

Run	Surface pressure, psia, for orifice[a]—															
	3	4	5	6	7	8	9	10	11	12	13	14	15	16	17	18
$\alpha = -20.9°$																
99-30	.289	.726	.234	.064	.101	.090	.207	.578	.581	1.400	2.730	3.820	4.360	.678	.139	.819
$\alpha \approx -14.9°$																
99-26A	.340	.729	.320	.160	.180	.180	.290	.600	.637	1.040	1.760	2.270	2.560	.645	.370	.710
99-31	.350	.800	.390	.320	.340	.320	.320	.615	.638	1.140	2.070	2.780	3.070	.652	.420	.745
99-24A	.237	.473	.193	.094	.107	.100	.170	.371	.387	.681	1.210	1.580	1.870	.423	.156	.427
99-23A	.101	.202	.087	.064	.061	.052	.069	.156	.164	.278	.484	.642	.749	.188	.071	.175
$\alpha \approx -9.5°$																
99-26B	.430	.733	.340	.300	.250	.300	.390	.567	.646	.790	1.080	1.260	1.370	.669	.420	.721
99-29	.510	.906	.370	.310	.240	.290	.419	.619	.707	.881	1.260	1.500	1.660	.730	.430	.757
99-24B	.303	.526	.225	.180	.158	.179	.244	.363	.417	.522	.735	.866	.981	.443	.193	1.040
99-23B	.127	.214	.096	.076	.074	.078	.093	.152	.169	.212	.298	.368	.394	.182	.083	.174
$\alpha \approx -4.5°$																
99-26C	.490	.716	.354	.330	.332	.393	.458	.537	.574	.605	.683	.708	.738	.594	.369	.644
99-28	.663	.963	.452	.424	.404	.459	.540	.632	.679	.716	.799	.822	.879	.697	.383	.652
99-24C	.394	.574	.276	.252	.250	.283	.324	.378	.404	.436	.478	.497	.532	.418	.235	.391
99-23C	.160	.231	.112	.104	.106	.119	.123	.157	.163	.177	.195	.222	.218	.175	.098	.159
$\alpha \approx 0°$																
99-19D	.624	.709	.472	.455	.491	.529	.533	.540	.527	.511	.469	.461	.460	.552	.479	.584
99-27	.841	.962	.578	.564	.578	.626	.634	.644	.641	.610	.581	.548	.579	.655	.497	.602
99-8	.841	.936	.586	.555	.592	.606	.631	.631	.623	.589	.544	.541	.542	.654	.524	.591
99-5	.829	.939	.581	.562	.592	.601	.629	.635	.624	.598	.563	.555	.555	.655	.520	.589
99-10	.496	.571	.355	.344	.393	.364	.373	.391	.385	.371	.341	.337	.338	.394	.319	.364
99-4	.487	.572	.345	.337	.362	.344	.394	.397	.397	.382	.346	.338	.336	.397	.316	.374
99-12D	.212	.244	.159	(b)	.167	.153	.168	.174	.172	.167	.145	.143	.144	.180	.151	.161
99-11	.214	.246	.158	(b)	(b)	.169	.167	.175	.174	.169	.149	.147	.147	.180	.148	.162
99-9	.205	.236	.151	(b)	(b)	(b)	.155	.164	.164	.162	.148	.145	.146	.176	(b)	.157
99-21A	.208	.245	.157	(b)	.167	.174	.176	.175	.178	.170	.165	.162	.161	.185	.151	.160
99-17	.198	.231	.148	(b)	.156	.154	.161	.164	.167	.162	.141	.139	.139	.172	.140	.151
$\alpha \approx 4.6°$																
99-19C	.864	.731	.766	.762	.804	.778	.662	.589	.540	.431	.358	.344	.355	.545	.819	.572
99-16	1.180	.961	.918	.876	.925	.904	.749	.679	.622	.499	.427	.421	.450	.627	.858	.578
99-12C	.320	.249	.268	.311	.280	.238	.214	.189	.176	.135	.103	.104	.114	.176	.263	.162
99-21B	.286	.243	.235	.227	.250	.206	.206	.183	.176	.145	.110	.109	.115	.177	.236	.159
$\alpha \approx 9.6°$																
99-19B	1.350	.760	1.490	1.470	1.500	1.300	.911	.653	.612	.359	.266	.267	.311	.591	1.500	.632
99-13	1.630	.898	1.760	1.720	1.730	1.470	1.010	.708	.668	.373	.272	.290	.380	.634	1.800	.666
99-12B	.436	.238	.462	.473	.471	.372	.276	.196	.188	.105	.059	.074	.101	.181	.484	.182
99-21C	.420	.241	.443	.447	.458	3.540	.276	.199	.193	.119	.077	.087	.102	.187	.469	.180
$\alpha \approx 15°$																
99-19A	2.090	.761	2.760	2.730	2.690	2.200	1.360	.711	.740	.277	.131	.162	.315	.707	2.440	.767
99-7	2.110	.789	3.231	(b)	2.880	2.260	1.410	.701	.740	.283	.149	.179	.327	.706	2.980	.747
99-6	2.260	.786	3.390	3.030	3.310	2.610	1.540	.735	.727	.271	.136	.166	.336	.717	3.150	.761
99-15	1.410	.506	2.040	2.000	1.980	1.520	.936	.463	.472	.184	.088	.113	.206	.452	1.860	.477
99-12A	.598	.226	.795	.784	.783	.582	.373	.202	.205	.092	.049	.061	.096	.202	.786	.205
99-21D	.584	.225	.782	.793	.788	.580	.387	.205	.215	.095	.042	.057	.092	.203	.775	.206
$\alpha = 20.4°$																
99-18	2.950	.704	4.440	(b)	4.090	3.140	1.740	.767	.657	.226	.113	.104	.271	.612	4.390	.802

[a]See figure 9(a) for orifice locations.
[b]Instrumentation not functional.

Table VII. Continued

(a) Continued

Run	Surface pressure, psia, for orifice[a]—																
	19	20	21	22	23	24	25	26	27	28	29	30	31	32	33	34	35
$\alpha = -20.9°$																	
99-30	.085	.058	.085	.092	.096	.090	.302	.742	.780	(b)	2.750	3.460	3.720	3.750	.696	.101	.814
$\alpha \approx -14.9°$																	
99-26A	.340	.350	.430	.360	.380	.370	.390	.675	.732	1.190	1.730	(b)	2.040	2.050	.637	.530	.795
99-31	.470	.420	.470	.460	.480	.470	.390	.732	.761	1.310	2.040	2.490	2.520	2.500	.677	.547	.841
99-24A	.071	.047	.115	.083	.087	.064	.188	.448	.461	.788	1.200	(b)	1.480	1.490	.388	.116	.508
99-23A	.043	.011	.058	.051	.056	.048	.074	.186	.194	.331	.492	.590	.619	.614	.122	.062	.216
$\alpha \approx -9.5°$																	
99-26B	.460	.470	.490	.460	.460	.450	.430	.606	.778	1.000	1.260	(b)	1.350	1.320	.670	.580	.806
99-29	.520	.500	.520	.510	.520	.510	.460	.615	.798	1.100	1.500	1.720	1.710	1.690	.674	.600	.894
99-24B	.092	.100	.176	.105	.110	.094	.200	.370	.465	.650	.868	(b)	.958	.941	.377	.189	.533
99-23B	.043	.009	.066	.048	.046	.038	.075	.152	.189	.263	.352	.388	.395	.384	.105	.074	.216
$\alpha \approx -4.6°$																	
99-26C	.377	.379	.403	.301	.292	.387	.532	.638	.713	.788	.835	(b)	.786	.780	.600	.395	.730
99-28	.345	.336	.353	.290	.299	.348	.503	.621	.720	.822	.911	(b)	.894	.872	.618	.367	.796
99-24C	.214	.201	.217	.187	.177	.219	.303	.380	.425	.488	.528	.522	.511	.494	.232	.232	.473
99-23C	.085	.058	.085	.081	.076	.092	.120	.158	.173	.197	.212	.202	.208	.195	.091	.098	.193
$\alpha \approx 0.0°$																	
99-19D	.519	.519	.506	.507	.575	.650	.697	.686	.660	.631	.586	.523	.516	.527	.587	.503	.693
99-27	.526	.499	.502	.537	.598	.667	.725	.707	.664	.639	.555	.539	.595	.492	.563	.555	.742
99-8	.522	.530	.518	.553	.606	.674	.702	.681	.641	.612	.559	.499	.495	.503	.570	.543	.731
99-5	.524	.533	.539	.550	.612	.683	.715	.698	.649	.619	.566	.507	.495	.502	.582	.537	.735
99-10	.312	.317	.314	.331	.361	.408	.436	.429	.398	.376	.341	.295	.298	.305	.302	.313	.454
99-4	.329	.326	.326	.336	.368	.427	.476	.469	.433	.408	.358	.309	.314	.319	.313	.314	.475
99-12D	.150	.149	.144	.159	.164	.180	.200	.200	.178	.168	.145	.113	.129	.132	.084	.129	.195
99-11	.140	.141	.140	.148	.160	.183	.190	.191	.173	.163	.150	.118	.134	.142	.082	.130	.195
99-9	.137	(b)	(b)	.143	.159	.177	.190	.192	.176	.165	.152	.122	.137	.144	.089	(b)	.190
99-21A	.156	.151	.151	.157	.170	.187	.204	.196	.181	.173	.149	.135	.134	.138	.089	.162	.193
99-17	.137	.135	.133	.145	.153	.168	.189	.187	.169	.160	.144	.111	.128	.135	.075	.120	.182
$\alpha \approx 4.6°$																	
99-19C	.801	.835	.850	.905	.998	1.000	.860	.644	.647	.486	.383	.352	.407	.430	.547	.832	.681
99-16	.863	.906	.918	.989	1.070	1.050	.848	.707	.597	.425	.332	.307	.348	.369	.494	.914	.694
99-12C	.275	.277	.279	.306	.322	.304	.263	.221	.179	.115	.068	.057	.080	.100	.082	.265	.195
99-21B	.255	.252	.256	.279	.294	.296	.267	.224	.181	.135	.102	.077	.106	.113	.083	.239	.192
$\alpha \approx 9.6°$																	
99-19B	1.380	1.450	1.460	1.550	1.600	1.440	1.070	.765	.735	.347	.160	.173	.274	.342	.609	1.330	.726
99-13	1.660	1.760	1.780	1.900	1.920	1.710	1.210	.786	.778	.317	.141	.146	.244	.313	.618	1.670	.828
99-12B	.461	.476	.480	.514	.513	.452	.335	.226	.211	.096	.046	.027	.042	.075	.109	.437	.224
99-21C	.460	.463	.470	.500	.504	.455	.347	.232	.208	.100	.059	.041	.059	.098	.106	.426	.215
$\alpha \approx 15.0°$																	
99-19A	2.080	2.210	2.230	2.350	2.310	1.910	1.280	.782	.780	.331	.124	.134	.137	.235	.644	2.080	.762
99-7	2.480	2.570	2.620	2.830	2.710	2.190	1.410	.819	.808	.329	.142	.146	.181	.200	.675	2.490	.829
99-6	2.630	2.840	2.860	2.990	2.850	2.290	1.450	.826	.808	.340	.114	.107	.109	.177	.662	2.680	.816
99-15	1.540	1.650	1.660	1.740	1.670	1.370	.897	.527	.511	.214	.090	.069	.091	.129	.371	1.530	.517
99-12A	.676	.707	.709	.741	.710	.587	.396	.244	.231	.100	.060	.034	.058	.074	.126	.648	.230
99-21D	.675	.692	.697	.731	.699	.582	.399	.242	.225	.103	.042	.025	.046	.064	.122	.643	.223
$\alpha = 20.4°$																	
99-18	3.610	3.910	3.950	4.100	3.810	2.860	1.670	.850	.842	.312	.098	.089	.106	.110	.710	3.630	.853

[a]See figure 9(a) for orifice locations.
[b]Instrumentation not functional.

Table VII. Continued

(a) Continued

Run	Surface pressure, psia, for orifice[a]—																
	36	37	38	39	40	41	42	43	44	45	46	47	48	49	50	51	52
$\alpha = -20.9°$																	
99-30	.092	.060	.059	.058	.053	.108	.307	.718	.798	.778	(b)	2.790	4.110	3.990	3.640	.778	.083
$\alpha \approx -14.9°$																	
99-26A	.580	.550	.540	.560	.580	.630	.600	.684	.794	.773	1.090	1.750	2.340	2.190	2.070	.734	.630
99-31	.590	.600	.600	.600	.610	.640	.530	.709	.852	.799	1.290	2.110	2.830	2.750	2.630	.768	.650
99-24A	.092	.076	.110	.074	.066	.095	.207	.428	.508	.481	.745	1.240	1.690	1.600	1.510	.490	.082
99-23A	.054	.054	(b)	.048	.044	.059	.089	.178	.213	.208	.318	.521	.697	.667	.629	.215	.050
$\alpha \approx -9.5°$																	
99-26B	.620	.610	.590	.600	.610	.640	.590	.660	.754	.773	.928	1.290	1.480	1.400	1.390	.746	.670
99-29	.620	.620	.610	.610	.620	.650	.560	.696	.835	.862	1.090	1.620	1.860	1.810	1.810	.846	.650
99-24B	.160	.071	.078	.088	.087	.120	.225	.406	.499	.525	.652	.939	1.070	1.040	1.040	.515	.149
99-23B	.056	.041	(b)	.039	.037	.058	.088	.162	.201	.214	.269	.378	.439	.425	.419	.212	.051
$\alpha \approx -4.5°$																	
99-26C	.372	.364	.331	.247	.250	.400	.550	.650	.700	.721	.771	.905	.868	.846	.888	.710	.359
99-28	.356	.343	.286	.209	.200	.365	.540	.681	.761	.801	.882	1.090	1.060	1.020	1.070	.796	.350
99-24C	.218	.214	.183	.143	.137	.246	.336	.418	.457	.484	.524	.626	.595	.584	.616	.470	.213
99-23C	.085	.079	(b)	.062	.055	.110	.133	.165	.184	.199	.215	.255	.242	.239	.250	.196	.080
$\alpha \approx 0.0°$																	
99-19D	.518	.504	.511	.474	.522	.642	.705	.709	.699	.695	.646	.620	.576	.540	.564	.680	.504
99-27	.554	.556	.552	.536	.581	.741	.814	.793	.773	.760	.701	.686	.600	.599	.600	.741	.546
99-8	.583	.569	.587	.553	.605	.735	.800	.784	.765	.752	.677	.633	.577	.550	.558	.743	.582
99-5	.595	.586	.622	.553	.606	.752	.830	.807	.780	.760	.701	.643	.585	.560	.569	.766	.598
99-10	.355	.340	.392	.333	.367	.457	.505	.495	.481	.471	.422	.388	.348	.324	.334	.444	.356
99-4	.361	.362	.423	.322	.358	.468	.525	.515	.502	.494	.452	.405	.359	.356	.346	.457	.371
99-12D	.159	.162	(b)	(b)	.160	.205	.223	.212	.210	.204	.180	.164	.142	.137	.135	.198	.163
99-11	.159	.152	(b)	(b)	.162	.199	.219	.211	.206	.202	.178	.168	.145	.133	.145	.190	.154
99-9	.158	(b)	(b)	(b)	(b)	(b)	(b)	.204	.199	.200	.179	.171	.155	.131	.149	.199	(b)
99-21A	.168	.170	(b)	.172	.187	.219	.232	.220	.214	.208	.181	.165	.152	.149	.139	.203	.169
99-17A	.147	.140	(b)	.134	.150	.189	.209	.199	.196	.192	.170	.160	.137	.125	.133	.182	.149
$\alpha \approx 4.6°$																	
99-19C	.880	.870	.876	.890	.942	.972	.861	.798	.742	.664	.479	.366	.346	.365	.394	.649	.850
99-16	1.020	1.020	1.030	1.070	1.150	1.170	1.000	.872	.814	.703	.456	.320	.293	.319	.353	.676	1.040
99-12C	.298	.319	.378	.328	.328	.335	.289	.246	.236	.204	.120	.065	.065	.064	.083	.189	.309
99-21B	.286	.292	.334	.293	.304	.329	.287	.245	.233	.208	.135	.098	.085	.107	.103	.196	.292
$\alpha \approx 9.6°$																	
99-19B	1.500	1.450	1.440	1.480	1.490	1.370	1.020	.818	.817	.698	.361	.181	.222	.159	.305	.680	1.430
99-13	1.870	1.840	1.820	1.880	1.870	1.670	1.180	.842	.928	.791	.376	.161	.179	.131	.275	.750	1.860
99-12B	.496	.506	.543	.506	.498	.454	.333	.237	.257	.222	.102	.044	.040	.051	.053	.208	.509
99-21D	.489	.496	.538	.496	.490	.459	.334	.235	.254	.224	.104	.054	.050	.064	.070	.210	.496
$\alpha \approx 15.0°$																	
99-19A	2.350	2.250	2.210	2.260	2.200	1.840	1.200	.731	.857	.741	.340	.140	.152	.130	.182	.721	2.250
99-7	2.710	2.680	2.670	2.730	2.690	2.210	1.420	.787	.910	.813	.345	.163	.274	.162	.189	.782	2.820
99-6	3.040	2.940	2.960	2.960	2.780	2.250	1.420	.786	.903	.808	.335	.145	.135	.136	.156	.790	3.000
99-15	1.700	1.670	1.680	1.680	1.620	1.340	.868	.494	.569	.508	.213	.087	.083	.076	.094	.484	1.690
99-12A	.735	.726	.753	.722	.684	.575	.379	.223	.258	.227	.097	.055	.048	.072	.064	.219	.744
99-21D	.734	.721	.753	.709	.669	.569	.376	.222	.252	.230	.099	.048	.043	.056	.045	.220	.732
$\alpha = 20.4°$																	
99-18	(b)	3.920	3.980	3.990	3.680	2.820	1.640	.830	.895	.832	.296	.097	.088	.080	.114	.805	(b)

[a]See figure 9(a) for orifice locations.
[b]Instrumentation not functional.

Table VII. Continued

(a) Concluded

Run	Surface pressure, psia, for orifice[a]—																
	53	54	55	56	57	58	59	60	61	62	63	64	65	66	67	68	69
$\alpha = -20.9°$																	
99-30	.820	.101	.122	.122	.124	.117	.109	.319	.684	.820	.798	1.620	2.750	3.600	3.650	3.680	.838
$\alpha \approx -14.9°$																	
99-26A	.832	.700	.740	.740	.750	.770	.770	.810	.740	.834	.818	1.220	1.820	2.160	2.110	2.200	.830
99-31	.860	.700	.680	.660	.690	.635	.705	.685	.770	.873	.819	1.400	2.150	2.570	2.610	2.730	.845
99-24A	.515	.103	.090	.091	.089	.081	.082	.215	.389	.523	.485	.793	1.250	1.510	1.530	1.600	.533
99-23A	.242	.092	.069	.066	.079	.050	.073	.101	.164	.219	.216	.342	.556	.641	.671	.683	.231
$\alpha \approx -9.5°$																	
99-26B	.839	.710	.740	.740	.760	.780	.790	.810	.730	.804	.827	1.020	1.330	1.420	1.330	1.380	.816
99-29	.916	.700	.750	.770	.780	.880	.790	.770	.790	.900	.880	1.150	1.550	1.720	1.670	1.740	.895
99-24B	.573	.153	.079	.086	.096	.090	.112	.250	.392	.525	.553	.703	.939	1.010	.978	.999	.561
99-23B	.253	.089	.082	.072	.083	.053	.075	.105	.164	.211	.229	.288	.406	.423	.423	.419	.237
$\alpha \approx -4.5°$																	
99-26C	.783	.440	.400	.430	.430	.390	.420	.580	.650	.744	.767	.844	.922	.822	.808	.809	.764
99-28	.858	.357	.334	.273	.210	.239	.363	.566	.688	.804	.863	.980	1.110	1.070	.982	.999	.856
99-24C	.533	.220	.215	.184	.137	.156	.240	.363	.413	.493	.519	.576	.663	.619	.569	.560	.515
99-23C	.239	.092	.087	.070	.080	.046	.100	.157	.177	.200	.219	.240	.291	.258	.249	.227	.214
$\alpha \approx 0.0°$																	
99-19D	.740	.505	.500	.508	.504	.560	.625	.772	.733	.739	.718	.691	.643	.572	.550	.567	.741
99-27	.819	.566	.560	.575	.563	.654	.736	.870	.804	.824	.812	.765	.734	.617	.563	.564	.776
99-8	.789	.587	.589	.618	.596	.661	.715	.866	.793	.786	.759	.711	.658	.566	.553	.561	.786
99-5	.805	.605	.592	.630	.594	.676	.745	.899	.826	.822	.790	.732	.680	.581	.589	.571	.809
99-10	.516	.361	.374	.401	.373	(b)	.444	.559	.506	.517	.492	.460	.424	.352	.364	.342	.475
99-4	.520	.371	.377	.422	.384	.404	.422	.553	.498	.523	.497	.459	.447	.355	.413	.344	.472
99-12D	.240	.166	.180	.213	.180	(b)	.172	.251	.210	.232	.218	.194	.200	.145	.200	.140	.209
99-11	.243	.153	.169	.201	.172	(b)	.189	.253	.225	.226	.220	.195	.188	.158	.149	.147	.209
99-9	.236	(b)	(b)	(b)	(b)	.193	.185	.238	.215	.214	.217	.191	.184	.159	.146	.150	.215
99-21A	.211	.172	.178	.182	.178	.199	.229	.253	.240	.235	.219	.201	.179	.159	.154	.149	.210
99-17	.226	.159	.169	.200	.171	.182	.163	.233	.204	.212	.205	.181	.183	.141	.163	.133	.195
$\alpha \approx 4.6°$																	
99-19C	.735	.862	.838	.878	.906	.985	.958	.992	.841	.809	.699	.525	.392	.332	.357	.379	.703
99-16	.792	1.060	1.030	1.070	1.100	(b)	1.140	1.120	.934	.884	.747	.518	.357	.279	.324	.353	.753
99-12C	.243	.311	.319	.347	.336	(b)	.293	.323	.246	.257	.217	.137	.104	.077	.134	.093	.203
99-21B	.243	.296	.321	.359	.344	.340	.273	.309	.238	.256	.219	.145	.141	.090	.170	.980	.206
$\alpha \approx 9.6°$																	
99-19B	.759	1.450	1.400	1.430	1.480	1.520	1.310	1.100	.865	.877	.718	.401	.204	.190	.194	.276	.733
99-13	.846	1.870	1.750	1.780	1.810	(b)	1.530	1.210	.863	.963	.787	.422	.200	.178	.161	.260	.786
99-12B	.258	.520	.514	.553	.531	(b)	.545	.457	.263	.280	.228	.110	.113	.087	.143	.070	.212
99-21C	.258	.505	.511	.547	.540	.573	.489	.418	.250	.278	.228	.109	.117	.084	.155	.074	.215
$\alpha \approx 15.0°$																	
99-19A	.810	2.310	2.230	2.280	2.280	2.220	1.750	1.280	.738	.940	.780	.362	.159	.140	.135	.179	.764
99-7	.871	2.880	2.670	2.740	2.680	2.530	1.930	1.360	.758	.937	.826	.346	.181	.297	.138	.174	.825
99-6	.876	2.950	2.750	2.750	2.700	2.570	1.960	1.390	.748	.938	.815	.338	.161	.113	.143	.160	.818
99-15	.240	1.710	1.630	1.660	1.630	(b)	1.180	.853	.461	.597	.510	.214	.119	.078	.104	.098	.482
99-12A	.263	.751	.740	.772	.798	(b)	.886	.622	.282	.277	.230	.097	.112	.082	.139	.078	.220
99-21D	.263	.738	.733	(b)	(b)	(b)	(b)	(b)	(b)	(b)	(b)	.098	.118	.082	.153	.081	.254
$\alpha = 20.4°$																	
99-18	.895	4.160	3.860	3.830	3.630	3.320	2.390	1.530	.754	.908	.846	.304	.116	.140	.110	.115	.816

[a]See figure 9(a) for orifice locations.
[b]Instrumentation not functional.

Table VII. Concluded

(b) Model base and surrounding area pressures

Run	α, deg	p_∞/p_s	p_b/p_s	[a]p_m, psia	[a]p_b/p_m
99-4	0	0.0172	0.0102	0.0292	0.3493
99-5	0	.0179	.0092	.0291	.3162
99-6	15.5	.0180	.0150	.0058	2.5860
99-7	15.0	.0178	.0099	.0072	1.3750
99-8	0	.0177	.0088	.0288	.3056
99-9	0	.0158	.0162	.0296	.5473
99-10	0	.0173	.0220	.0296	.7432
99-11	0	.0153	.0160	.0296	.5405
99-12A	14.7	.0155	.0161	.0156	1.0320
99-12B	9.5	.0156	.0180	.0140	1.2860
99-12C	4.4	.0152	.0181	.0155	1.1680
99-12D	.1	.0155	.0200	.0281	.7117
99-13	9.7	.0179	.0062	.0083	.7470
99-15	14.9	.0177	.0077	.0084	.9167
99-16	4.8	.0174	.0078	.0146	.5342
99-17	.1	.0153	.0234	.0282	.8298
99-18	20.4	.0177	.0135	.0057	2.3680
99-19A	14.8	.0209	.0089	.0080	1.1120
99-19B	9.5	.0214	.0079	.0116	.6810
99-19C	4.6	.0216	.0092	.0204	.0232
99-19D	−.1	.0215	.0104	.0307	.0348
99-21A	.4	.0152	.0194	.0289	.0289
99-21B	4.8	.0153	.0175	.0175	.0190
99-21C	9.8	.0154	.0175	.0144	.0144
99-21D	14.9	.0151	.0175	.0157	.0157
99-23A	−14.9	.0159	.0228	.0104	.1410
99-23B	−9.5	.0155	.0228	.0110	.0867
99-23C	−4.4	.0156	.0207	.0095	.0470
99-24A	−14.9	.0171	.0092	.0068	.1330
99-24B	−9.4	.0171	.0083	.0066	.0832
99-24C	−4.4	.0166	.0076	.0116	.0474
99-26A	−14.9	.0209	[b].0491	.0419	.1320
99-26B	−9.4	.0210	[b].0494	.0428	.0831
99-26C	−4.5	.0216	[b].0494	.0241	.0499
99-27	−.1	.0173	.0084	.0293	.0295
99-28	−4.8	.0177	.0078	.0109	.0518
99-29	−9.7	.0177	[b].0423	.0363	.0902
99-30	−20.9	.0175	.0088	.0053	.1920
99-31	−14.8	.0180	[b].0423	.0329	.1410

[a]At $x/r_n = 35.54$.

[b]Base pressure gage became saturated.

Table VIII. Heating-Rate Data

Run	Heating rates, Btu/ft^2-sec, measured at sensor[a]—															
	2	3	4	5	6	7	8	9	10	11	12	13	14	15	16	17
$\alpha = -20.9°$																
99-30	3.51	9.69	3.65	0.33	1.06	0.58	4.18	10.40	8.07	32.10	54.60	71.40	66.10	8.90	2.46	13.90
$\alpha \approx -14.9°$																
99-26A	3.19	9.49	3.17	.87	.64	1.63	3.75	8.22	5.99	17.20	25.70	33.50	30.60	5.87	3.56	8.67
99-31	4.91	12.70	4.70	2.12	1.99	3.40	5.00	12.00	7.98	26.60	44.50	56.30	51.30	8.16	4.90	12.80
99-24A	3.03	7.30	2.67	.74	.47	1.41	3.09	6.88	4.75	16.00	27.00	36.60	33.80	5.04	2.50	7.92
99-23A	.58	3.35	1.41	.41	.04	.64	1.19	2.10	2.06	5.78	9.80	15.80	16.80	2.16	1.04	3.05
$\alpha \approx -9.5°$																
99-26B	4.10	9.45	3.03	2.28	2.46	4.16	5.69	7.31	6.32	12.30	16.10	19.10	17.10	6.42	3.27	7.60
99-29	6.94	16.10	5.10	3.01	2.41	5.35	8.19	11.90	10.30	21.50	30.00	35.20	32.70	10.20	5.55	12.40
99-24B	4.38	8.78	3.18	1.13	1.28	3.23	4.71	7.35	5.79	12.50	17.20	20.70	19.30	5.96	2.86	7.55
99-23B	1.50	4.21	1.28	.29	.67	1.44	1.80	2.44	2.34	4.33	6.79	8.50	8.90	2.29	.99	2.47
$\alpha \approx -4.6°$																
99-26C	5.24	9.41	3.65	3.40	5.22	6.51	7.40	7.08	6.19	10.00	10.80	11.40	9.82	6.14	3.60	6.93
99-28	9.89	18.00	6.42	5.94	9.17	11.30	12.60	12.40	10.50	18.10	19.70	21.00	19.20	10.50	5.83	10.90
99-24C	6.22	11.00	4.33	3.10	5.04	6.44	7.70	7.85	6.70	10.70	11.60	12.40	10.60	6.72	3.74	7.17
99-23C	1.57	3.31	1.71	1.12	1.96	2.89	3.15	3.32	2.64	4.17	4.75	4.13	4.31	3.05	1.44	2.93
$\alpha \approx 0.0°$																
99-19D	9.78	7.86	6.37	7.25	8.30	9.89	9.57	6.92	6.86	6.60	6.40	5.59	4.87	6.56	6.37	7.40
99-27	12.30	19.00	8.60	8.50	14.90	16.50	16.00	13.30	10.10	14.90	14.50	13.90	12.10	9.95	7.74	10.10
99-8	16.10	13.60	11.86	12.21	13.78	15.79	15.00	10.73	10.73	10.29	10.20	9.42	8.44	10.30	10.10	7.86
99-5	3.96	3.50	12.58	3.01	5.66	6.57	6.41	3.40	3.08	3.71	2.31	2.44	5.81	3.03	11.00	2.36
99-10	9.40	9.55	7.47	7.62	8.67	10.12	9.70	7.49	7.45	7.32	7.19	6.68	5.92	7.17	6.55	7.35
99-4	3.96	3.50	1.99	2.39	4.22	4.82	4.65	2.67	2.44	2.91	1.99	2.08	1.55	2.41	1.35	2.00
99-12D	2.56	2.93	2.99	3.02	3.92	4.60	4.45	3.61	3.70	3.46	2.51	2.82	2.36	3.54	2.94	3.64
99-11	2.95	3.13	3.22	3.21	4.17	4.86	4.77	3.76	3.77	3.73	2.67	2.99	2.82	3.70	3.09	3.77
99-9	1.97	2.56	1.08	1.64	2.42	3.00	2.95	2.18	1.79	1.99	1.81	1.65	.96	1.94	.60	1.55
99-21A	2.33	2.31	1.28	1.96	2.86	3.48	3.25	2.09	1.79	1.85	1.69	1.60	.97	1.83	.85	1.71
99-17	2.12	2.47	1.26	1.71	2.64	3.26	3.15	2.15	1.85	1.98	1.84	1.65	1.00	1.86	.81	1.75
$\alpha \approx 4.5°$																
99-19C	13.30	7.83	10.80	12.50	14.20	15.10	12.00	7.26	6.88	5.29	4.75	4.00	3.57	6.42	10.90	7.67
99-16	24.80	14.10	19.50	20.20	22.70	23.80	19.10	11.70	11.60	8.76	7.92	7.24	6.76	10.60	17.50	11.60
99-12C	5.98	4.25	6.17	5.92	6.38	7.02	5.49	3.35	3.27	2.42	1.88	1.54	1.10	2.80	5.78	2.87
99-21B	3.35	2.41	2.18	3.30	4.68	5.14	4.29	2.43	2.11	1.66	1.26	.98	.59	2.00	1.47	2.12
$\alpha \approx 9.5°$																
99-19B	20.10	7.41	17.30	24.30	25.00	23.40	15.70	7.08	7.63	3.86	2.80	2.41	2.95	6.82	18.30	8.73
99-13	28.90	11.50	27.80	32.60	37.00	35.00	22.40	10.30	12.30	5.81	3.65	3.25	5.15	11.10	29.80	13.60
99-12B	8.72	3.72	10.30	10.40	10.60	10.20	6.56	3.17	2.80	1.68	1.00	.37	1.29	2.49	10.40	3.12
99-21C	5.42	2.57	3.98	6.26	8.41	8.50	6.04	2.83	2.49	1.59	1.00	.46	.99	2.36	2.82	2.49
$\alpha \approx 15.0°$																
99-19A	26.40	6.39	24.10	33.30	37.00	33.20	20.50	7.60	8.79	2.93	0.99	0.93	2.90	7.93	27.80	11.50
99-7	35.60	8.73	39.77	55.48	62.18	54.28	31.14	10.38	11.94	4.11	1.20	1.16	4.29	11.60	50.60	10.70
99-6	13.00	3.15	35.54	41.61	45.18	39.02	23.13	6.04	5.36	2.47	.62	.72	2.94	6.82	51.10	11.50
99-15	24.90	5.30	30.50	38.50	44.10	39.30	22.10	7.29	6.92	2.75	.97	.77	2.92	6.03	35.10	11.60
99-12A	11.00	3.09	16.80	18.50	19.40	16.70	9.00	3.43	2.75	1.39	.58	.30	1.62	2.62	17.70	4.21
99-21D	6.78	2.41	5.90	9.41	11.90	11.60	7.29	2.96	2.41	1.30	.58	.24	1.43	2.20	8.05	2.62
$\alpha = 20.40°$																
99-18	43.80	6.55	47.00	69.70	72.80	60.50	35.10	11.40	10.80	3.34	0.47	1.47	3.51	9.47	68.50	14.60

[a]See figure 9(b) for sensor locations.

Table VIII. Continued

Run	Heating rates, Btu/ft^2-sec, measured at sensor[a]—																
	18	19	20	21	22	23	24	25	26	27	28	29	30	31	32	33	34
$\alpha = -20.9°$																	
99-30	1.53	.90	(b)	(b)	.75	1.48	6.76	12.10	13.00	35.20	58.70	61.00	60.00	58.20	12.30	1.34	12.30
$\alpha \approx -14.9°$																	
99-26A	3.58	2.44	2.10	2.01	2.08	2.07	5.65	8.39	9.35	21.70	31.00	32.20	29.90	29.60	8.80	4.23	8.89
99-31	5.00	4.20	3.50	3.80	3.40	5.18	7.25	13.20	14.00	32.60	51.00	52.10	48.00	45.80	13.00	4.80	13.20
99-24A	2.09	1.23	1.06	.93	.62	1.06	4.58	9.10	9.28	21.40	32.20	34.20	32.30	33.00	9.00	1.78	8.90
99-23A	1.06	.80	.55	.45	.30	.57	2.30	4.99	4.41	10.50	16.30	17.80	16.70	17.60	4.60	1.00	4.43
$\alpha \approx -9.5°$																	
99-26B	3.33	3.08	2.27	2.22	2.73	3.66	5.70	6.59	8.43	16.90	21.50	21.00	18.20	16.70	8.08	3.68	8.04
99-29	5.70	5.70	3.40	3.50	4.00	5.90	7.79	11.10	14.20	29.60	42.20	41.50	35.40	34.20	13.00	5.70	14.50
99-24B	2.73	2.94	1.33	1.10	.75	1.64	4.41	7.23	9.02	17.70	24.30	24.30	21.20	20.10	8.56	2.71	9.31
99-23B	.81	1.70	.62	.49	.22	.82	2.00	3.38	3.86	8.31	11.90	12.50	10.80	10.60	3.62	.72	4.76
$\alpha \approx -4.5°$																	
99-26C	3.47	3.95	3.28	3.42	3.69	5.33	7.69	6.57	7.49	12.40	13.80	12.70	10.30	9.51	7.09	3.26	7.06
99-28	5.09	5.31	4.19	4.47	4.78	7.40	11.10	10.10	11.70	20.80	25.20	23.70	19.00	18.50	11.20	4.90	11.90
99-24C	3.36	3.73	2.58	2.68	3.31	4.81	7.13	6.85	7.57	12.50	14.30	13.50	10.80	10.20	7.23	3.19	7.74
99-23C	1.48	1.26	.59	.52	1.55	2.07	3.07	3.38	3.19	4.96	5.65	5.31	4.81	4.92	3.05	1.44	3.72
$\alpha \approx 0.0°$																	
99-19D	5.52	6.74	11.40	8.31	10.50	10.30	11.30	9.14	7.84	7.67	7.22	6.89	4.82	4.94	7.16	5.50	6.28
99-27	6.90	8.00	9.21	9.15	11.80	15.80	18.40	12.10	10.20	14.90	14.80	12.70	9.82	9.94	9.88	6.90	10.10
99-8	8.82	10.30	(b)	14.70	15.60	15.10	18.20	13.20	11.00	10.50	9.99	9.52	7.42	7.78	10.70	9.41	9.87
99-5	9.58	5.80	3.57	3.85	6.98	7.20	8.84	5.75	3.74	3.66	2.72	2.54	5.51	7.06	3.87	10.20	3.49
99-10	5.80	6.77	8.06	8.76	9.94	10.20	12.10	9.28	7.75	7.49	6.99	6.59	5.13	5.23	7.35	6.18	7.24
99-4	1.30	2.10	2.56	2.82	5.05	5.29	6.34	3.98	2.83	3.01	2.38	2.13	1.31	1.20	2.92	1.59	2.66
99-12D	2.59	2.96	3.50	2.12	4.07	4.20	4.69	4.04	3.94	3.69	3.29	2.77	2.42	2.54	3.70	2.85	3.87
99-11	2.88	3.05	2.87	3.00	4.00	4.28	4.86	4.26	3.98	3.81	3.39	2.97	2.58	2.66	3.85	3.11	4.00
99-9	.65	1.51	(b)	2.06	3.20	3.39	3.65	2.69	2.21	2.11	1.99	1.65	.90	.63	2.63	1.07	2.29
99-21A	.69	1.24	1.79	2.50	3.60	3.63	3.84	2.49	1.69	1.72	1.58	1.26	.65	.46	1.83	.60	1.62
99-17	.58	1.14	2.19	1.87	3.27	3.38	3.68	2.57	1.78	1.86	1.72	1.41	.73	.54	1.83	.55	1.65
$\alpha \approx 4.6°$																	
99-19C	9.62	11.90	18.10	14.70	19.90	16.60	15.90	11.20	8.78	6.22	5.02	4.62	3.18	3.59	7.93	9.83	7.62
99-16	15.60	19.50	25.10	27.90	32.10	26.20	26.50	16.80	12.60	8.59	6.75	6.28	4.72	5.60	11.70	17.00	12.30
99-12C	5.43	6.79	7.97	7.03	8.53	7.28	6.59	4.02	3.26	2.08	1.30	.57	.88	1.53	2.73	5.95	3.85
99-21B	1.06	1.92	4.12	3.41	5.83	5.39	5.14	2.87	2.13	1.63	1.16	.65	.21	.79	2.13	.79	1.97
$\alpha \approx 9.6°$																	
99-19B	16.20	20.20	26.00	25.80	28.60	22.10	20.70	11.70	10.20	5.27	2.40	1.63	2.31	3.93	9.22	18.30	8.42
99-13	25.40	33.30	37.50	44.50	44.60	35.50	31.00	16.80	15.80	6.93	2.54	2.20	3.57	5.61	14.40	29.60	13.50
99-12B	9.53	11.70	15.10	15.40	16.70	13.00	11.10	5.71	6.07	2.25	.62	.96	1.47	1.21	4.94	10.50	5.69
99-21C	2.84	4.40	7.30	6.60	8.68	7.25	6.31	3.15	2.60	1.49	.56	.45	1.32	1.07	2.60	5.10	2.47
$\alpha \approx 15.0°$																	
99-19A	26.30	30.40	32.70	37.20	36.40	27.20	22.20	11.00	10.40	5.15	1.64	2.11	1.64	2.74	9.40	29.80	8.35
99-7	44.01	51.70	(b)	67.13	56.51	43.63	35.20	16.53	14.91	6.91	.53	1.15	1.78	2.38	14.80	49.40	12.90
99-6	45.18	52.59	54.92	64.61	58.93	42.80	34.50	16.31	14.40	7.27	1.69	2.29	1.85	3.35	13.60	50.70	12.50
99-15	30.00	36.10	37.10	45.50	41.20	30.40	25.20	11.90	11.60	5.00	1.20	1.53	1.31	2.20	10.00	33.80	9.44
99-12A	15.50	18.20	20.80	23.30	21.90	16.10	12.70	5.93	6.76	2.69	.67	.88	.99	1.25	6.21	16.90	5.54
99-21D	13.90	15.40	16.50	17.30	15.40	11.40	8.65	3.79	3.29	1.66	.45	.99	.96	1.04	3.05	17.30	3.59
$\alpha = 20.4°$																	
99-18	57.10	61.40	58.80	72.40	59.70	46.20	33.50	14.50	14.00	5.69	1.72	1.64	.82	1.60	12.80	60.10	11.40

[a]See figure 9(b) for sensor locations.
[b]Instrumentation not functional.

Table VIII. Continued

Run	Heating rates, Btu/ft^2-sec, measured at sensor[a]—																
	35	36	37	38	39	40	41	42	43	44	45	46	47	48	49	50	51
$\alpha = -20.9°$																	
99-30	1.62	.54	.70	.70	1.45	1.79	6.46	16.60	12.40	13.20	(b)	56.00	67.50	68.80	68.30	11.90	1.76
$\alpha \approx -14.9°$																	
99-26A	4.15	3.47	3.08	3.53	3.68	5.80	7.96	12.70	9.00	9.61	13.50	29.60	34.60	34.30	34.60	8.83	3.95
99-31	4.70	3.60	3.50	3.60	5.21	9.00	10.70	18.40	13.40	14.00	(b)	47.80	56.90	55.90	56.70	12.70	5.30
99-24A	1.71	.44	.63	.99	.54	1.98	5.40	11.50	9.11	9.54	14.40	29.90	36.20	35.90	36.00	8.85	1.77
99-23A	.97	.31	.41	.60	.29	.86	2.55	5.50	4.83	4.76	7.52	14.40	18.60	18.10	18.10	4.54	.57
$\alpha \approx -9.5°$																	
99-26B	3.40	2.65	2.37	2.89	3.89	6.53	8.76	11.40	8.15	8.98	11.10	21.00	22.80	21.60	20.30	8.24	3.45
99-29	5.10	3.90	3.80	4.40	6.20	10.50	12.00	19.20	14.50	15.80	(b)	40.40	45.50	42.70	41.10	14.20	5.40
99-24B	2.55	1.43	.85	1.17	.70	2.81	5.98	11.30	9.38	10.40	13.20	23.90	26.90	25.10	23.30	9.60	2.69
99-23B	.76	.95	.55	.35	.23	1.36	2.88	5.50	5.14	5.63	7.24	11.80	13.60	12.70	11.70	5.05	.89
$\alpha \approx -4.5°$																	
99-26C	3.05	3.61	3.48	2.29	3.47	7.23	8.70	10.10	7.32	8.30	9.39	14.40	14.60	12.20	10.50	7.74	3.15
99-28	4.70	5.24	5.06	1.79	4.21	9.89	13.10	16.80	12.20	14.00	16.50	27.10	28.80	23.90	21.40	12.80	4.93
99-24C	3.07	3.60	3.53	.98	3.11	6.78	8.63	10.50	8.05	9.22	10.60	16.10	16.30	13.40	11.80	8.49	3.21
99-23C	1.44	1.96	.73	.27	1.54	2.97	3.85	4.68	4.08	4.72	5.44	7.20	7.40	6.20	5.56	3.73	1.38
$\alpha \approx 0.0°$																	
99-19D	5.02	(b)	9.02	10.30	11.30	14.70	14.30	13.40	8.11	8.39	7.71	7.68	6.66	5.73	4.24	7.07	4.80
99-27	6.50	8.20	9.60	10.80	13.10	24.30	23.40	21.70	12.00	11.70	11.80	15.20	14.30	11.30	10.00	10.70	7.00
99-8	9.62	(b)	14.40	16.30	18.30	23.30	21.90	20.40	12.40	12.60	11.30	11.10	9.41	8.07	6.12	11.30	9.35
99-5	10.22	(b)	4.27	5.14	6.17	10.56	9.92	5.53	5.16	5.00	4.24	4.25	2.47	6.14	6.77	4.51	9.76
99-10	6.07	(b)	9.69	10.50	12.40	16.20	15.60	14.30	9.01	9.15	8.16	8.03	6.71	5.76	4.47	8.00	6.02
99-4	2.09	(b)	2.89	3.44	4.03	7.44	7.00	4.19	3.32	3.50	3.27	3.37	2.15	1.87	1.91	3.16	3.08
99-12D	2.89	(b)	3.35	3.10	4.70	6.36	6.46	5.96	4.68	4.61	4.12	3.93	3.22	2.72	2.28	4.19	2.79
99-11	3.11	(b)	3.65	3.28	5.20	7.21	7.13	6.81	4.94	4.86	4.28	4.09	3.37	2.87	2.37	4.27	3.25
99-9	1.55	(b)	2.29	2.39	3.80	4.82	4.47	3.82	2.75	2.86	2.54	2.34	1.85	1.38	.86	3.10	1.85
99-21A	.51	(b)	1.90	2.29	3.80	4.94	4.46	3.28	1.85	1.80	1.69	1.63	1.19	.74	.32	1.65	.57
99-17	.54	(b)	1.73	2.18	3.60	4.72	4.33	3.22	1.89	1.87	1.81	1.83	1.36	.91	.42	1.69	.57
$\alpha \approx 4.6°$																	
99-19C	9.03	(b)	14.80	17.50	17.10	20.30	17.10	15.50	9.51	9.29	6.70	5.39	4.33	3.23	3.10	8.20	9.20
99-16	18.30	(b)	28.90	32.50	35.40	40.20	32.00	27.70	16.80	15.80	10.20	7.28	5.72	4.70	4.57	13.40	18.70
99-12C	6.25	(b)	9.78	10.20	11.30	12.40	9.72	7.29	5.93	5.48	2.84	1.59	.47	.71	1.29	4.18	6.45
99-21B	.79	(b)	3.44	3.93	5.81	6.77	5.39	3.41	2.24	2.31	1.61	1.21	.45	.37	.80	2.12	1.60
$\alpha \approx 9.6°$																	
99-19B	19.80	(b)	25.70	27.00	24.90	27.00	20.00	16.30	10.50	9.82	5.76	3.16	1.64	2.27	3.42	8.46	19.50
99-13	33.60	(b)	43.20	44.30	44.90	46.30	32.70	24.00	16.50	16.00	8.55	3.93	2.17	2.47	4.28	13.90	35.10
99-12B	11.40	(b)	14.40	16.10	16.40	16.80	11.50	7.08	6.68	6.29	2.80	1.11	.40	.79	.97	5.48	11.70
99-21C	9.00	(b)	10.90	9.50	10.80	10.90	7.50	4.15	3.15	3.42	1.67	.77	.41	1.10	.71	3.12	11.30
$\alpha \approx 15.0°$																	
99-19A	32.70	(b)	34.60	35.10	34.00	33.80	22.40	14.60	11.00	9.95	5.15	2.23	1.25	1.96	2.46	8.54	33.00
99-7	56.20	(b)	62.31	61.40	59.20	57.60	36.50	22.20	15.70	14.30	6.95	2.21	.98	.39	2.21	13.30	57.90
99-6	56.20	(b)	59.50	60.50	53.80	55.40	35.70	18.40	15.50	14.00	6.88	2.93	1.70	1.96	2.98	12.40	56.40
99-15	37.70	(b)	41.00	41.30	40.60	39.40	25.00	13.90	11.50	11.00	4.84	1.87	1.02	.68	1.75	9.09	37.70
99-12A	18.20	(b)	20.20	21.60	21.10	20.50	12.60	6.31	6.58	6.12	2.43	.94	.39	.46	1.15	5.58	18.30
99-21D	19.40	(b)	21.10	19.70	19.30	17.70	10.60	5.30	4.52	4.61	1.92	.70	.40	.36	1.03	4.10	18.70
$\alpha = 20.4°$																	
99-18	61.00	(b)	65.50	66.70	63.30	59.60	36.10	19.60	19.60	13.90	5.40	1.67	1.06	1.59	1.91	12.20	65.00

[a]See figure 9(b) for sensor locations.
[b]Instrumentation not functional.

Table VIII. Concluded

Run	Heating rates, Btu/ft^2-sec, measured at sensor [a]—																
	52	53	54	55	56	57	58	59	60	61	62	63	64	65	66	67	68
$\alpha = -20.9°$																	
99-30	12.50	1.54	1.70	1.68	1.62	1.20	1.58	6.49	16.00	13.00	14.40	32.20	55.40	59.60	68.00	61.00	(b)
$\alpha \approx -14.9°$																	
99-26A	9.30	4.68	5.19	4.87	5.00	5.01	7.73	9.65	12.80	9.61	10.90	20.00	30.80	30.80	33.70	32.20	(b)
99-31	13.30	6.50	5.60	5.90	7.00	6.70	9.14	12.20	17.00	13.80	15.10	30.10	48.10	49.40	54.70	49.90	(b)
99-24A	8.89	1.77	.85	.75	.66	.54	1.93	4.82	10.30	9.31	10.00	18.90	29.70	31.60	34.70	33.40	(b)
99-23A	4.45	1.67	1.16	1.26	1.58	.97	.49	2.28	4.80	4.95	5.08	9.53	15.70	16.80	18.10	17.30	(b)
$\alpha \approx -9.5°$																	
99-26B	8.84	4.26	3.67	4.05	4.83	4.67	6.88	9.61	11.90	8.97	10.50	16.60	22.10	21.20	21.60	20.00	(b)
99-29	15.30	7.10	6.40	7.20	8.40	7.10	11.20	14.80	15.00	19.30	17.50	28.70	41.00	40.30	41.80	38.80	(b)
99-24B	10.10	2.69	.74	1.63	1.19	.58	3.14	6.29	11.10	10.00	11.60	18.20	24.80	24.50	24.50	22.60	(b)
99-23B	5.47	1.18	1.33	1.73	1.59	1.00	.80	2.96	5.47	5.50	6.29	9.06	12.70	12.90	12.70	11.60	(b)
$\alpha \approx -4.5°$																	
99-26C	8.47	3.31	4.06	4.02	3.65	4.48	7.53	9.12	10.60	8.50	10.10	13.90	15.90	14.30	13.20	10.50	(b)
99-28	14.30	4.83	6.37	4.38	(b)	4.85	10.70	14.40	17.70	14.20	17.00	24.50	30.30	26.90	25.20	20.70	(b)
99-24C	9.29	3.11	4.14	3.33	1.07	3.64	7.48	9.34	11.10	9.30	11.00	15.60	17.80	15.70	14.00	11.60	(b)
99-23C	4.89	1.43	2.15	1.07	.65	1.61	3.39	4.37	5.25	4.94	5.79	7.47	8.45	7.82	6.84	5.73	(b)
$\alpha \approx 0.0°$																	
99-19D	7.50	5.00	7.95	8.10	8.30	11.00	14.00	12.00	12.90	9.02	9.54	8.81	7.22	7.86	5.47	4.41	8.07
99-27	11.90	6.60	9.60	11.00	11.10	13.30	25.10	24.50	22.70	13.90	14.30	18.30	18.40	14.30	12.40	7.40	(b)
99-8	11.90	8.97	13.80	14.80	15.50	20.60	24.70	21.50	21.20	15.00	14.50	13.20	10.30	11.10	7.50	6.38	12.90
99-5	5.77	7.60	7.48	7.13	6.05	11.31	13.00	9.83	10.30	10.20	9.36	7.82	5.69	6.08	6.11	7.13	8.99
99-10	8.69	6.02	9.67	10.20	10.80	14.50	17.80	15.60	15.20	10.90	10.90	9.72	7.58	8.02	5.54	4.58	9.02
99-4	3.79	3.19	4.34	4.03	3.67	7.01	8.38	6.97	6.95	5.90	5.90	5.02	3.78	4.02	2.69	3.76	5.02
99-12D	4.58	2.72	3.93	4.14	4.02	6.17	8.10	7.24	6.92	5.66	5.57	4.97	4.03	3.89	2.71	2.31	4.82
99-11	4.81	3.26	4.77	5.05	4.81	7.12	8.91	8.20	7.83	6.06	5.89	5.27	4.22	4.16	2.88	2.41	4.93
99-9	2.93	1.88	2.47	2.60	2.74	4.28	5.08	4.62	4.38	3.52	3.66	3.30	2.55	2.44	1.60	1.33	3.73
99-21A	1.76	.74	1.79	1.89	2.22	3.75	4.46	3.89	3.01	2.19	2.11	1.77	1.46	1.43	.76	.59	2.01
99-17	1.82	.58	1.58	1.75	2.04	3.67	4.43	3.70	3.18	2.19	2.17	1.94	1.65	1.65	.88	.68	2.00
$\alpha \approx 4.6°$																	
99-19C	8.74	10.00	14.00	14.00	14.80	18.10	20.90	15.90	15.60	10.80	10.70	7.78	5.12	5.19	3.41	3.14	9.00
99-16	15.10	21.40	26.80	28.00	29.60	36.90	39.60	30.30	27.40	19.00	18.40	12.30	7.46	6.68	4.73	5.03	15.20
99-12C	5.61	6.84	9.32	9.36	9.95	12.40	13.80	10.50	8.99	7.25	6.77	4.11	2.06	1.07	.91	1.34	5.37
99-21B	2.44	3.52	4.70	4.74	4.67	6.20	6.77	5.02	3.40	3.66	3.48	2.06	1.19	.68	.67	.78	2.92
$\alpha \approx 9.6°$																	
99-19B	9.15	20.60	21.00	21.10	23.90	25.40	26.70	18.40	16.10	11.50	11.40	6.41	3.06	2.27	2.61	3.14	9.02
99-13	14.60	36.80	37.80	38.20	40.60	44.50	43.80	29.80	22.90	17.90	17.20	9.57	4.29	2.89	2.92	4.67	14.40
99-12B	5.64	12.90	14.10	13.70	14.40	19.60	21.90	14.40	9.04	7.21	6.49	3.21	.89	1.46	1.14	1.00	5.33
99-21C	4.33	12.70	13.00	12.50	13.00	15.00	15.70	11.10	6.28	5.57	6.20	2.77	.65	1.28	1.13	.97	5.42
$\alpha \approx 15.0°$																	
99-19A	9.24	33.00	29.80	31.40	34.20	35.00	33.30	22.00	13.50	12.00	11.20	5.50	2.20	1.59	1.68	2.95	9.18
99-7	13.00	51.50	52.30	54.10	56.80	56.60	51.30	32.24	20.00	17.40	14.90	7.27	1.18	.98	1.82	3.51	13.50
99-6	13.60	46.30	47.90	48.40	52.90	54.90	50.00	31.80	19.20	17.10	14.60	6.96	2.45	1.53	2.01	3.42	13.00
99-15	9.85	39.80	35.20	35.60	36.00	38.80	35.10	21.10	12.80	12.60	11.70	5.02	1.71	.99	.91	1.99	9.18
99-12A	5.58	19.70	19.70	19.00	22.10	32.70	34.60	20.40	10.20	7.19	6.29	2.54	.66	1.45	1.23	1.24	5.45
99-21D	4.82	18.00	18.90	21.50	(b)	(b)	(b)	(b)	(b)	8.20	6.63	2.47	.83	1.73	1.26	1.72	5.64
$\alpha = 20.4°$																	
99-18	13.10	64.20	55.00	58.00	63.60	59.50	53.20	31.70	17.60	16.10	15.60	5.87	1.20	1.96	1.51	2.10	12.80

[a]See figure 9(b) for sensor locations.
[b]Instrumentation not functional.

Table IX. Effect of Diameter of Boundary-Layer Trips

$[x/r_n \geq 16.88]$

d, in.	N_{Re}, ft^{-1}	T_t, °R	Type of flow for α, deg, of—								
			0	4.6	9.6	15.0	20.4	−4.5	−9.5	−14.9	−20.9
0	0.4×10^6	3330	Laminar	Transitional	Transitional	Transitional					
	.9	3330	Transitional								
	1.5	3330	Transitional			Turbulent					
0.094	0.4×10^6	3330	Transitional								
	.9	3330	Turbulent			Turbulent					
	1.5	3330	Turbulent	Turbulent	Turbulent	Turbulent	Turbulent	Turbulent	Turbulent	Turbulent	Turbulent
	1.7	2410	Turbulent	Turbulent	Turbulent	Turbulent		Turbulent	Turbulent	Turbulent	
0.190	0.4×10^6	3300	Transitional	Turbulent	Turbulent	Turbulent		Turbulent	Turbulent	Turbulent	
	.9	3300						Turbulent	Turbulent	Turbulent	

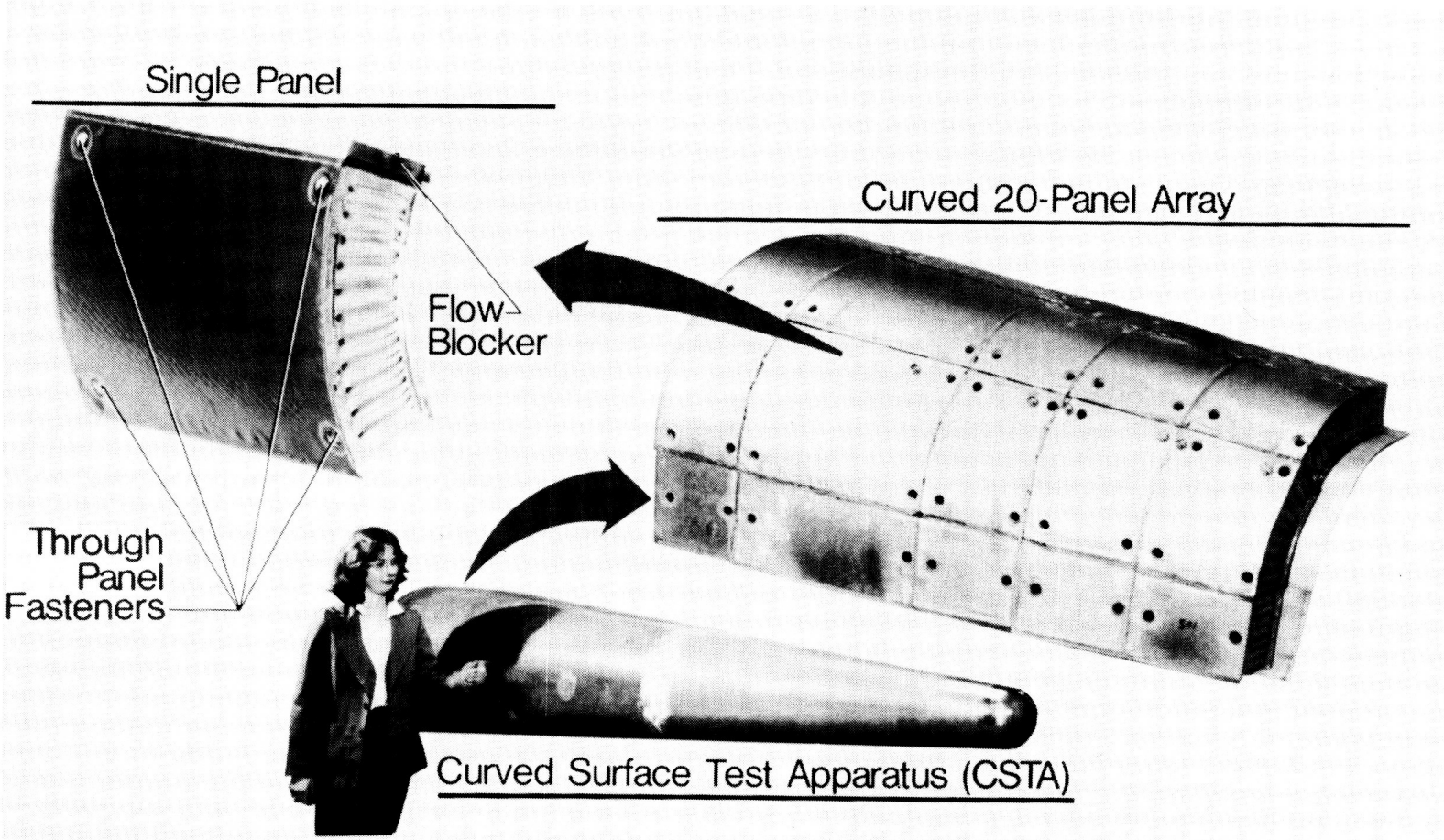

L-84-3717

Figure 1. Curved metallic tile system with CSTA used as test bed.

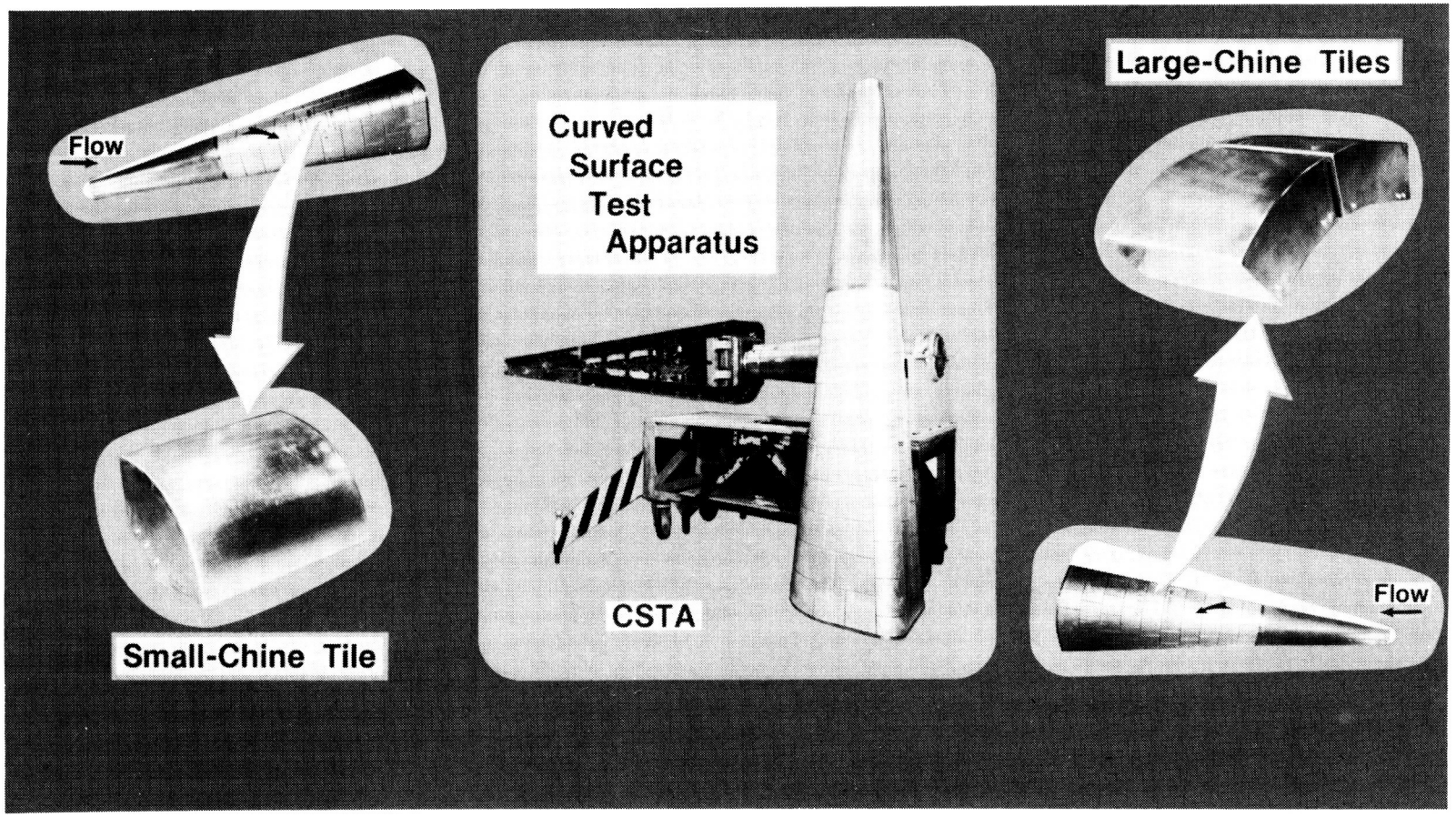

L-85-898

Figure 2. Chine tile-gap heating model with CSTA used as test bed. (From ref. 7.)

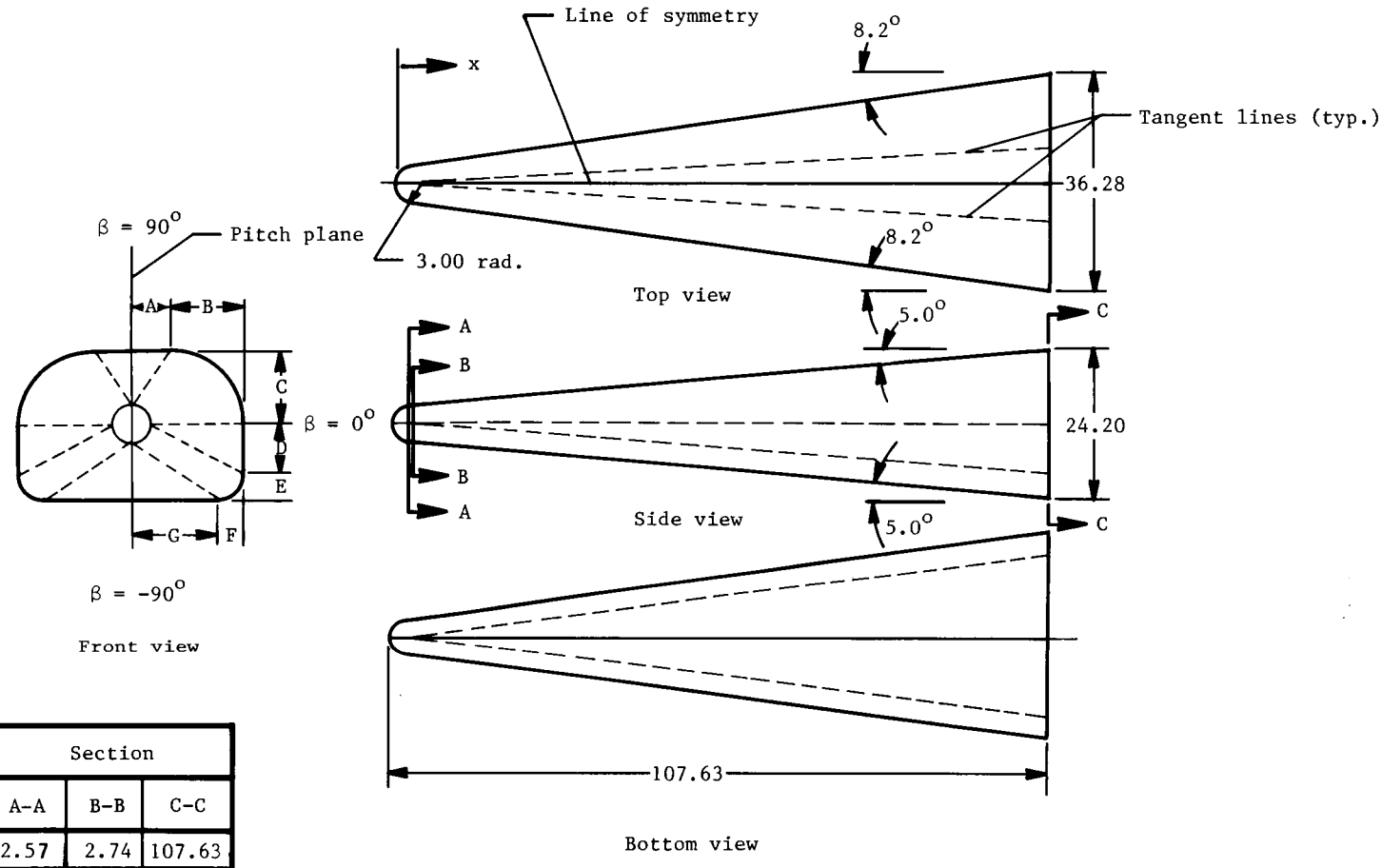

	Section		
	A-A	B-B	C-C
x	2.57	2.74	107.63
A	0	0	6.04
B	2.90	2.99	12.10
C	2.90	2.99	12.10
D	0	.01	8.09
E	2.90	2.98	4.01
F	2.90	2.99	4.01
G	0	0	14.13

Figure 3. Schematic of model. Dimensions are in inches unless otherwise indicated.

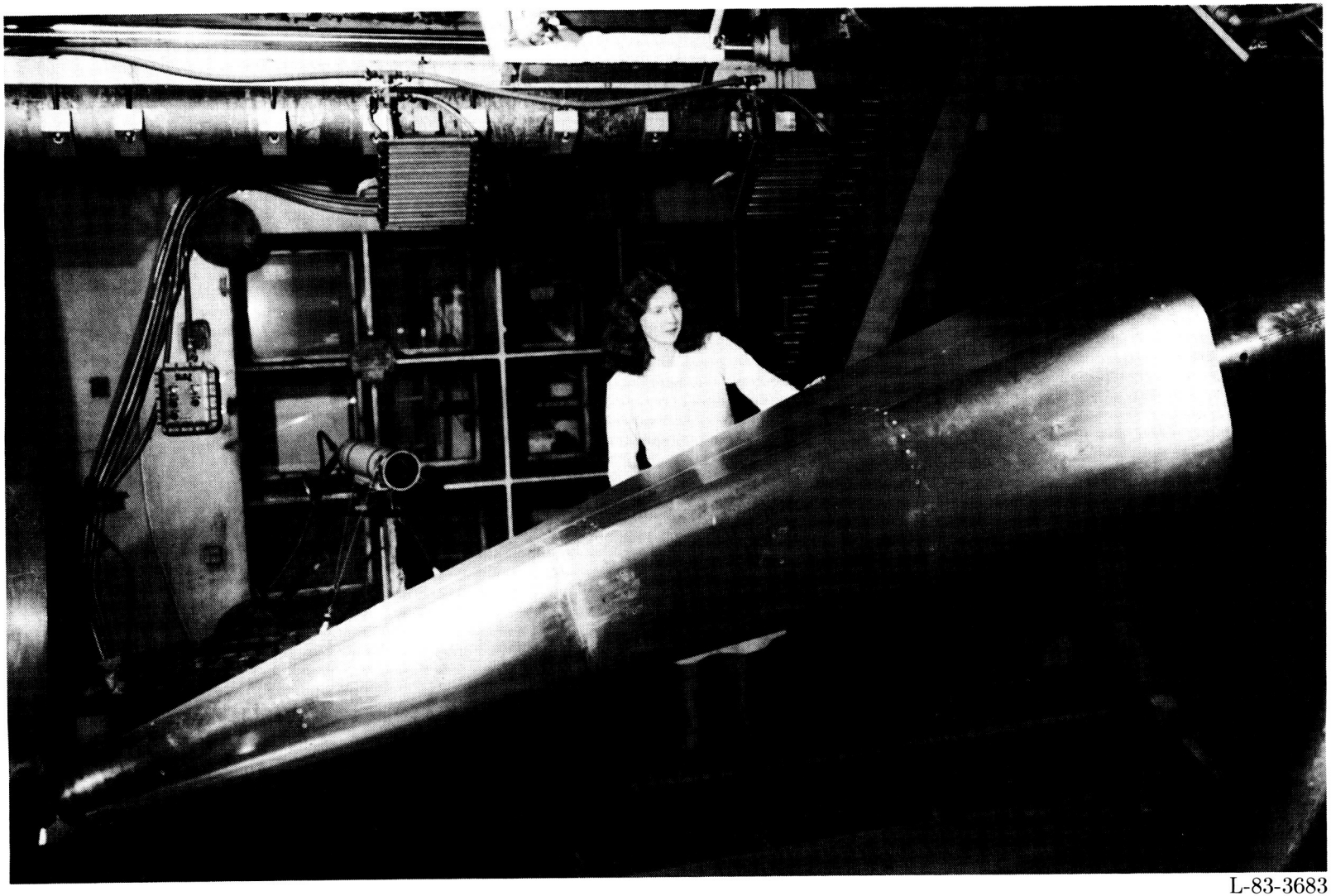

L-83-3683

Figure 4. Model mounted on sting in Langley 8-Foot High-Temperature Tunnel.

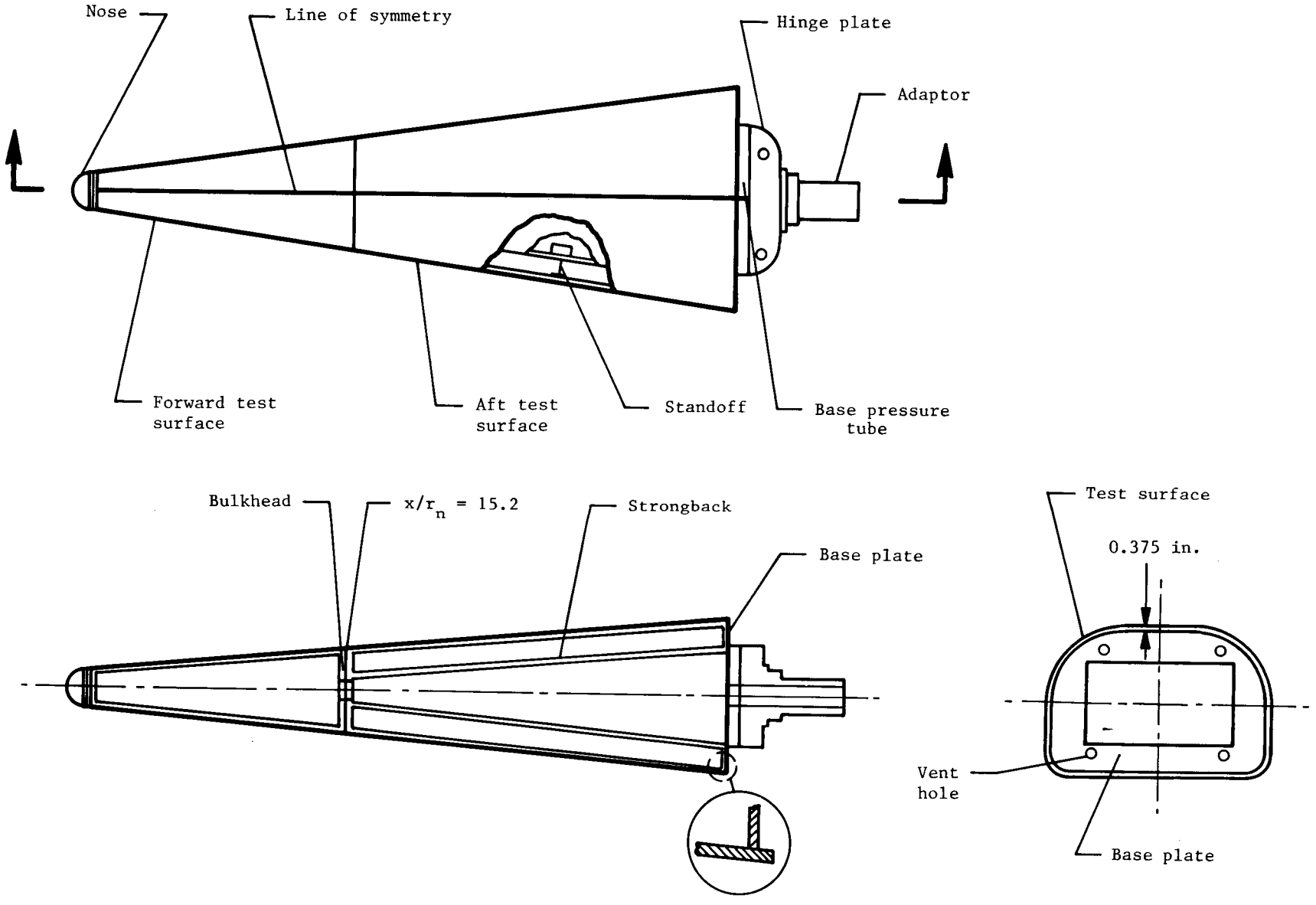

Figure 5. Model structural components.

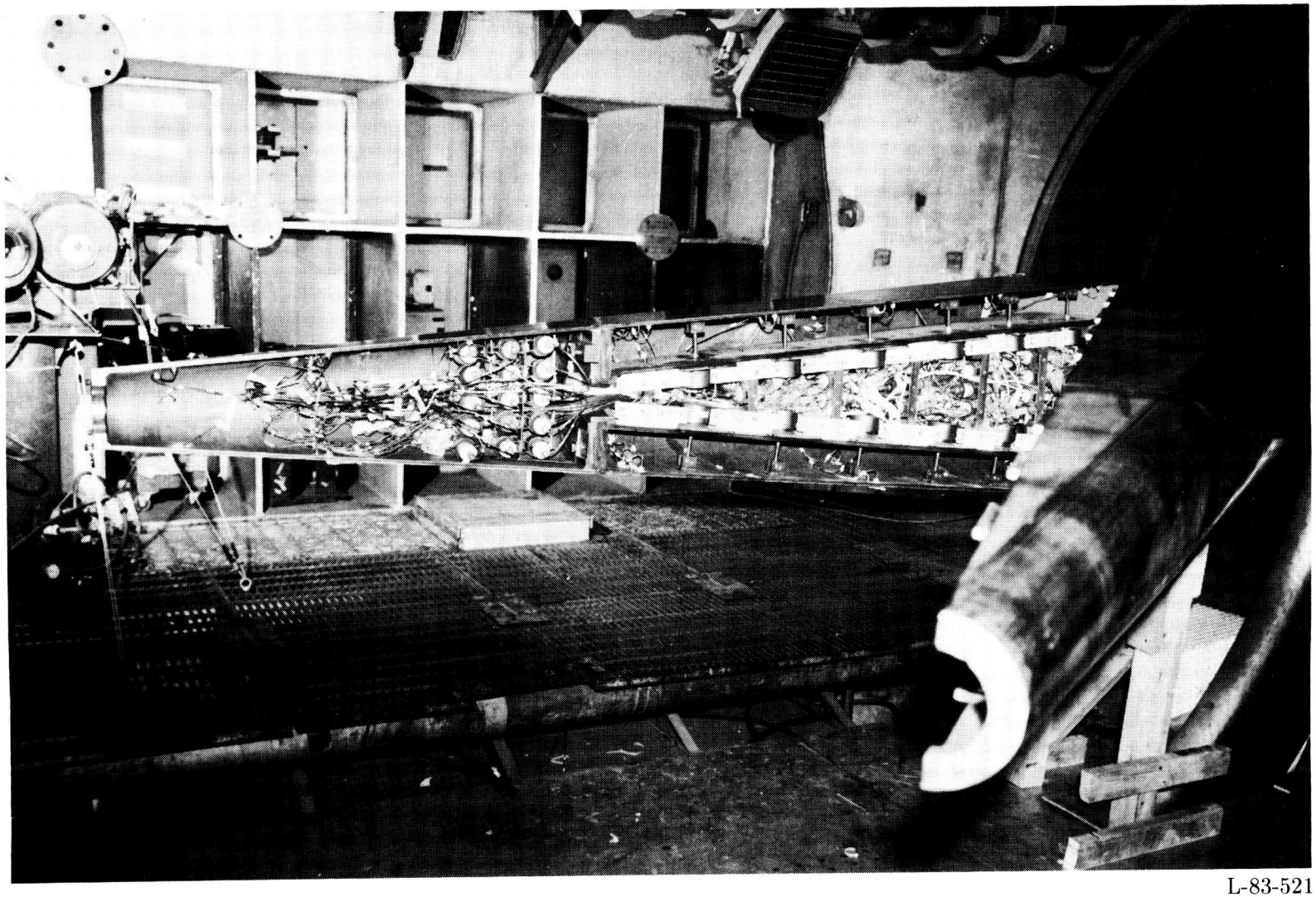

L-83-521

Figure 6. Model opened to allow access to instrumentation.

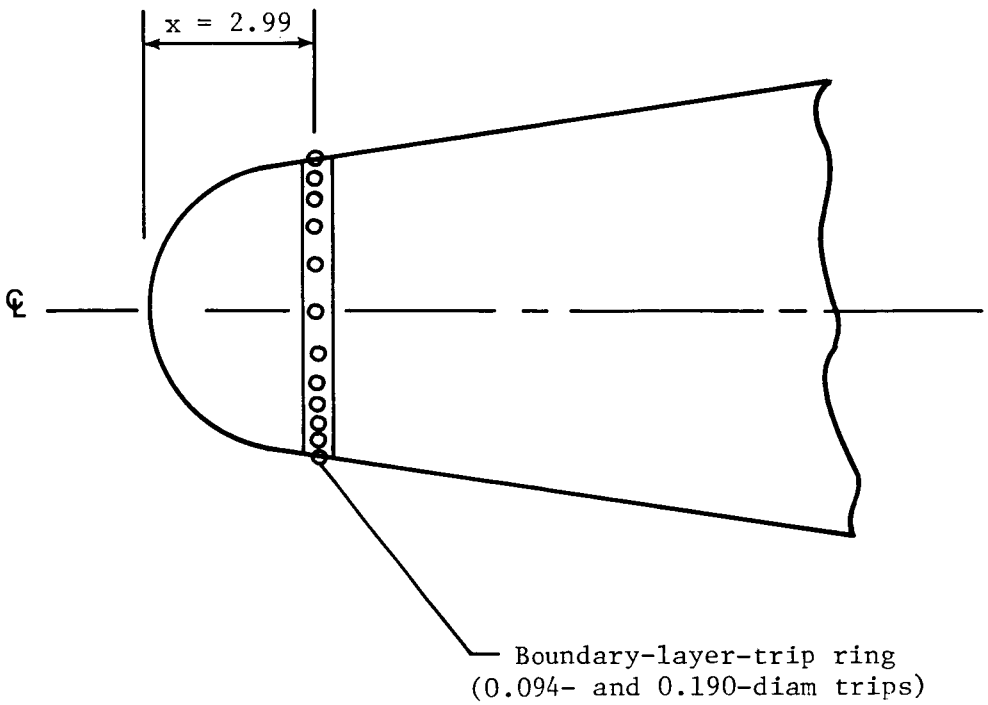

Figure 7. Model nose region showing boundary-layer-trip ring. Dimensions are in inches.

Probe locations

No.	y, in.
1	0.20
2	.40
3	.80
4	1.25
5	1.75
6	2.25
7	2.75

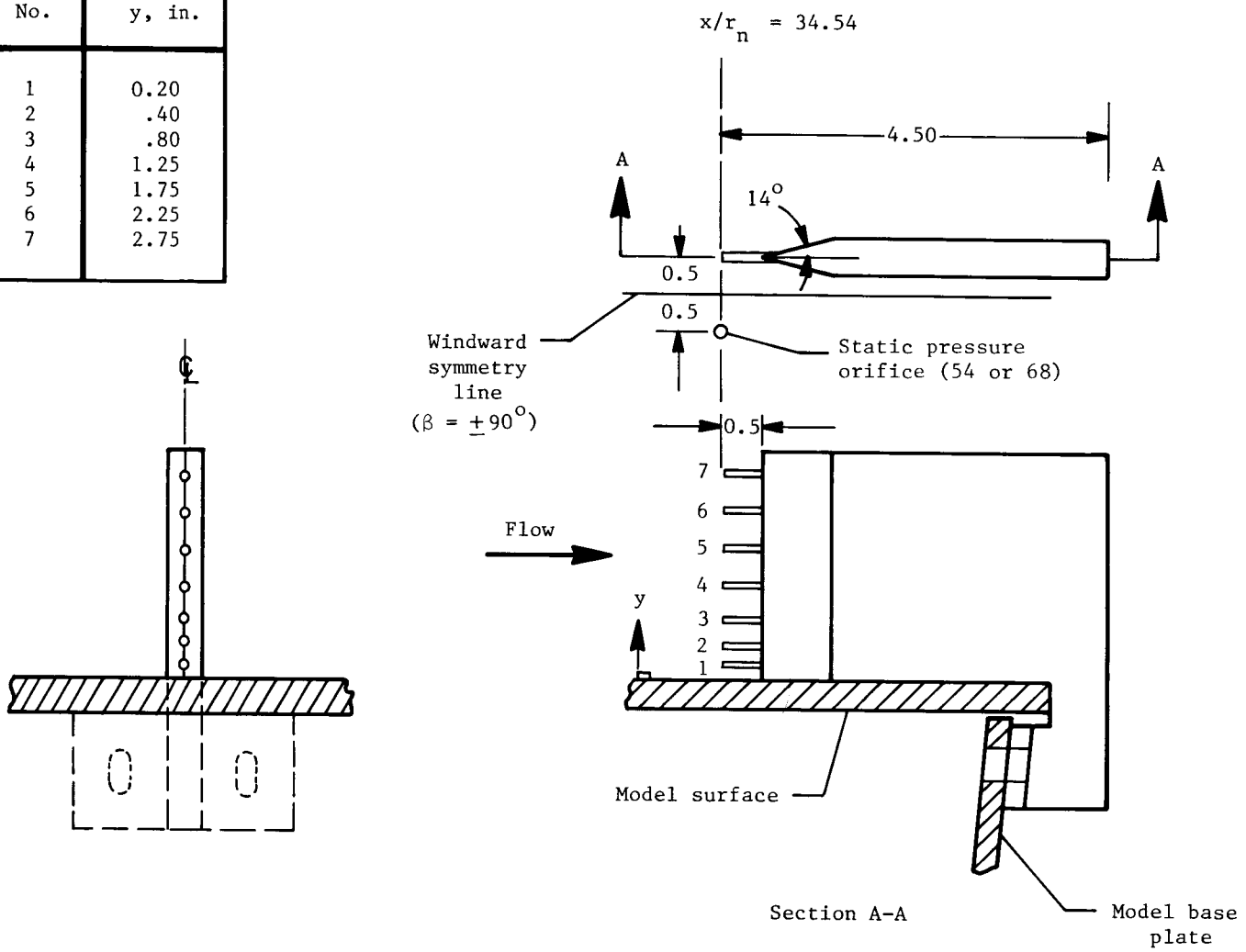

Figure 8. Shock-layer pitot rake. Dimensions are in inches unless otherwise noted.

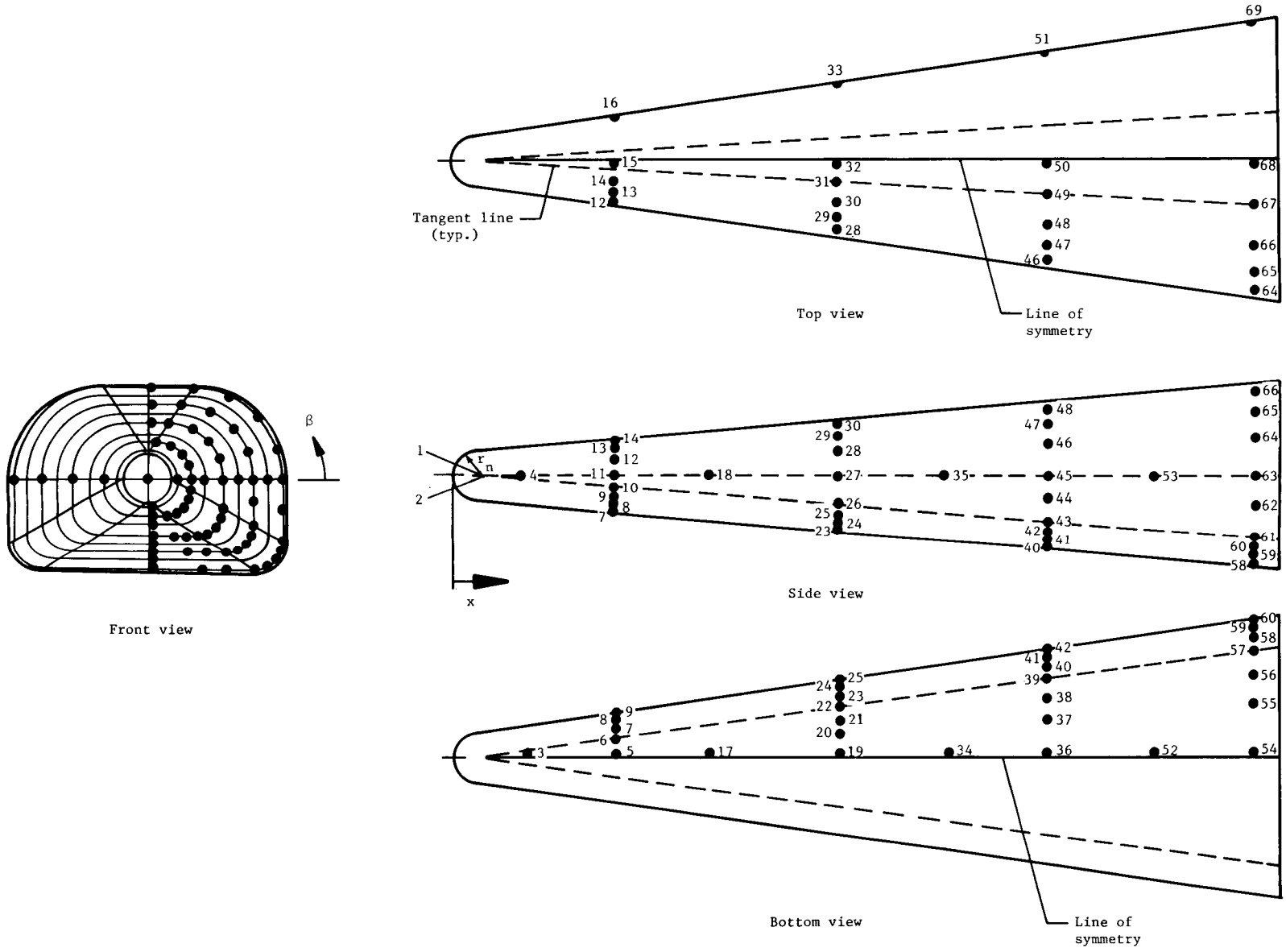

(a) Pressure orifices.

Figure 9. Surface instrumentation distribution on model.

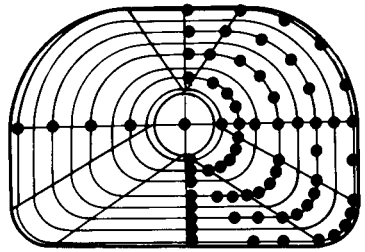

Front view

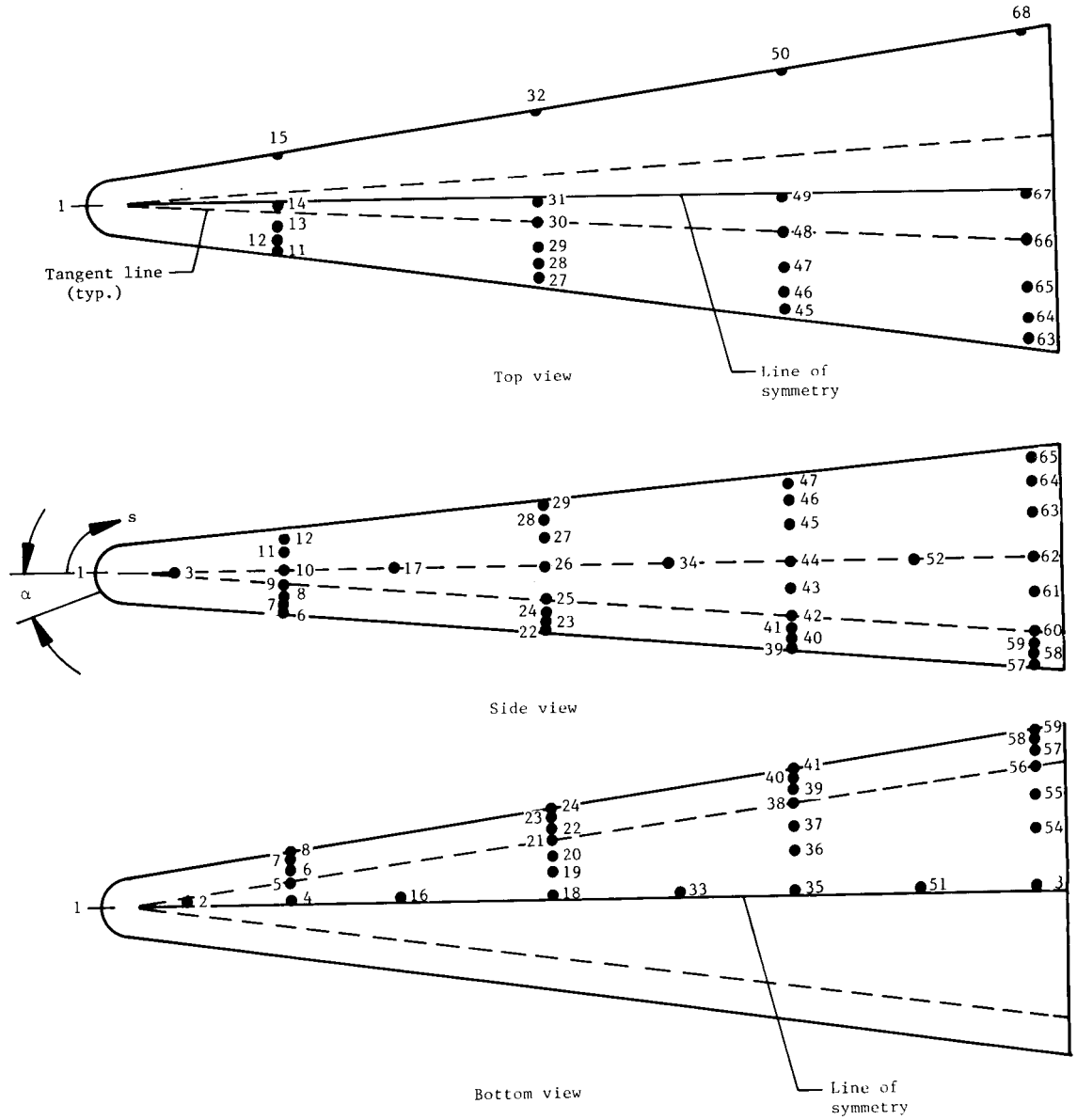

(b) Heat flux sensors.

Figure 9. Concluded.

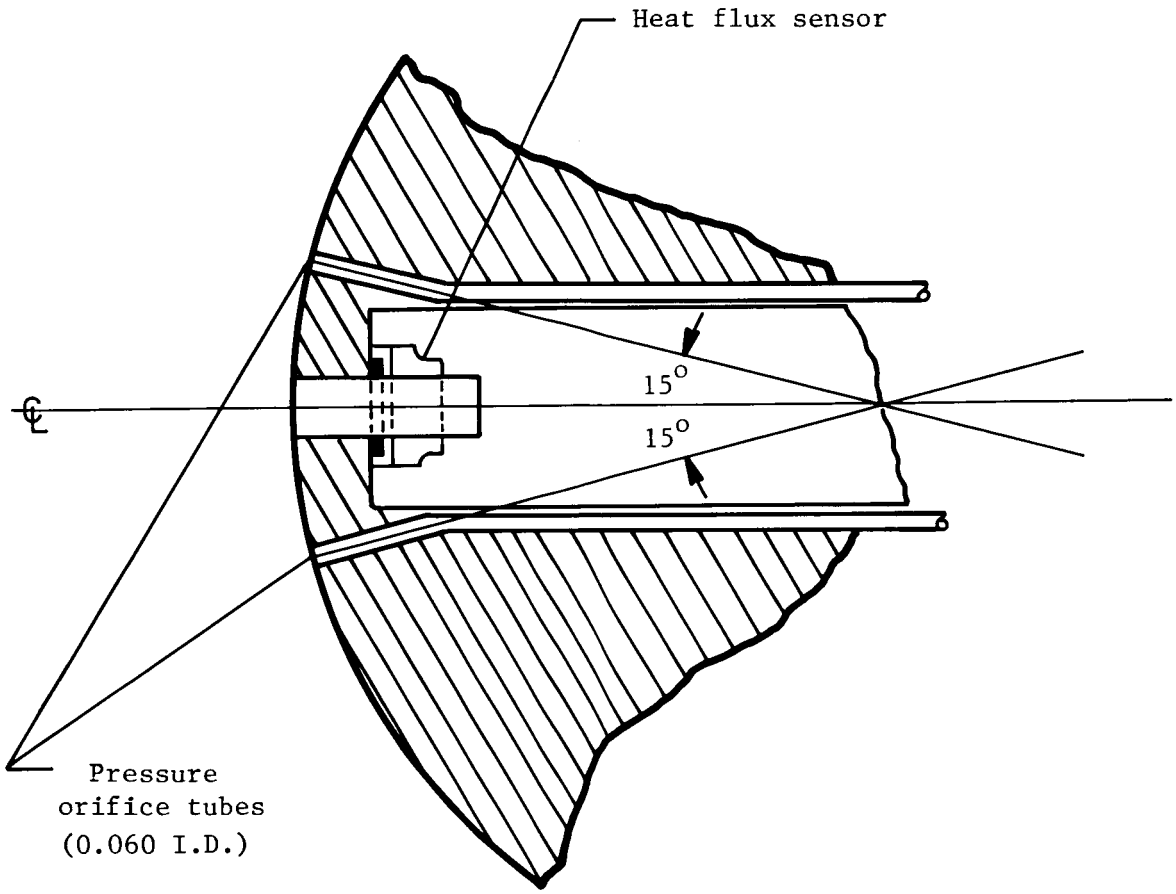

Figure 10. Heat flux sensor and pressure orifice locations on the nose of the model. Dimensions are in inches unless otherwise noted.

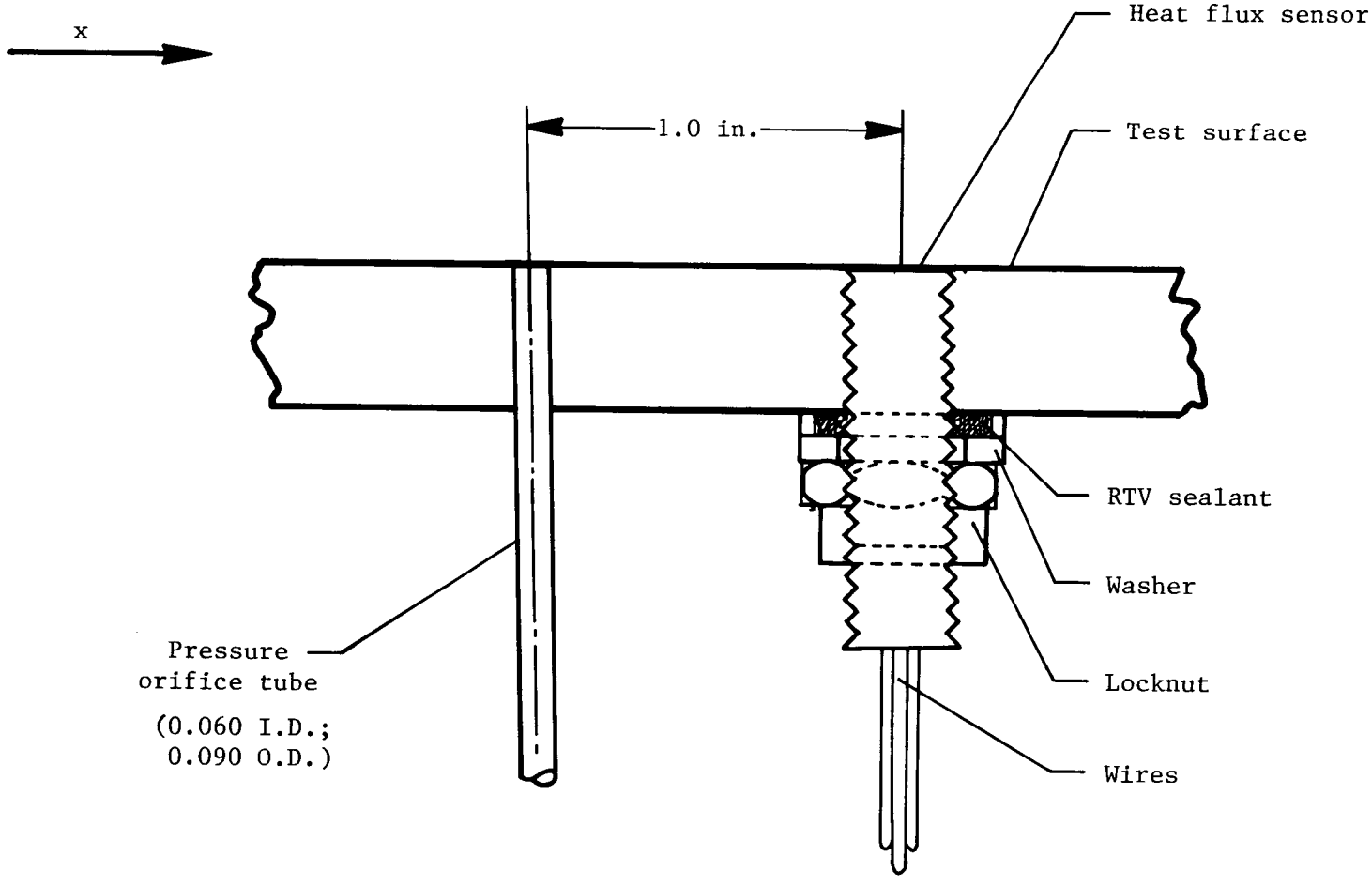

Figure 11. Typical surface instrumentation arrangement. Dimensions are in inches.

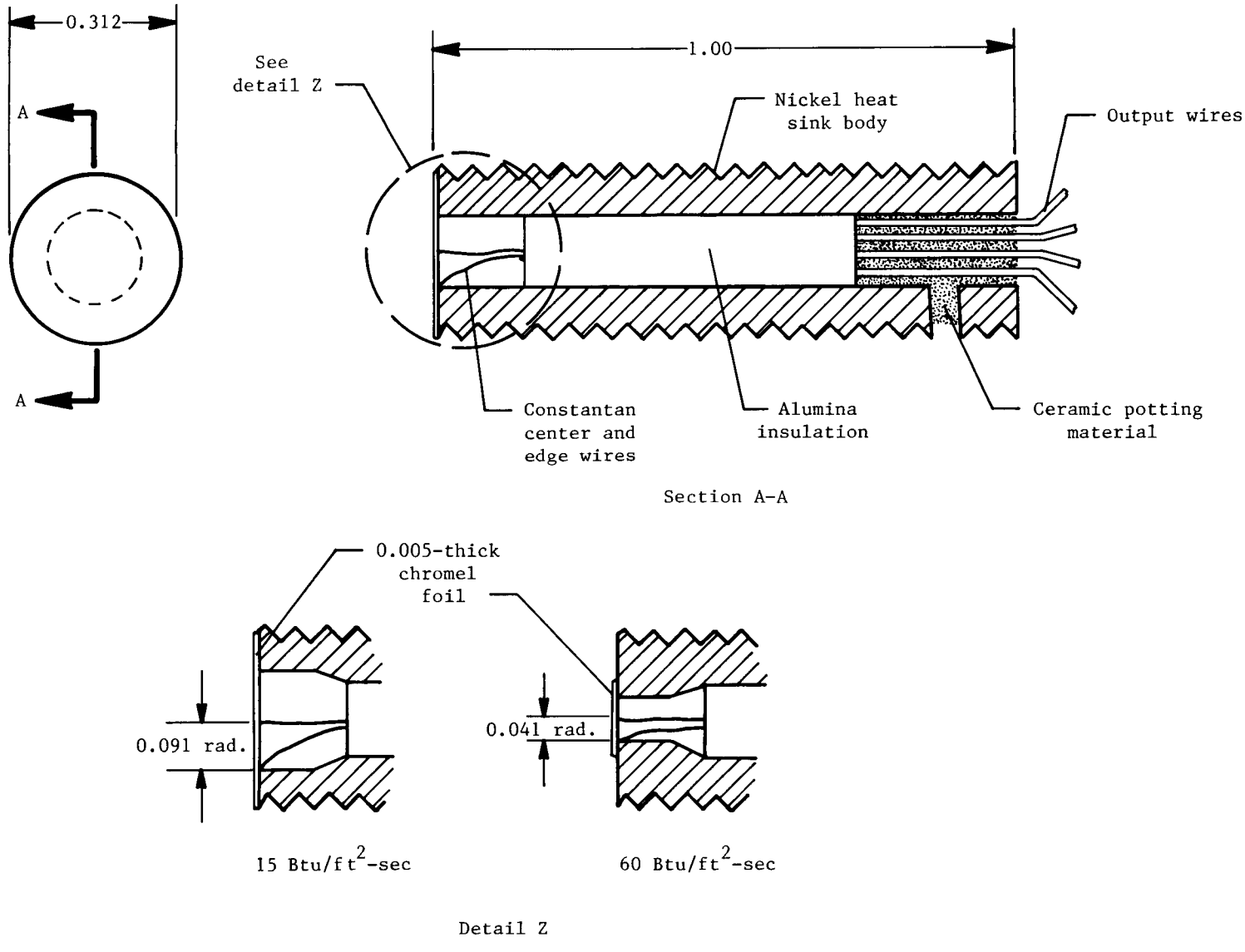

Figure 12. Schematic of Gardon-type heat flux sensor. Dimensions are in inches unless otherwise indicated.

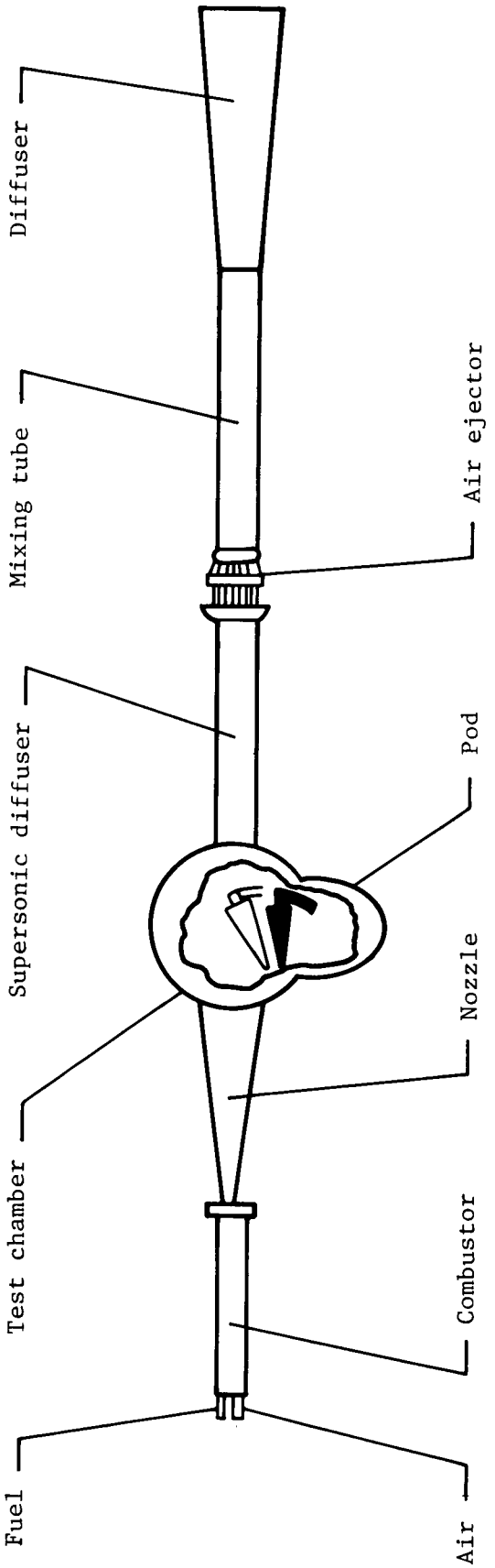

Figure 13. Schematic of Langley 8-Foot High-Temperature Tunnel.

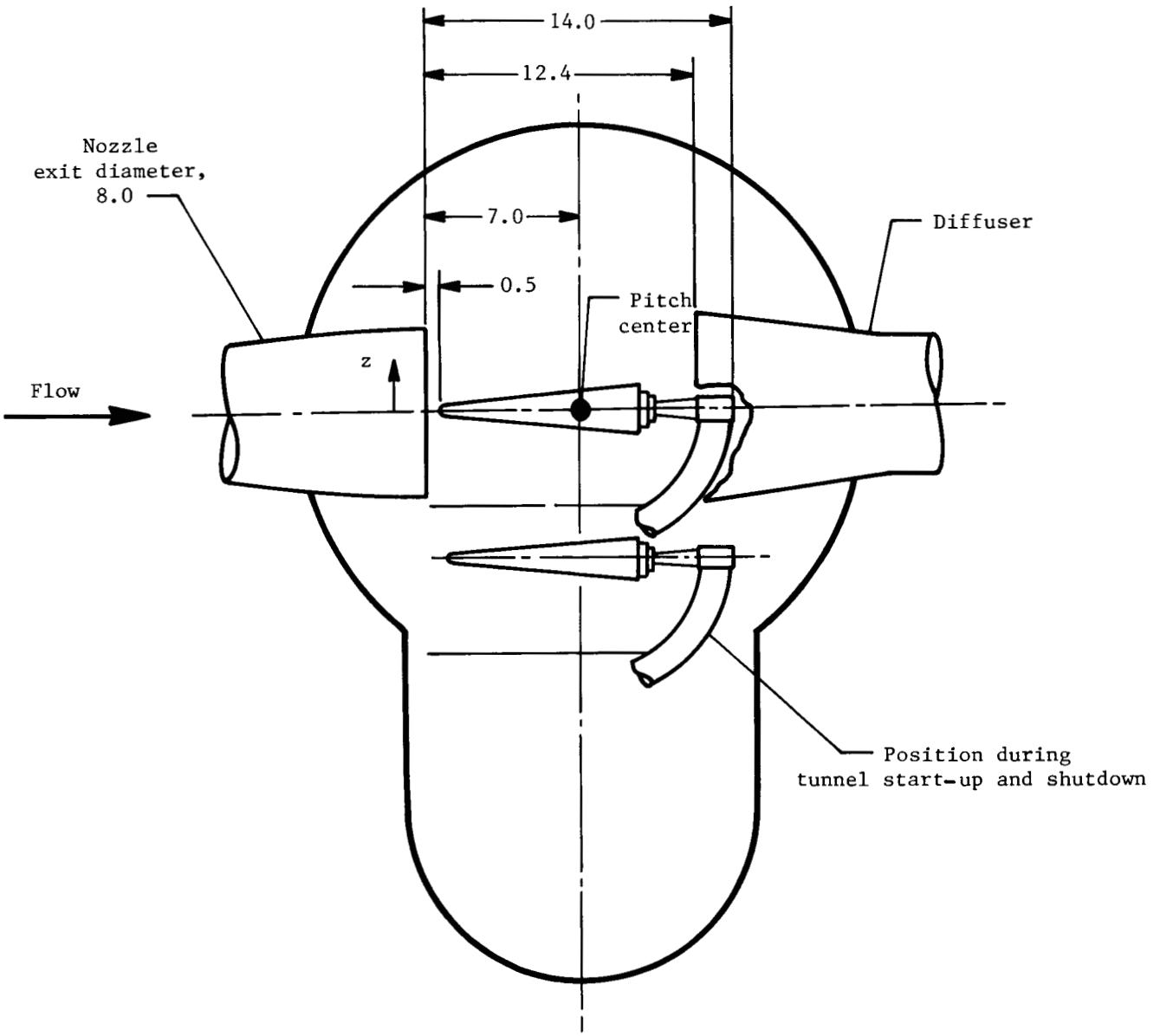

Figure 14. Cross-sectional view of test section of Langley 8-Foot High-Temperature Tunnel. Dimensions are in feet.

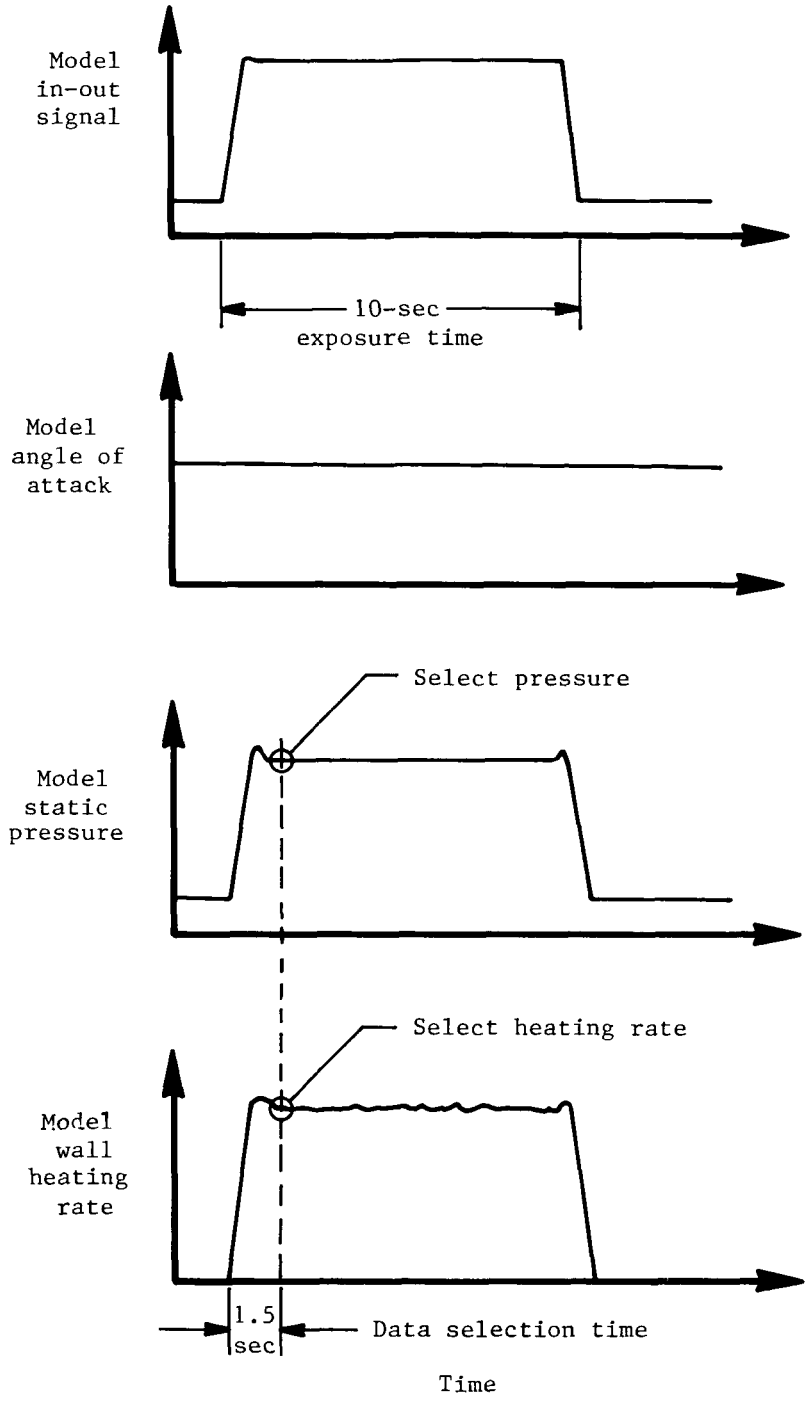

(a) Single angle of attack exposure.

Figure 15. Nominal test time histories.

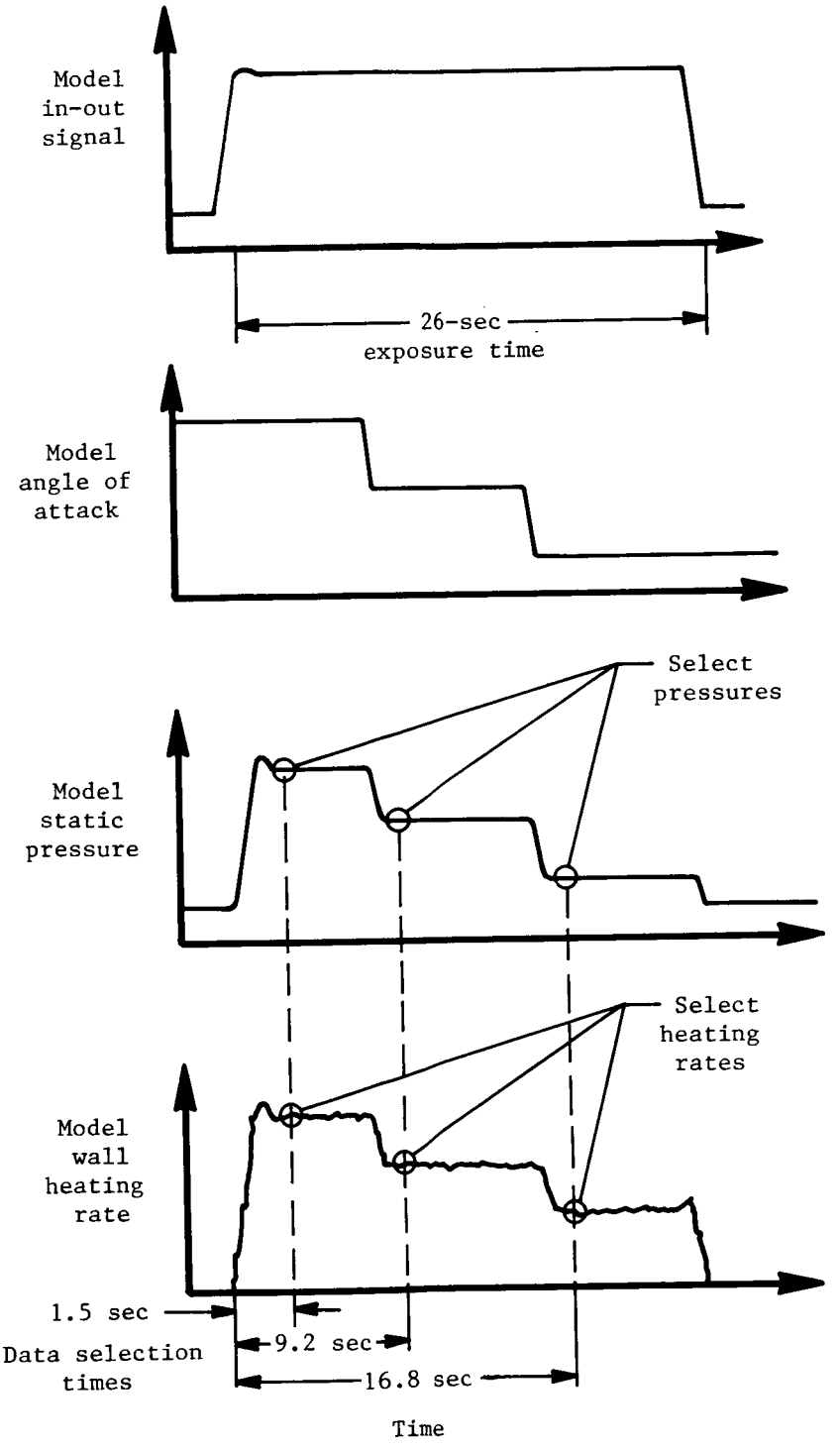

(b) Multiple angle of attack exposure.

Figure 15. Concluded.

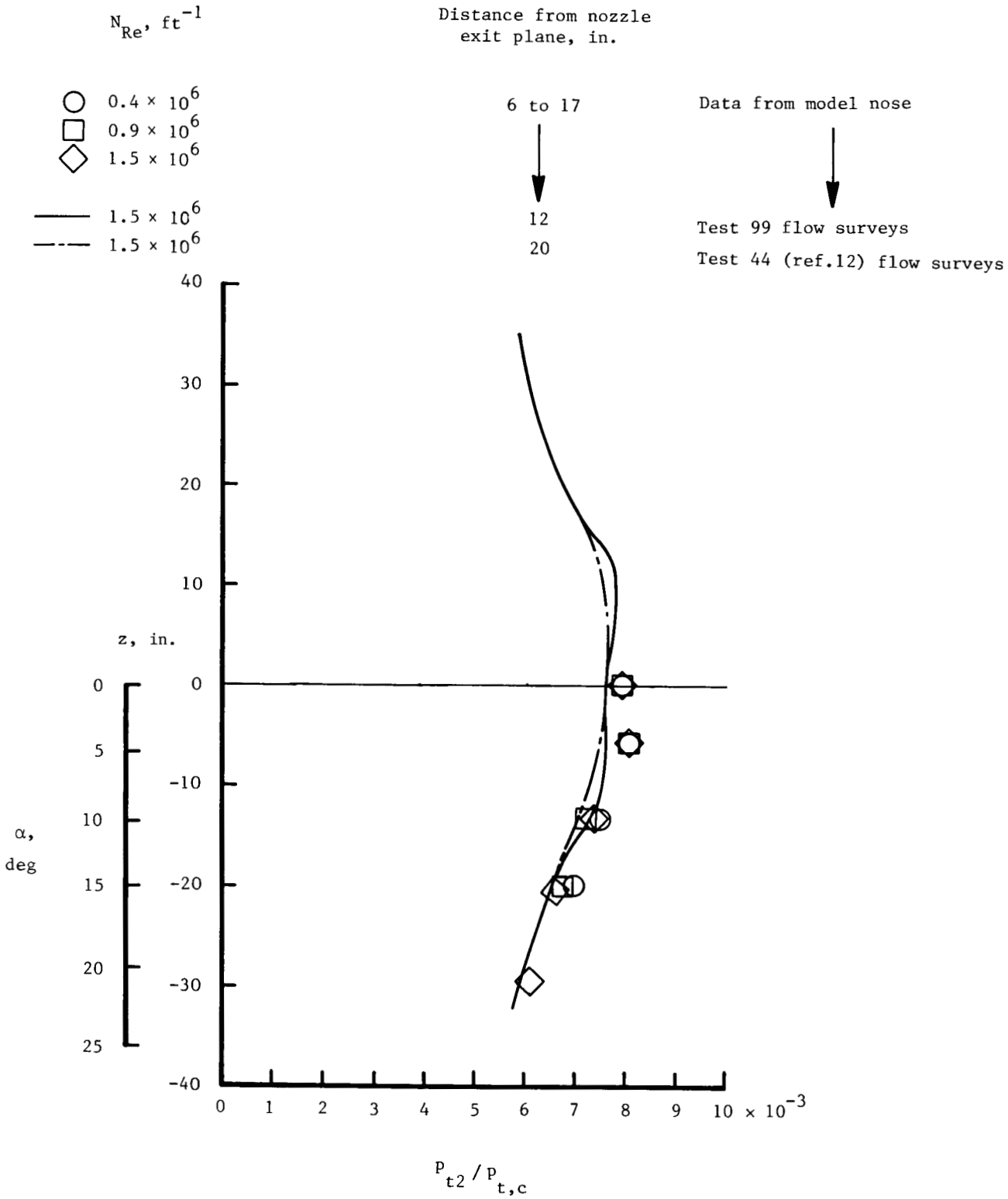

Figure 16. Pitot pressure distribution across test stream normalized to combustor pressure. $T_t = 3300°R$.

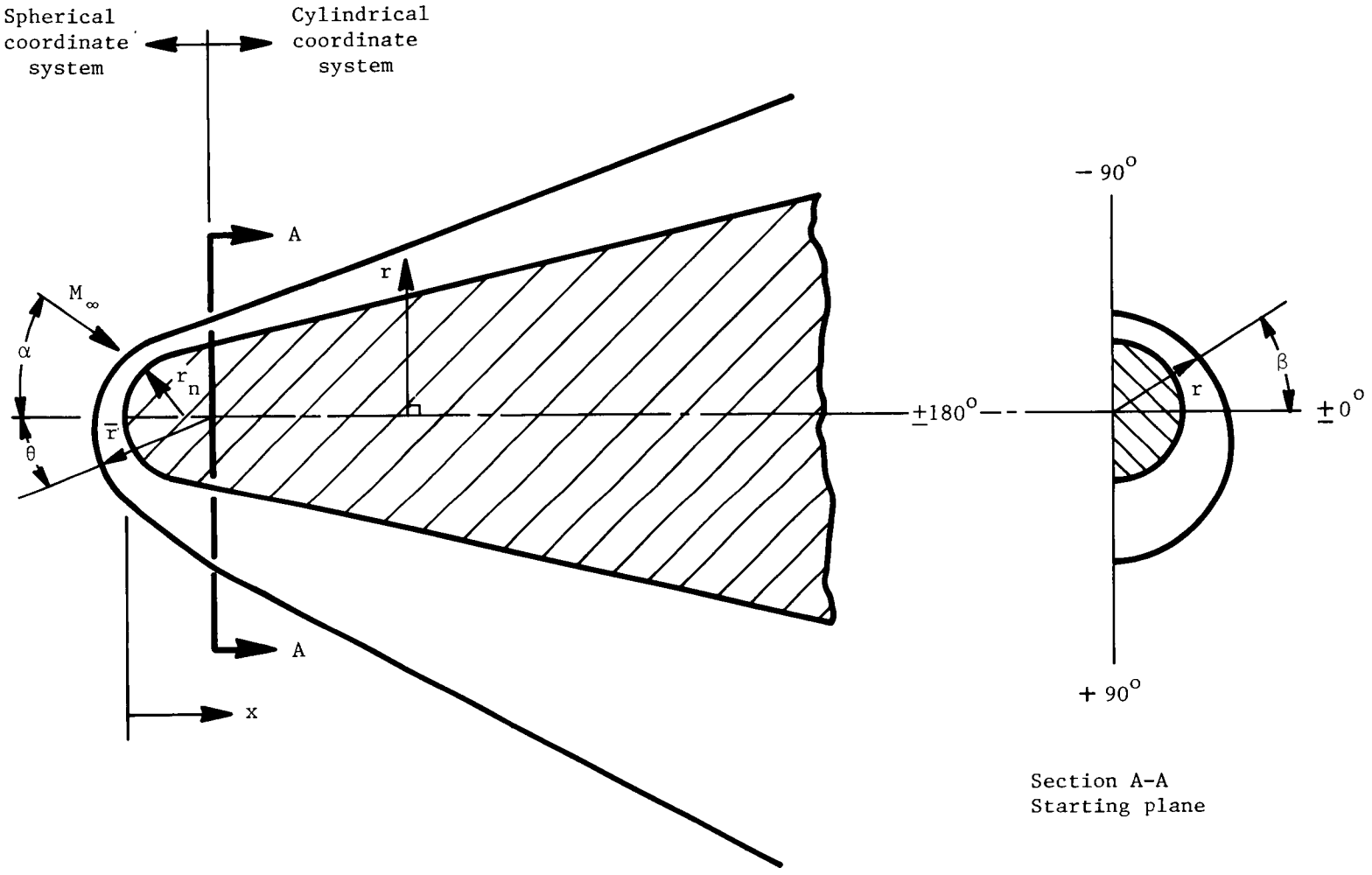

Figure 17. Coordinate system for computational grid.

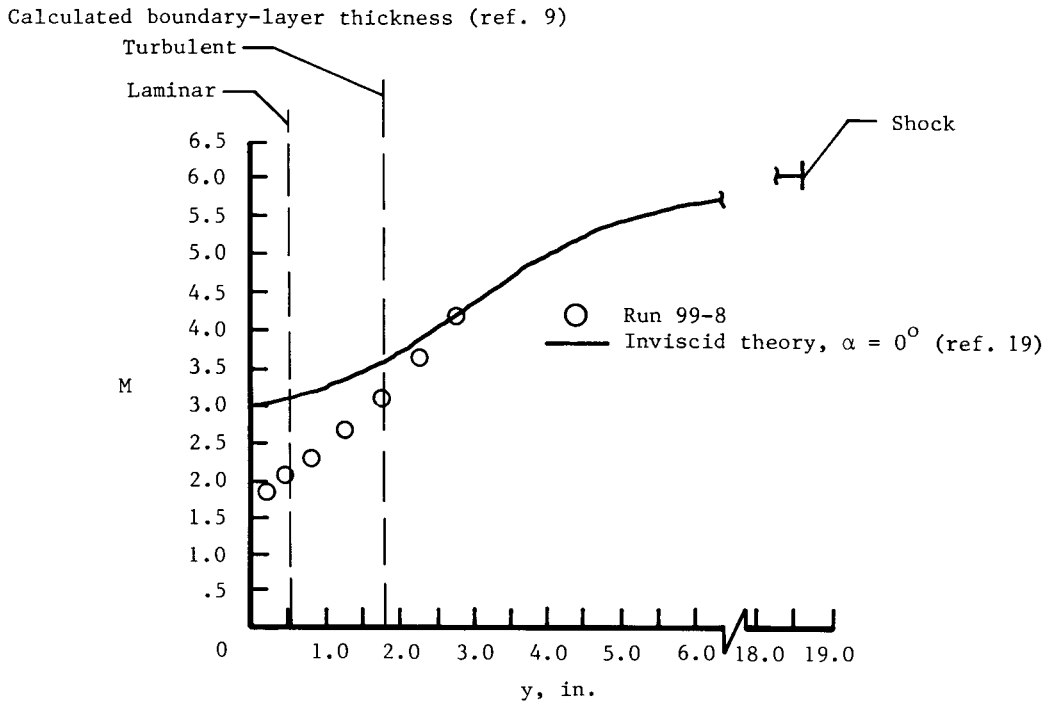

(a) $\alpha = 0°$; $\beta \approx -90°$.

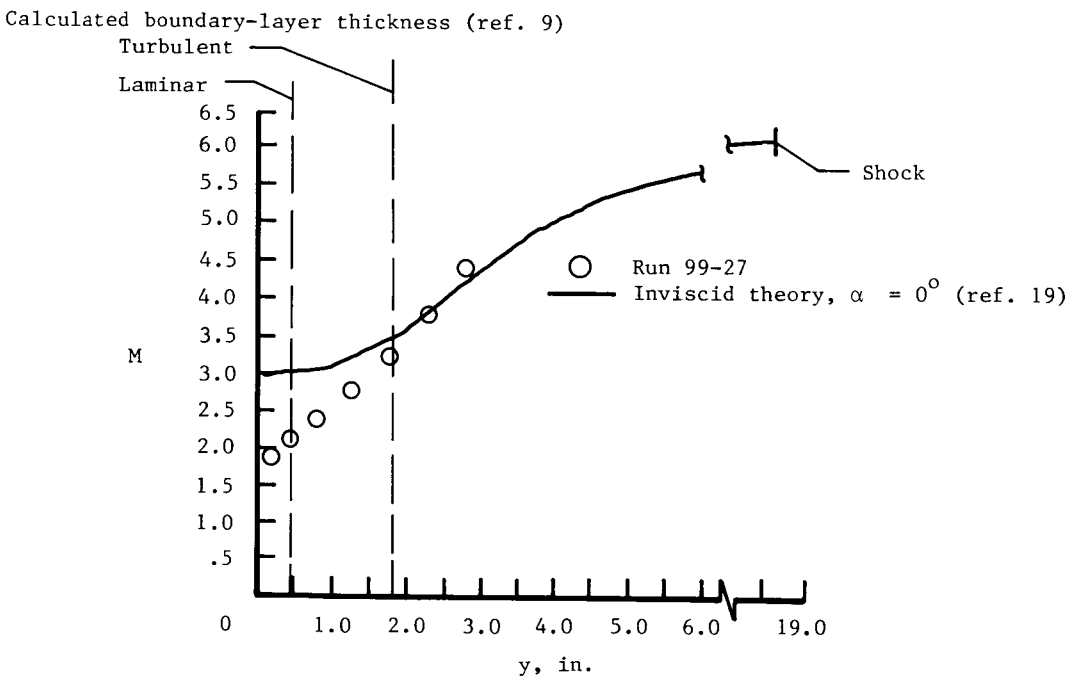

(b) $\alpha = -0.1°$; $\beta \approx 90°$.

Figure 18. Mach number distributions as function of distance normal to model test surface at $x/r_n = 34.54$ with 0.094-in-diameter boundary-layer trips. $N_{Re} = 1.5 \times 10^6$ ft^{-1}.

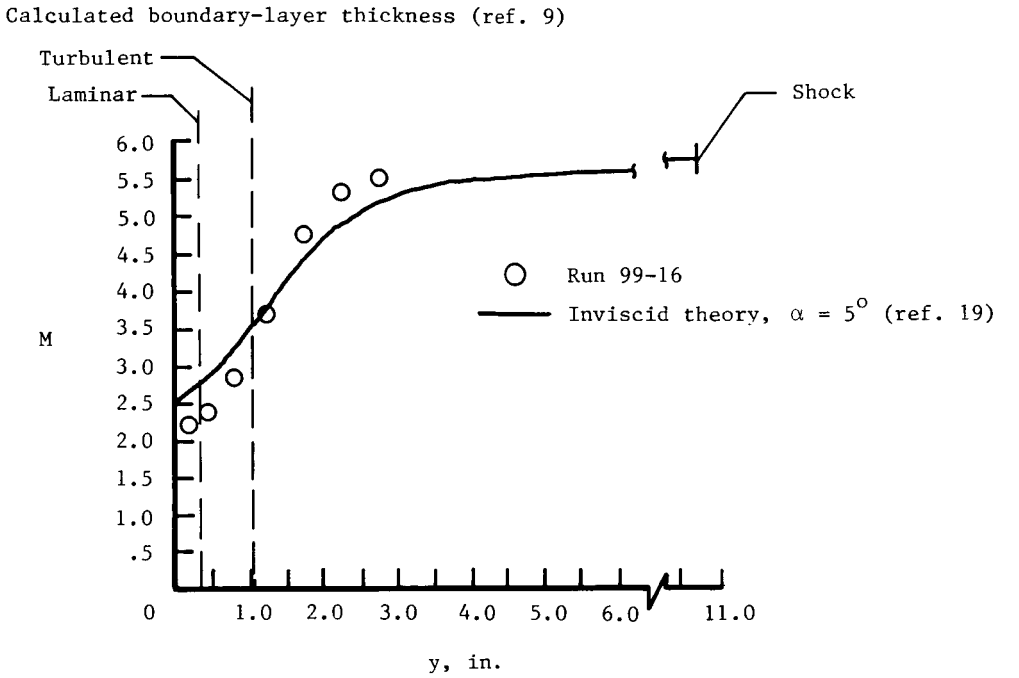

(c) $\alpha = 4.8°; \beta \approx -90°$.

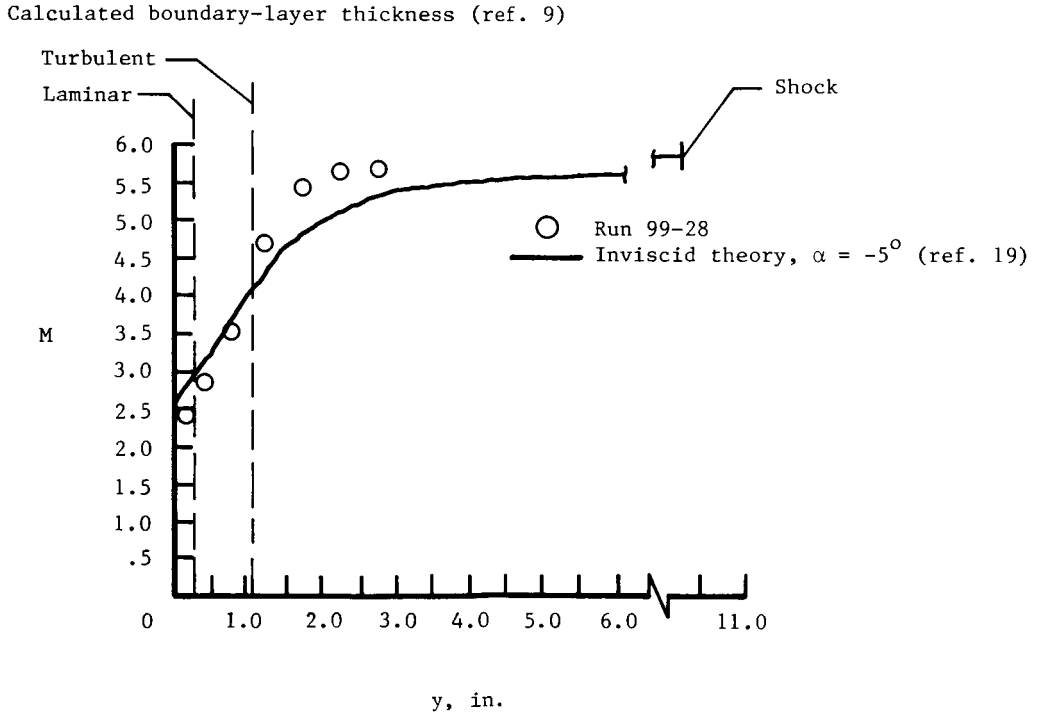

(d) $\alpha = -4.8°; \beta \approx 90°$.

Figure 18. Continued.

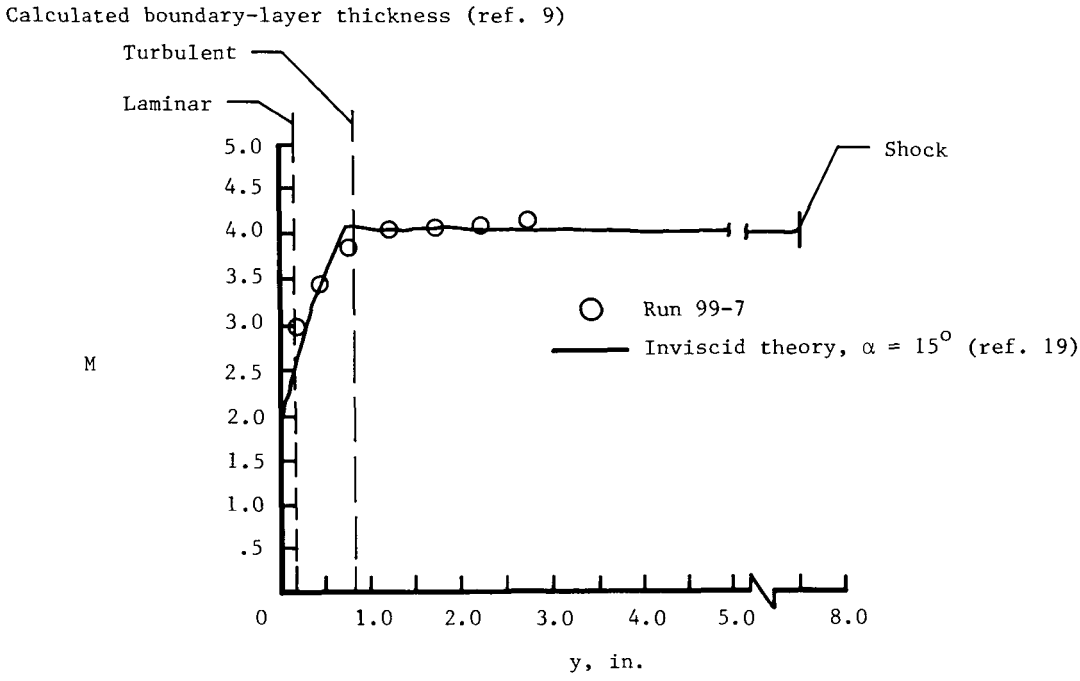

(e) $\alpha = 15.0°$; $\beta \approx -90°$.

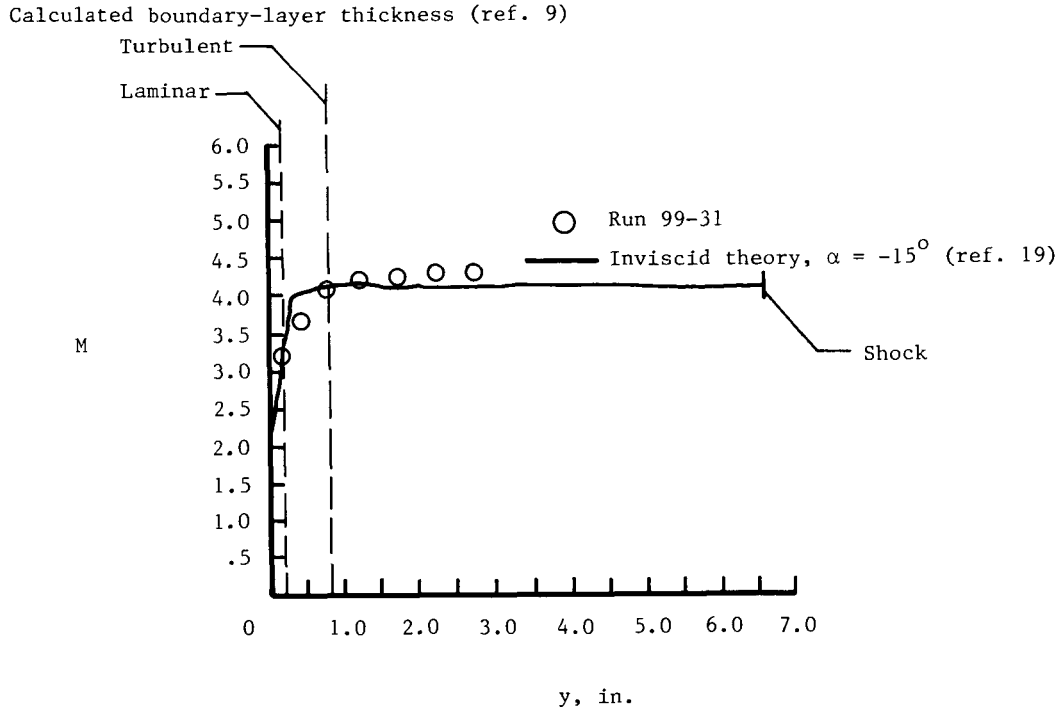

(f) $\alpha = -14.8°$; $\beta \approx 90°$.

Figure 18. Concluded.

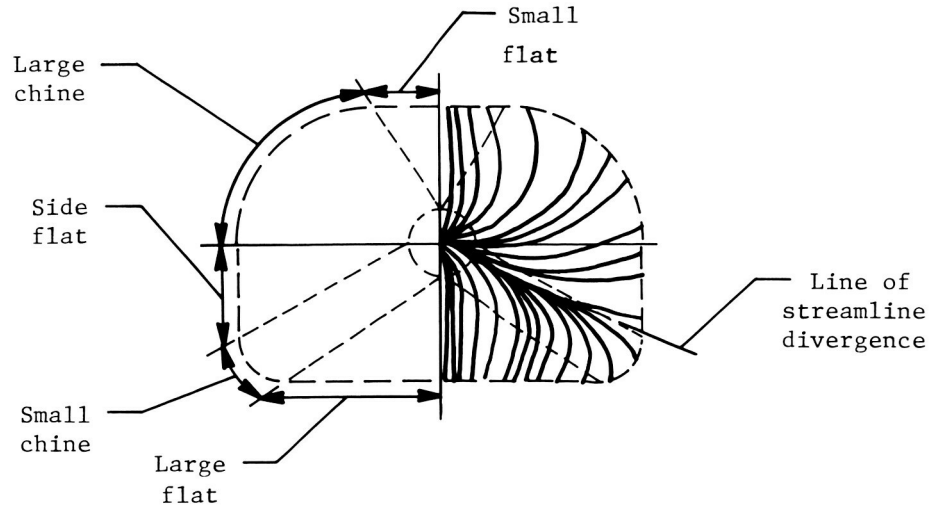

(a) $\alpha = 0°$.

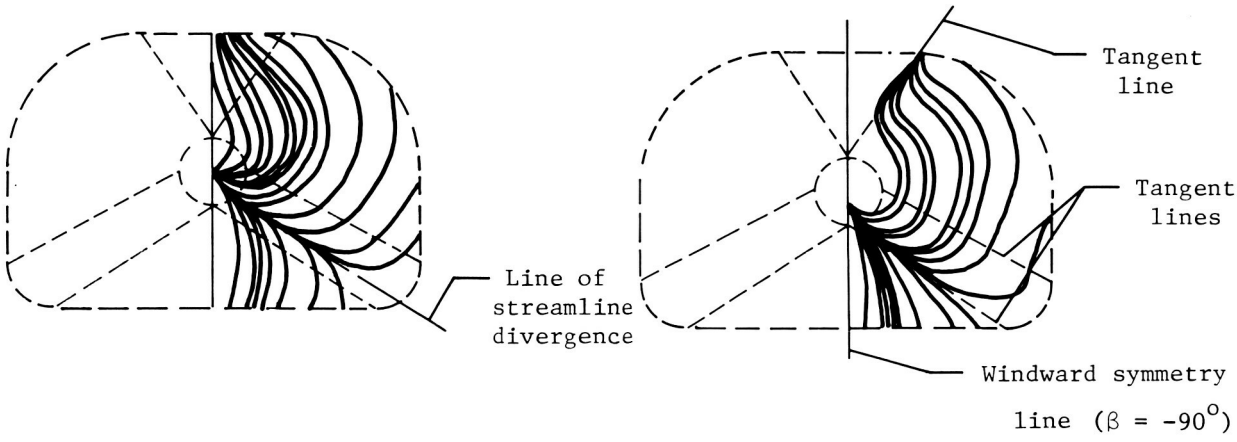

(b) $\alpha = 5°$.

(c) $\alpha = 15°$.

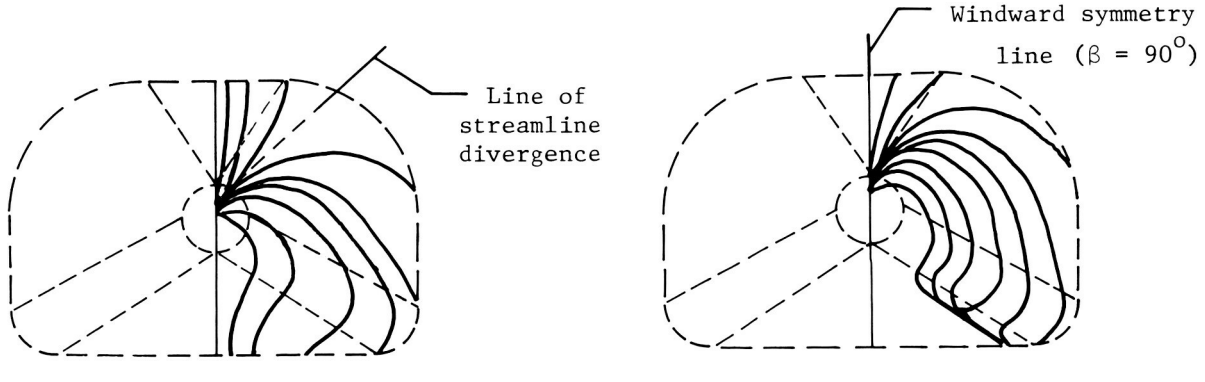

(d) $\alpha = -5°$.

(e) $\alpha = -15°$.

Figure 19. Front view of model showing predicted (ref. 20) inviscid surface streamlines.

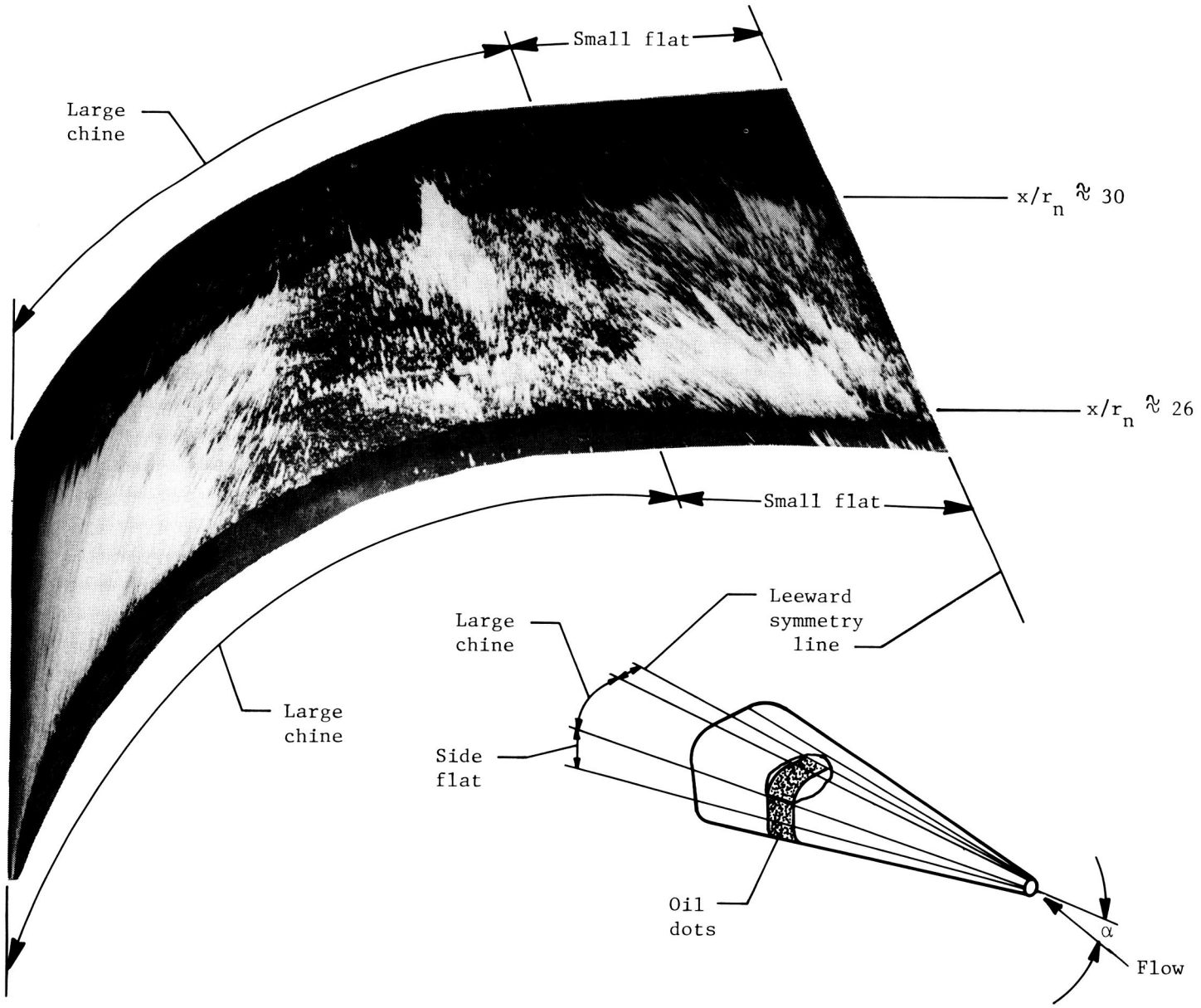

Figure 20. Oil flow photograph showing leeward-side separation on model at $\alpha = 15.0°$ (run 99-7) from $x/r_n = 26$ to 30. $N_{\mathrm{Re}} = 1.5 \times 10^6$ ft^{-1}; 0.094-in-diam trips.

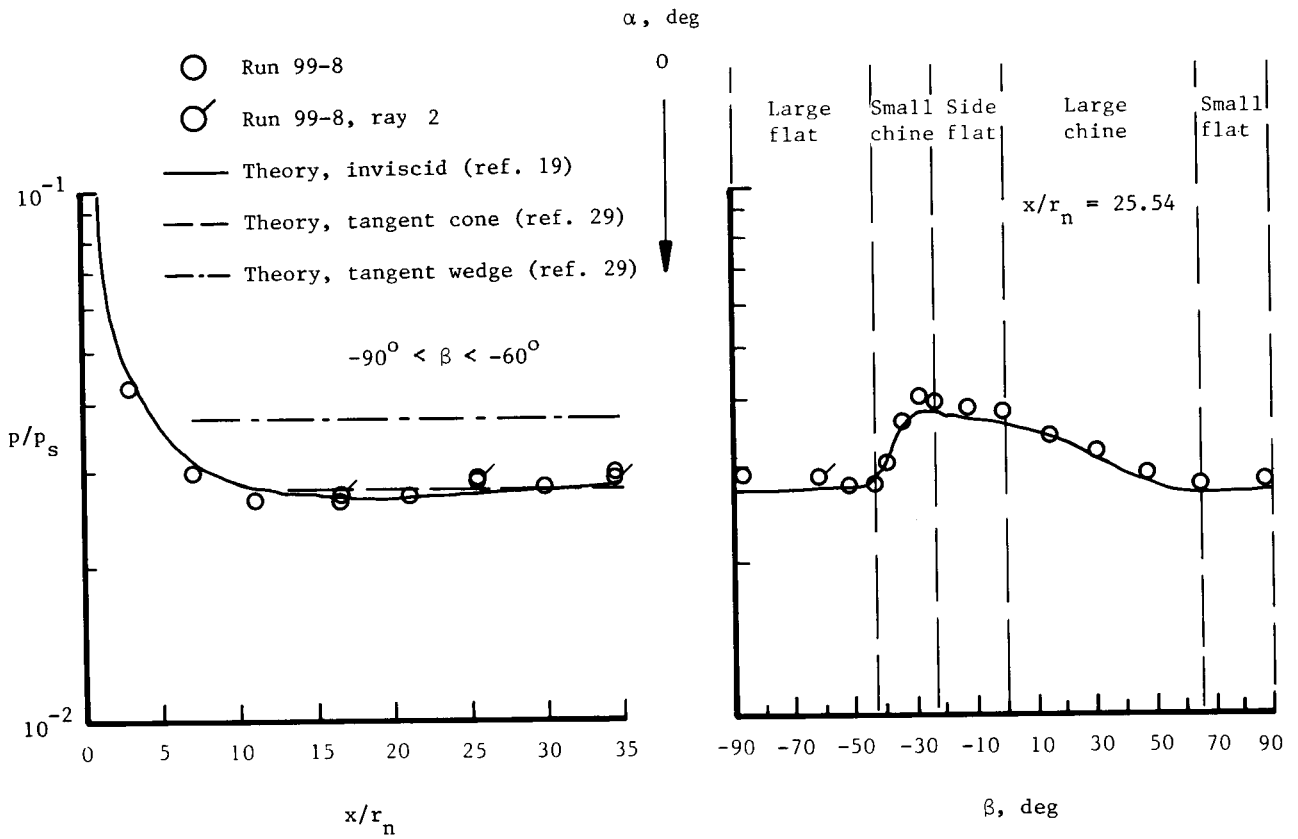

(a) $\alpha = 0°$.

Figure 21. Axial and circumferential surface pressure distributions at various angles of attack. $N_{Re} = 1.5 \times 10^6$ ft^{-1}; 0.094-in-diam trips.

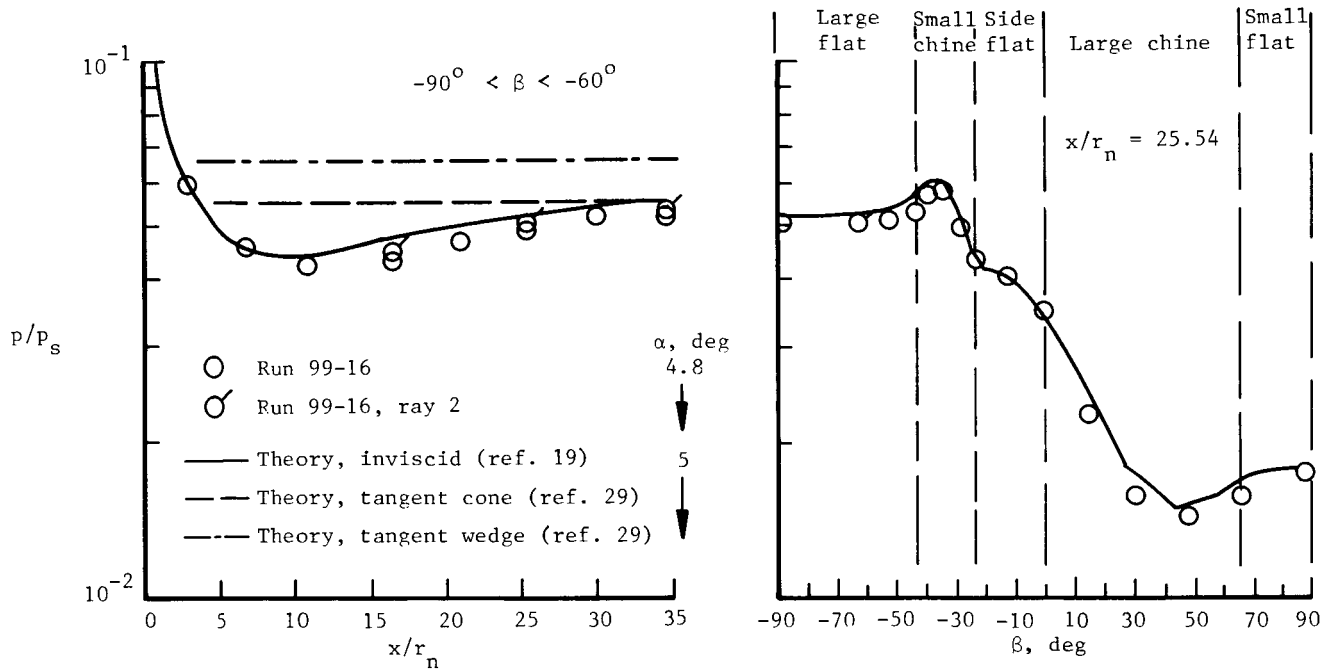

(b) $\alpha = 4.8°$.

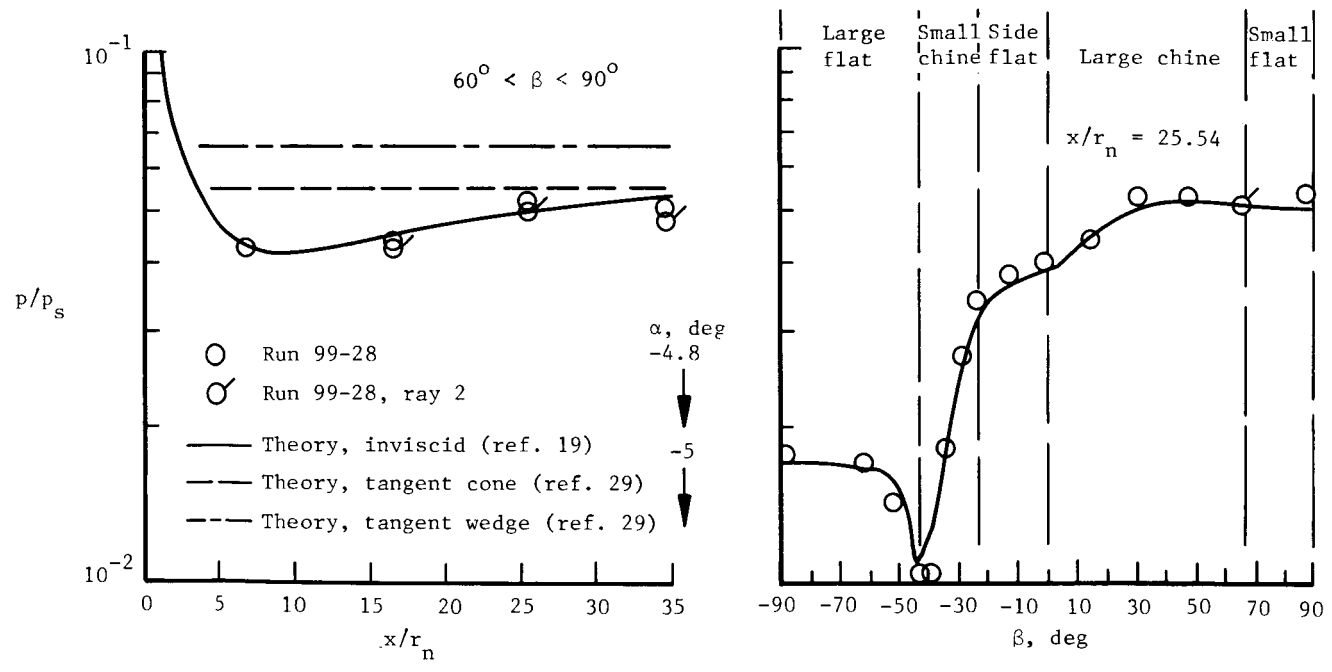

(c) $\alpha = -4.8°$.

Figure 21. Continued.

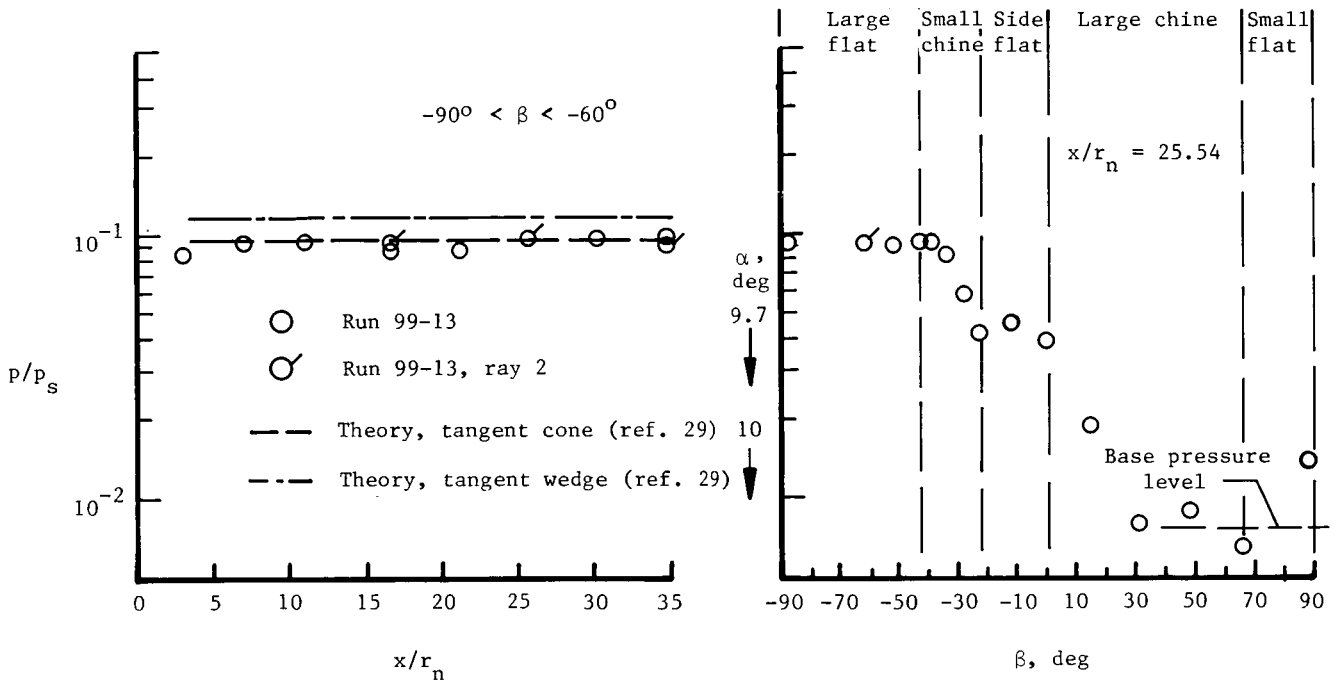

(d) $\alpha = 9.7°$.

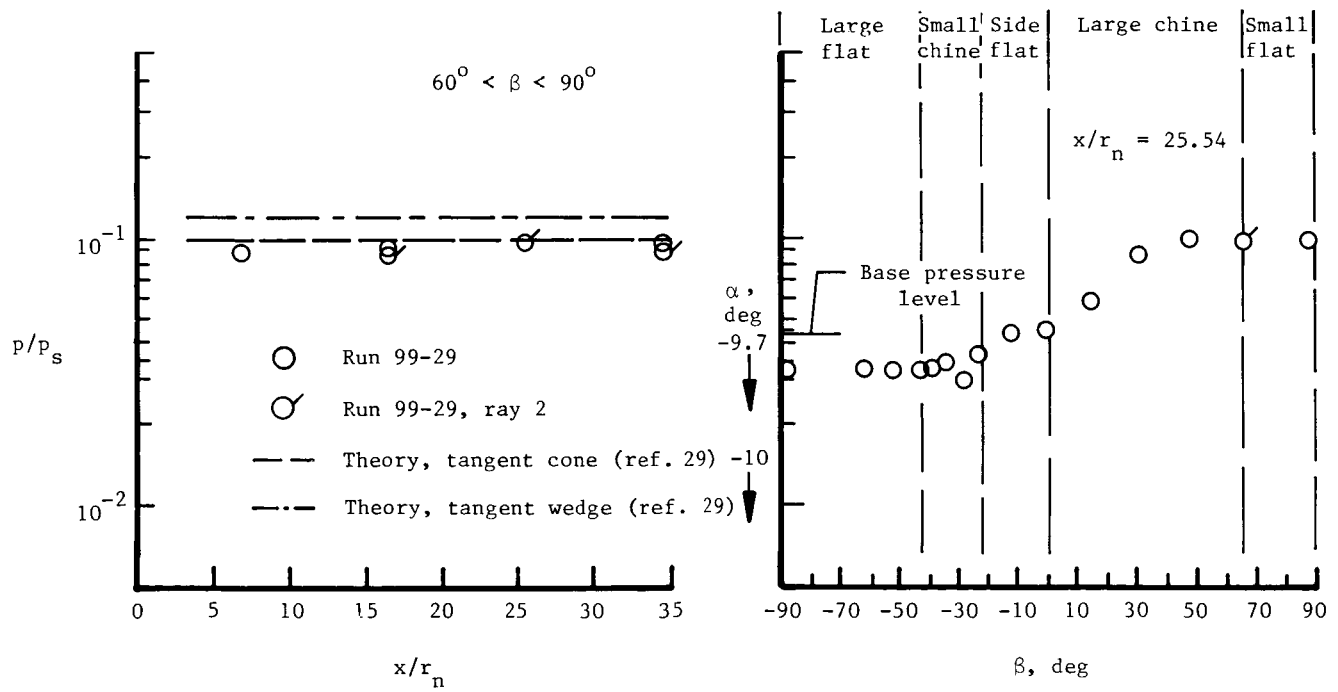

(e) $\alpha = -9.7°$.

Figure 21. Continued.

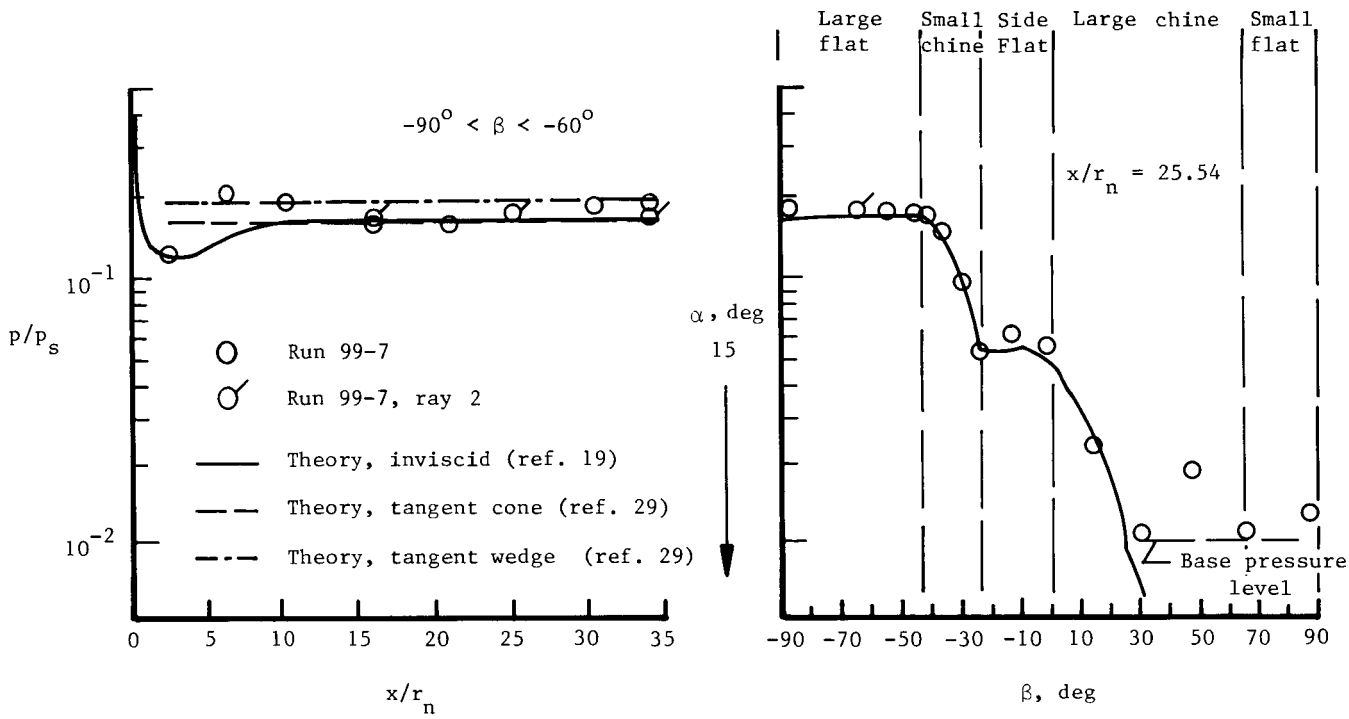

(f) $\alpha = 15.0°$.

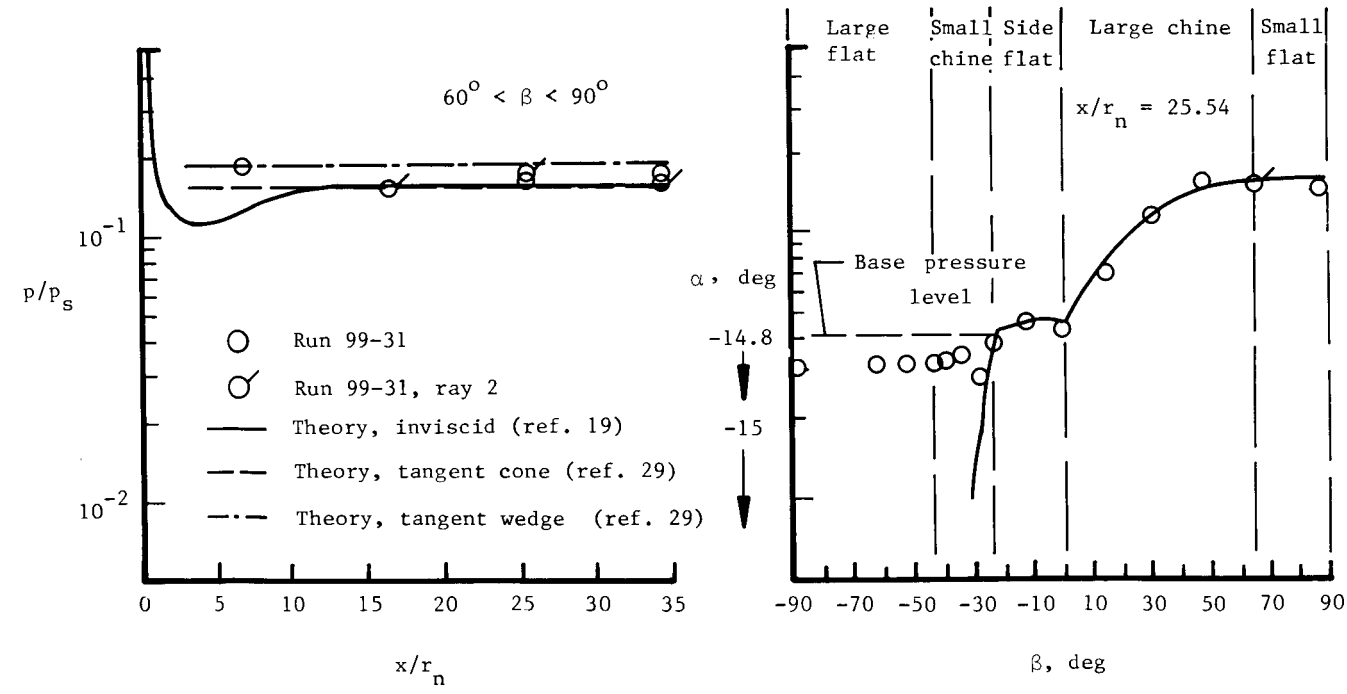

(g) $\alpha = -14.8°$.

Figure 21. Continued.

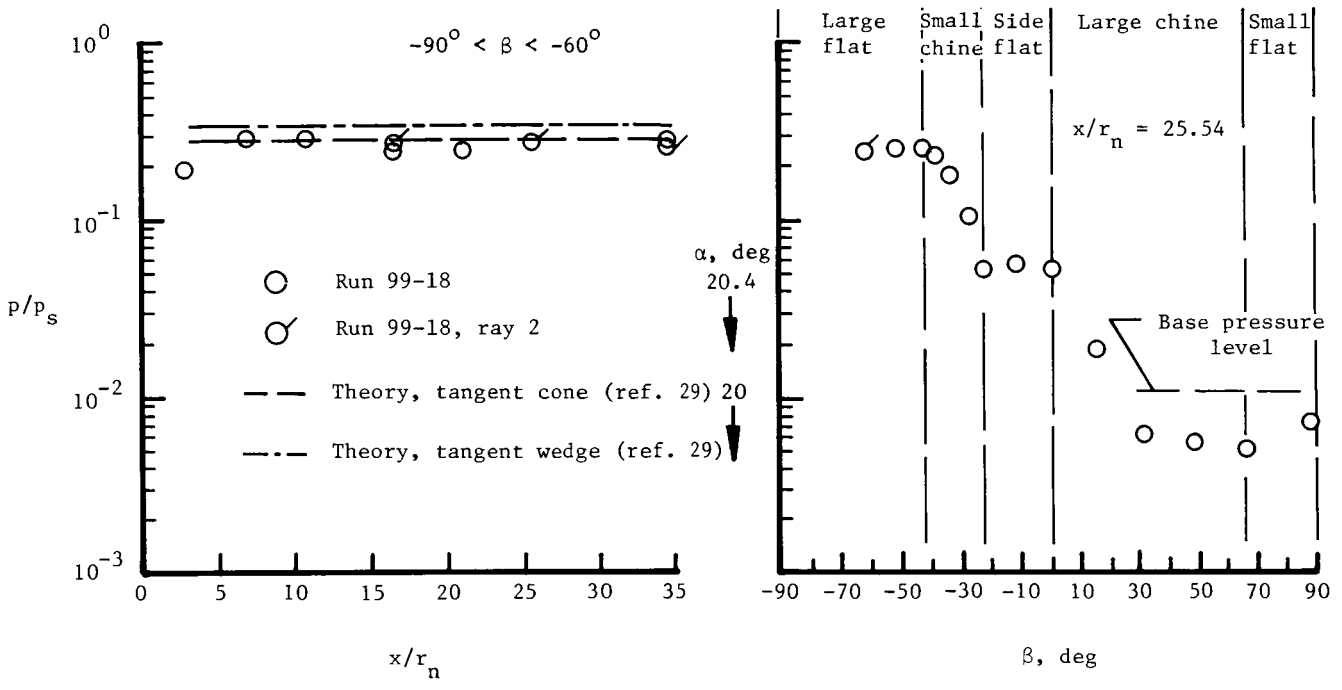

(h) $\alpha = 20.4°$.

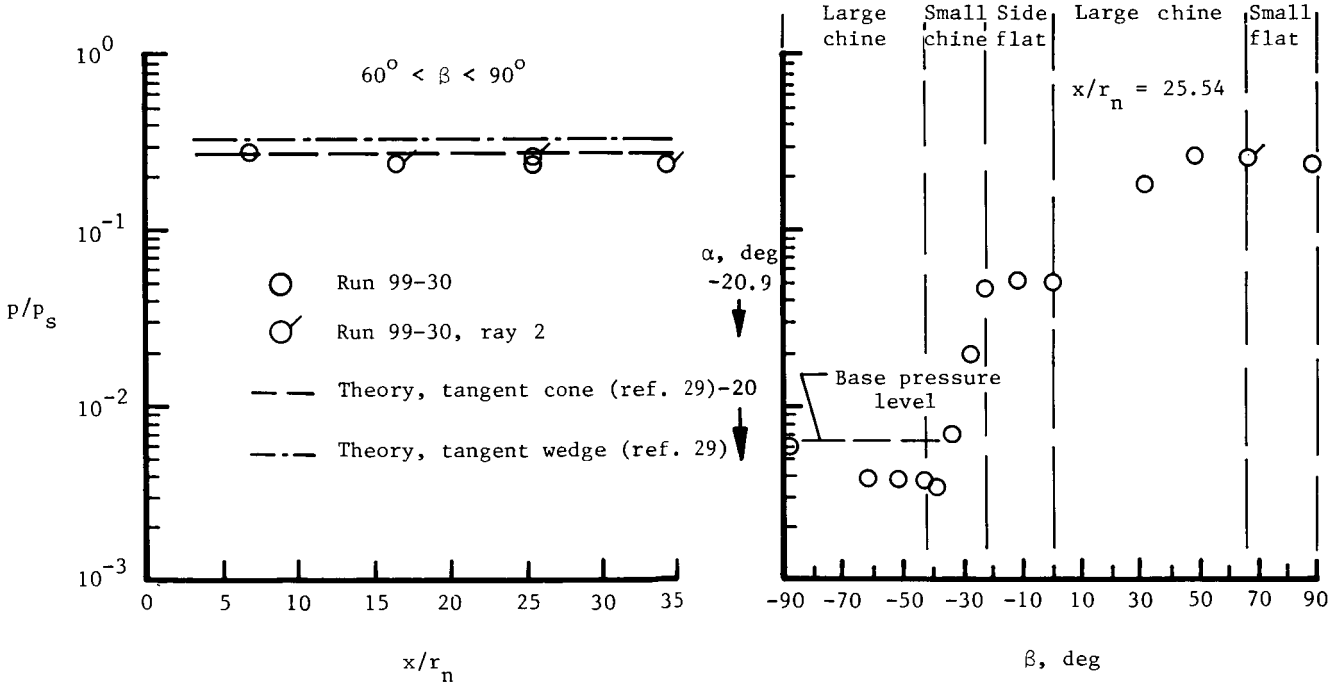

(i) $\alpha = -20.9°$.

Figure 21. Concluded.

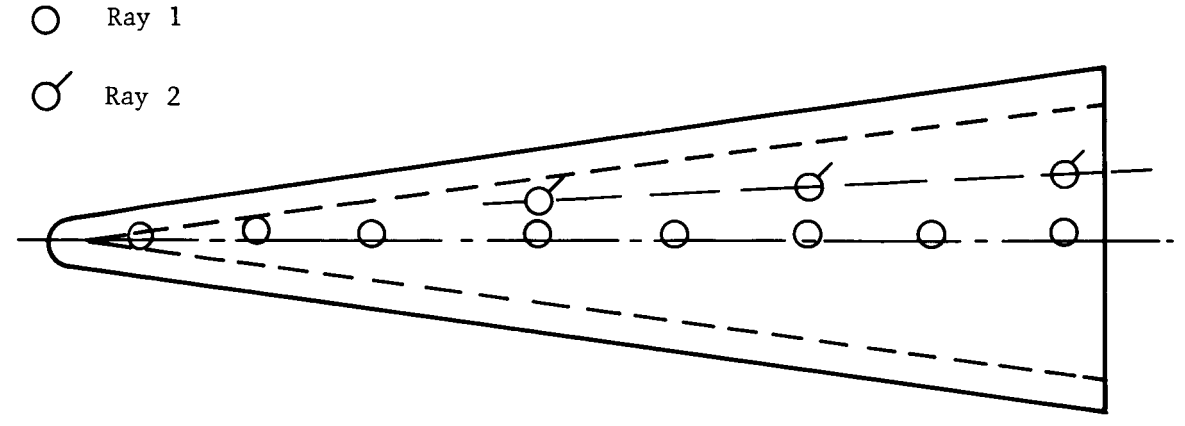

(a) $\alpha \geq 0°$.

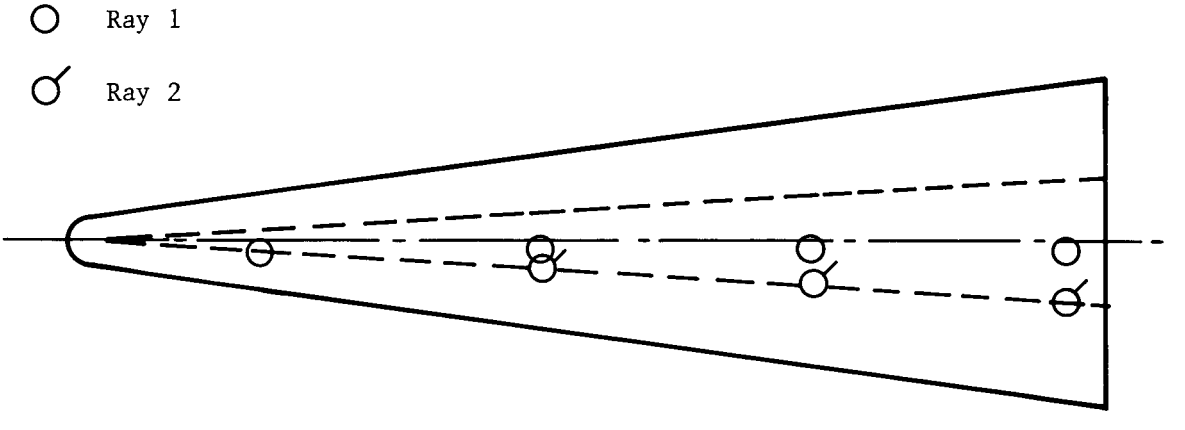

(b) $\alpha < 0°$.

Figure 22. Pressure orifice and heat gage locations corresponding to axial distributions of pressures and heating rates.

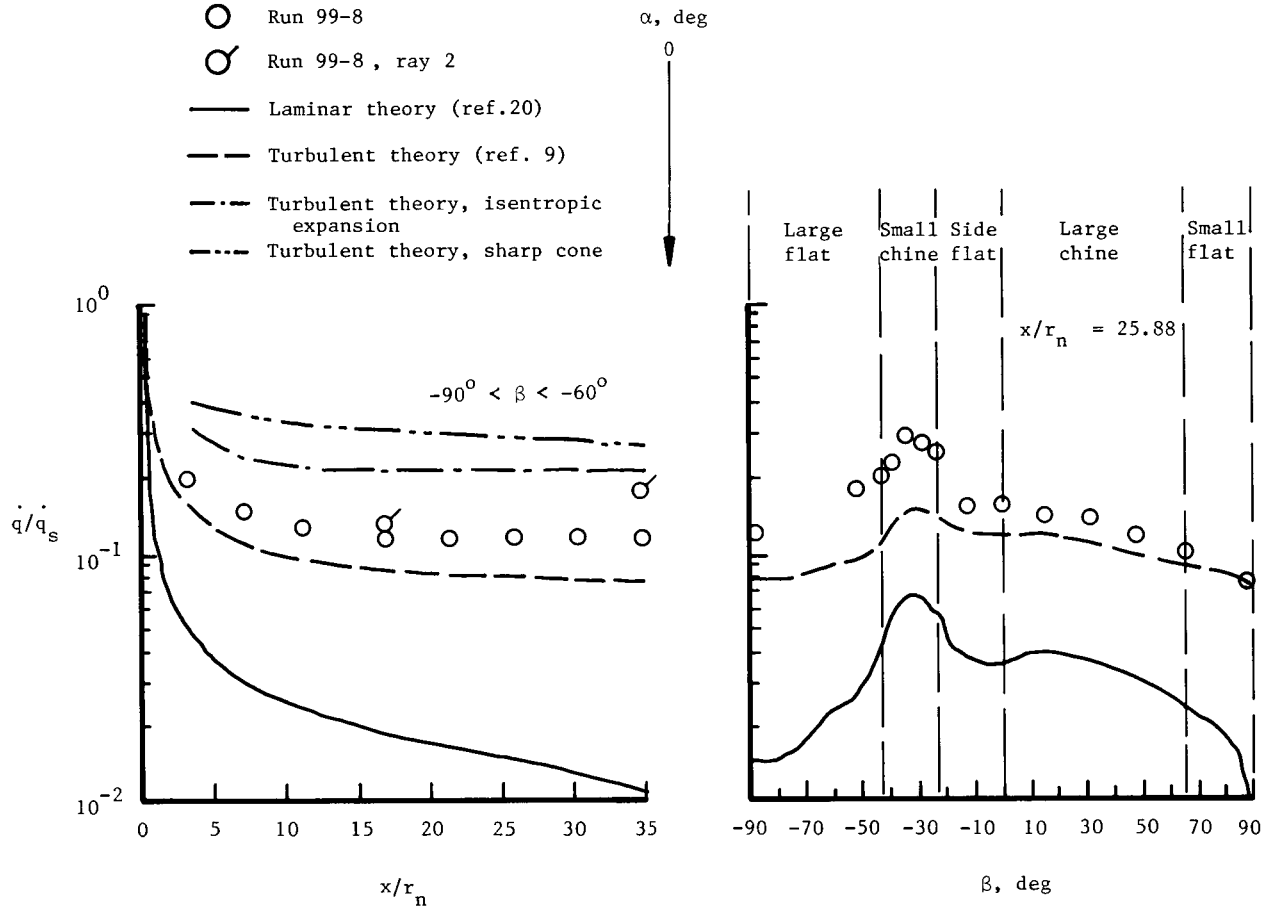

(a) $\alpha = 0°$.

Figure 23. Axial and circumferential heating-rate distributions at various angles of attack, $N_{Re} = 1.5 \times 10^6$ ft^{-1}; 0.094-in-diam trips.

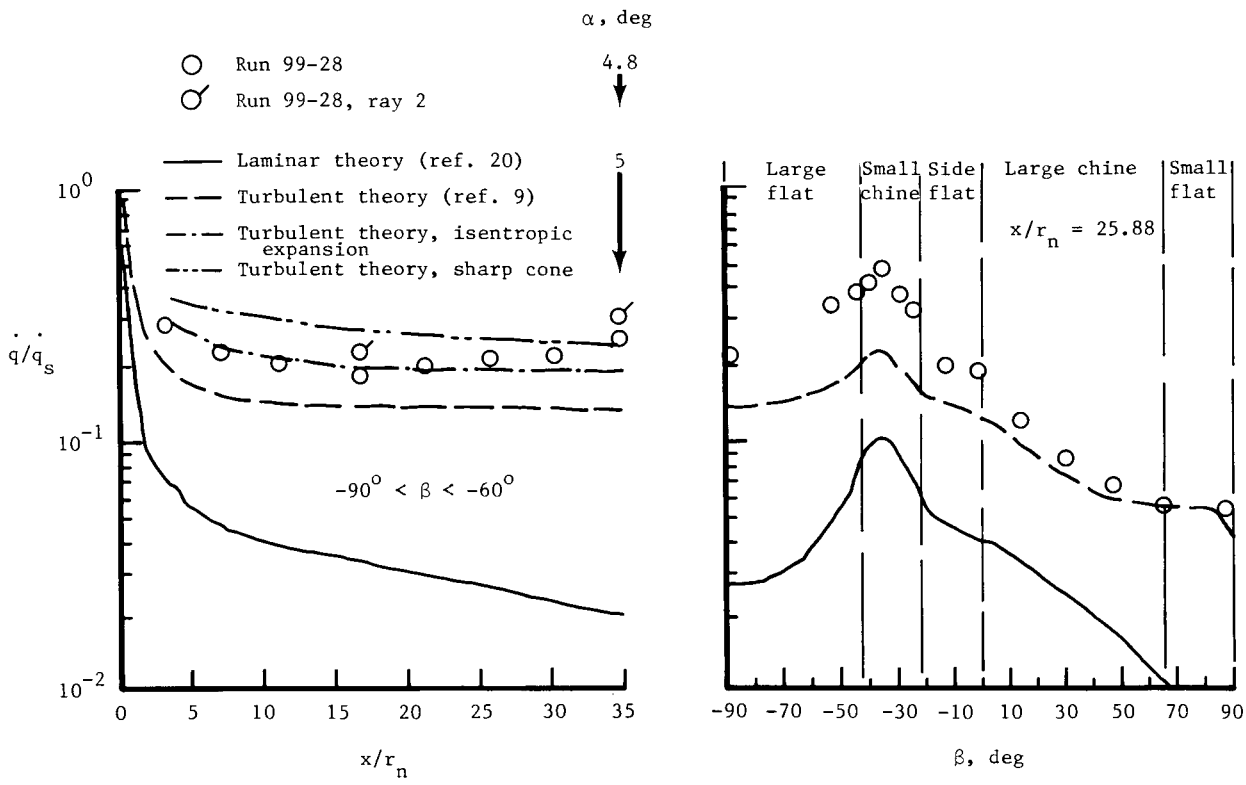

(b) $\alpha = 4.8°$.

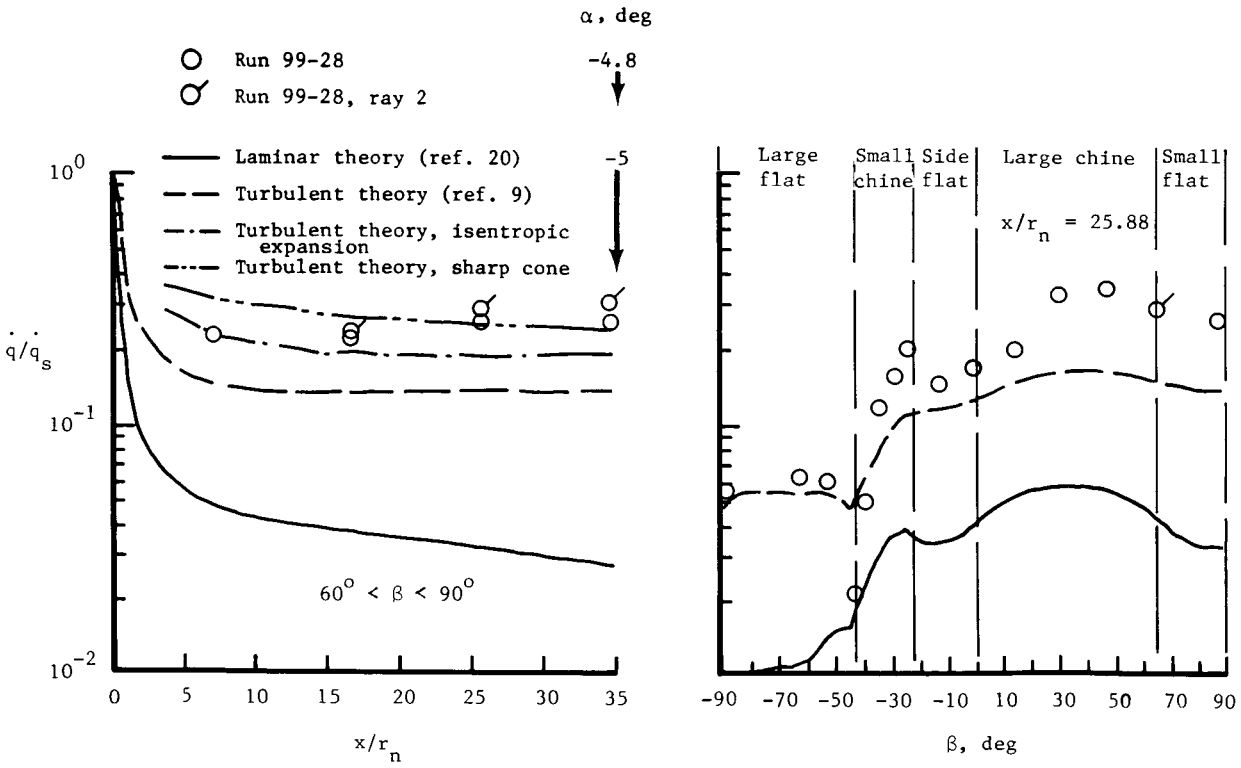

(c) $\alpha = -4.8°$.

Figure 23. Continued.

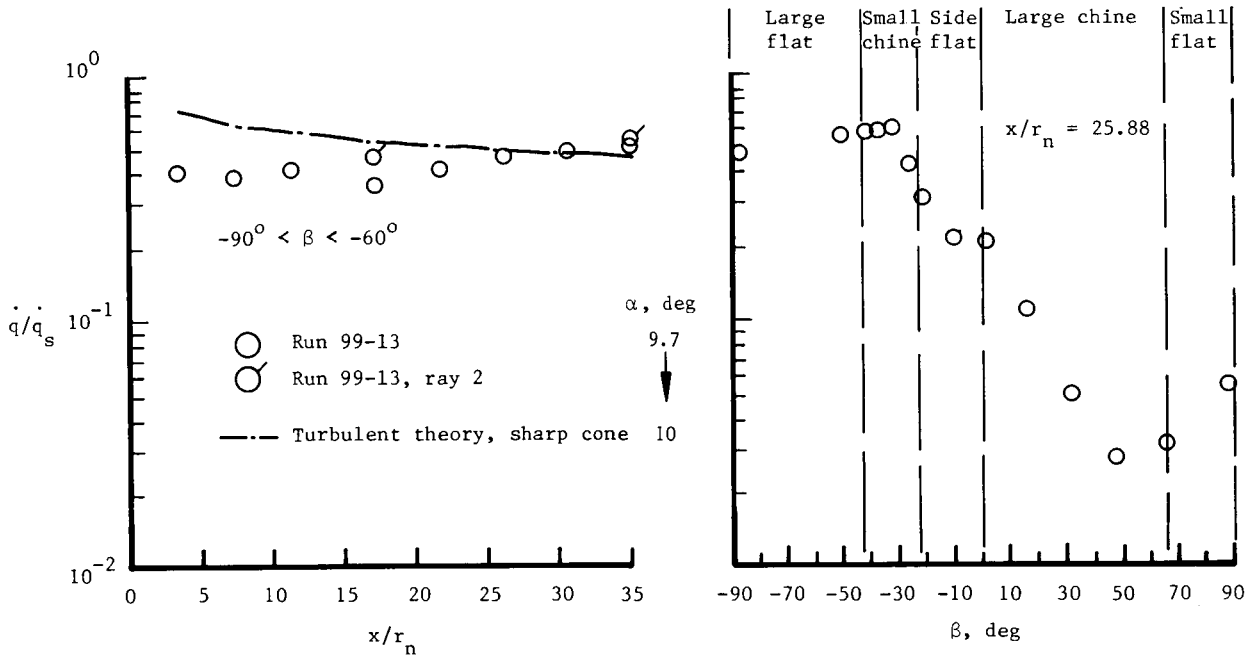

(d) $\alpha = 9.7°$.

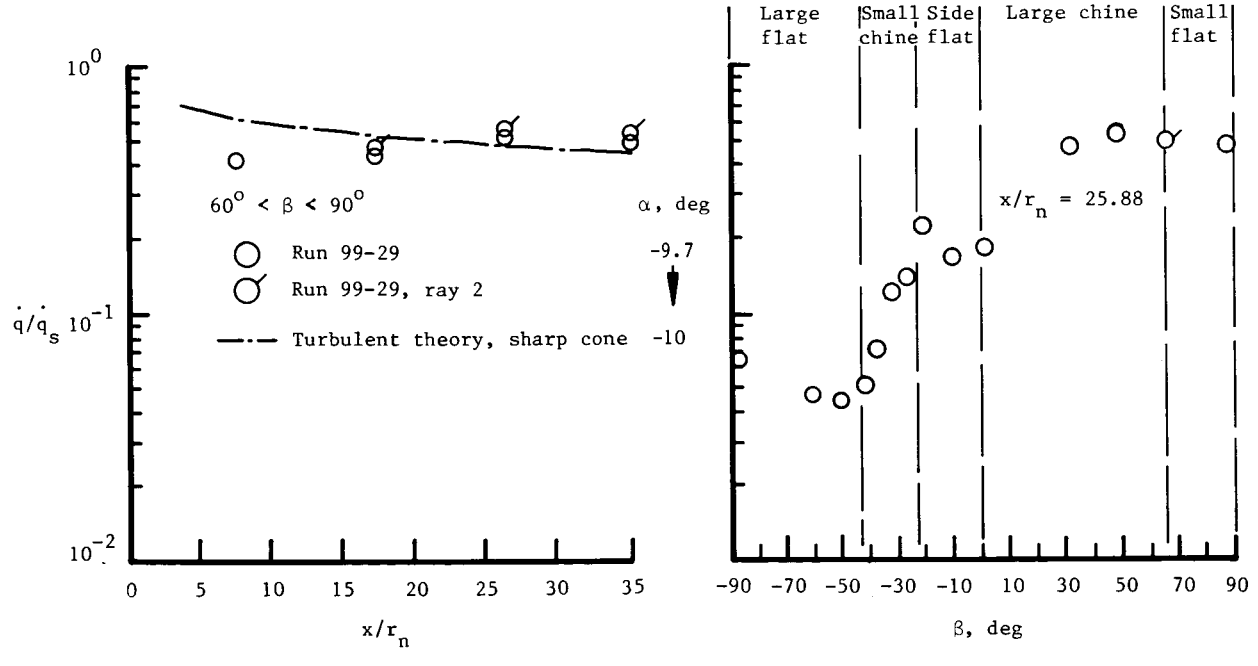

(e) $\alpha = -9.7°$.

Figure 23. Continued.

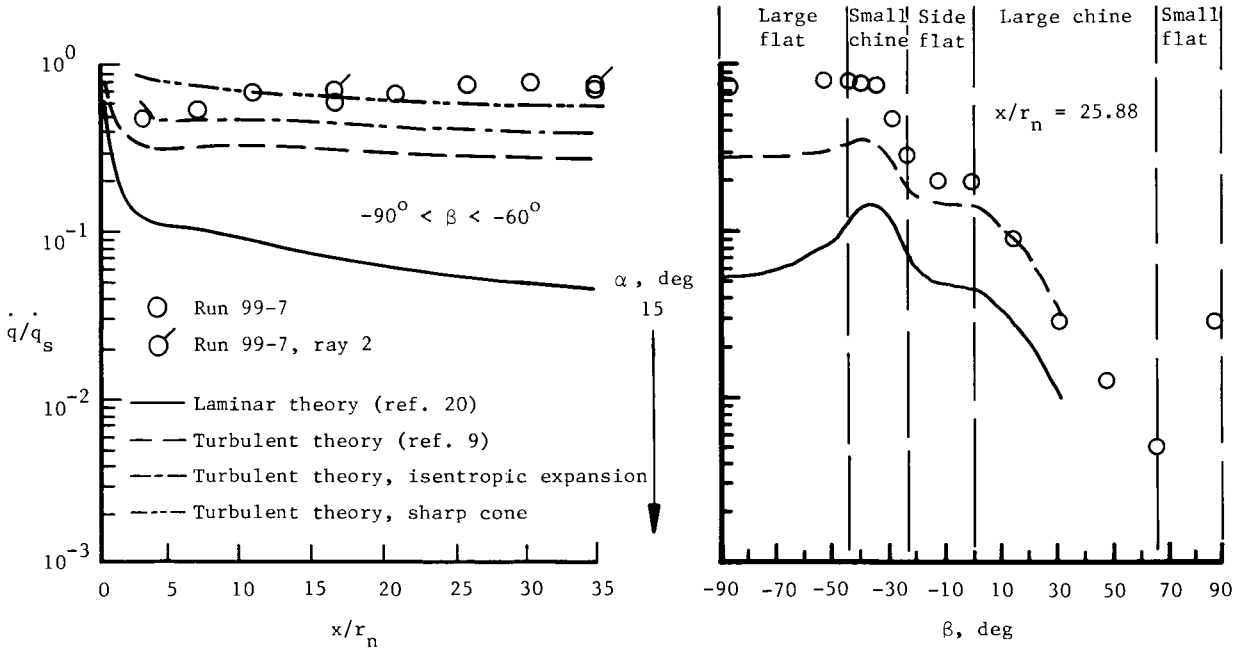

(f) $\alpha = 15.0°$.

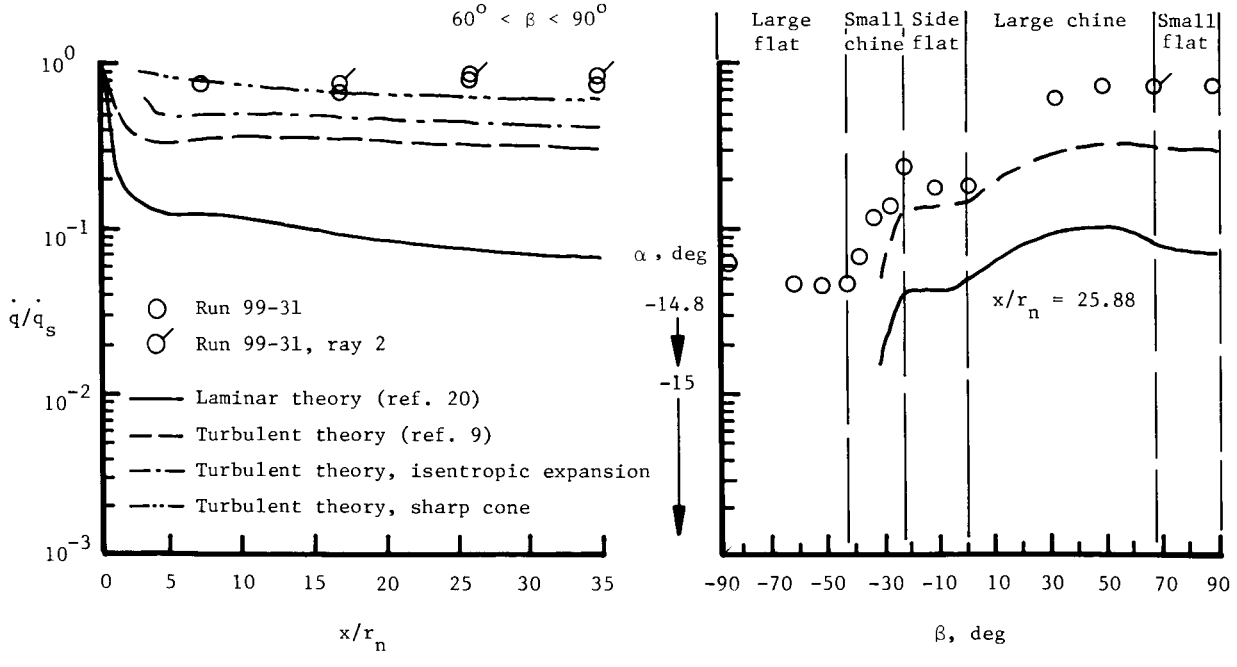

(g) $\alpha = -14.8°$.

Figure 23. Continued.

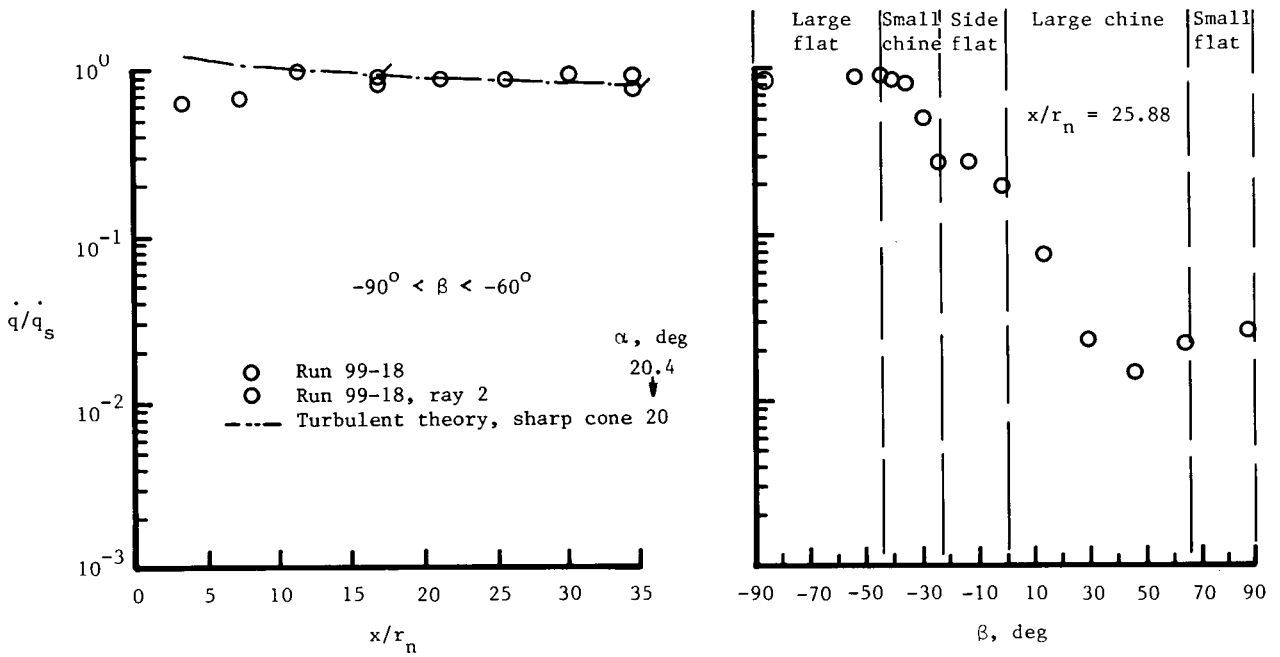

(h) $\alpha = 20.4°$.

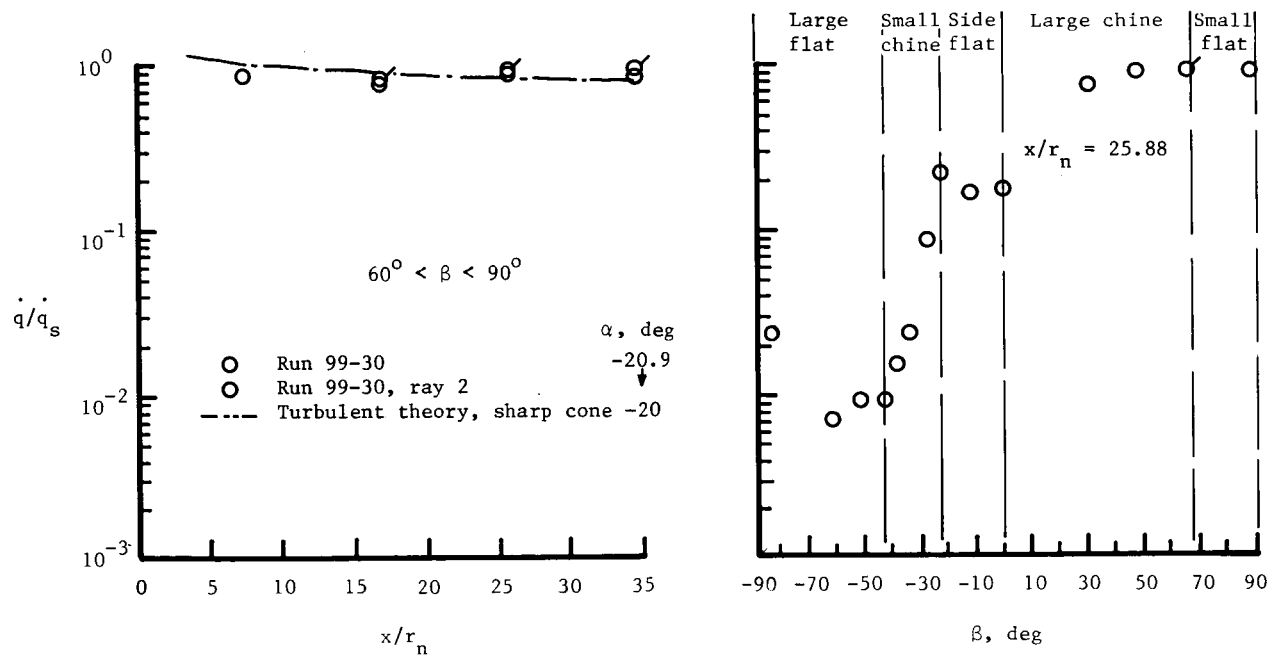

(i) $\alpha = -20.9°$.

Figure 23. Concluded.

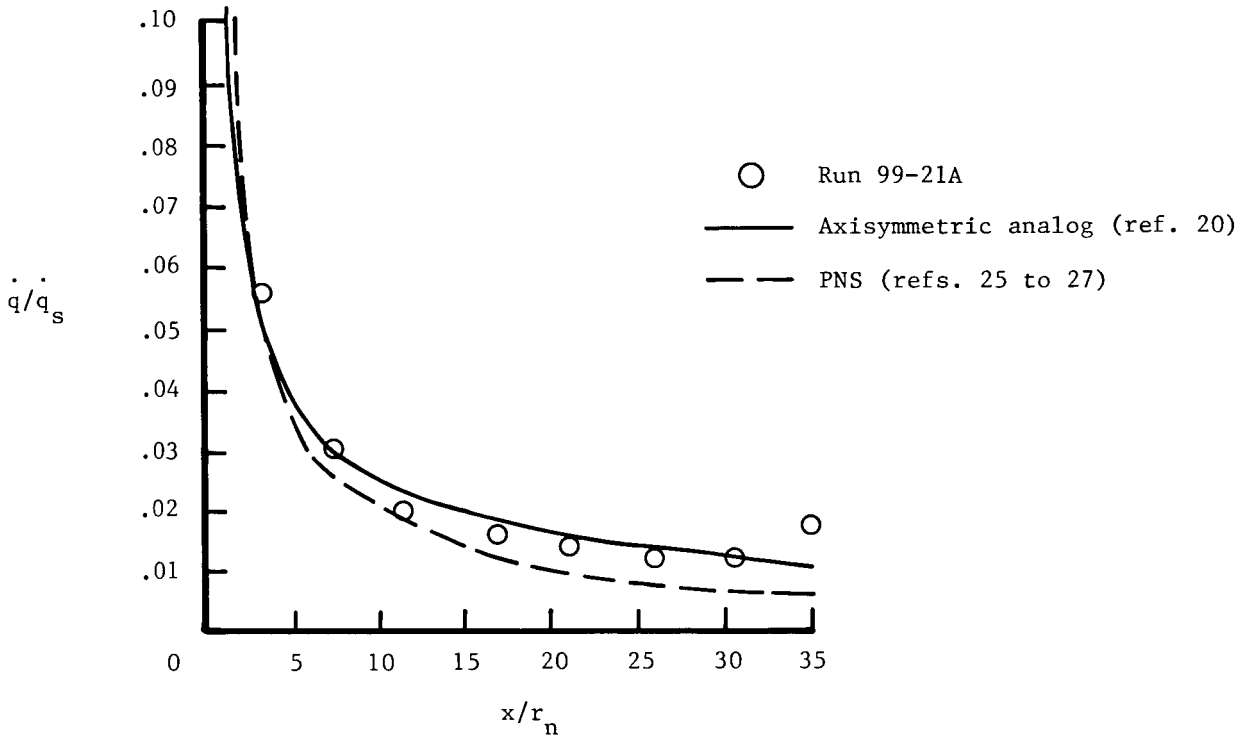

(a) $\beta = -90°$.

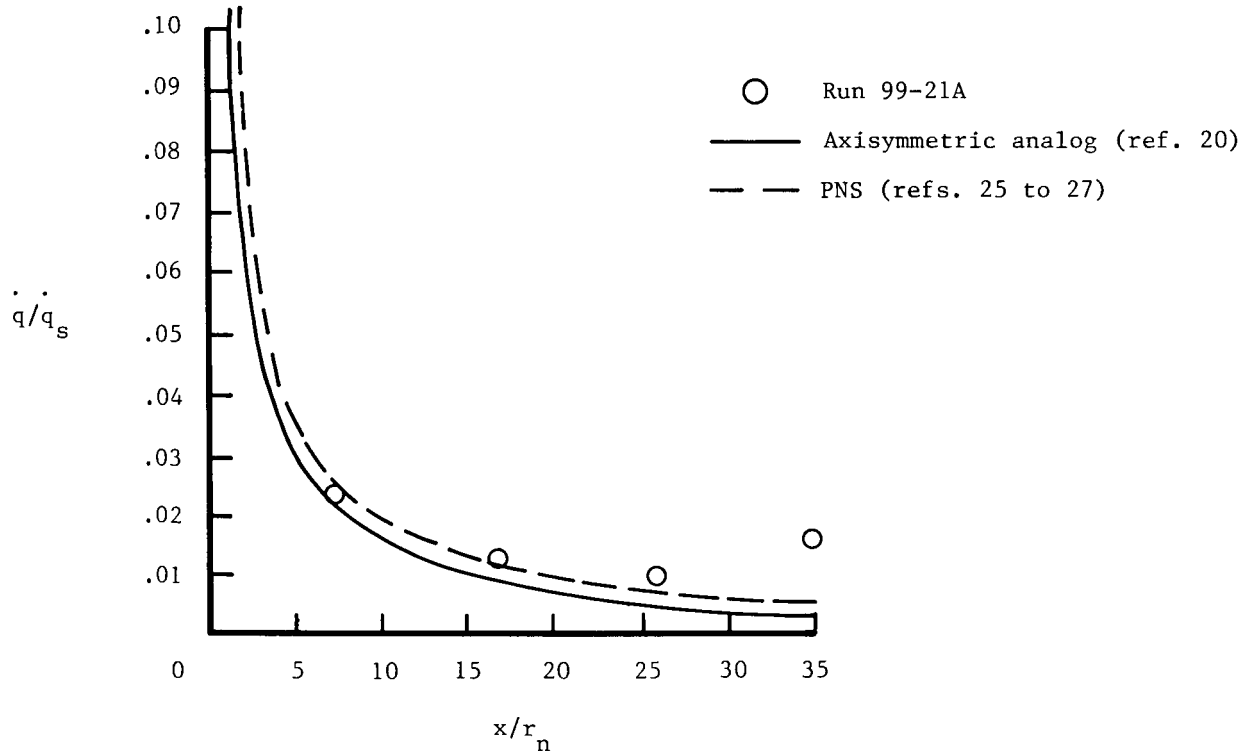

(b) $\beta = 90°$.

Figure 24. Measured and predicted laminar axial heating-rate distributions. $N_{Re} = 0.4 \times 10^6$ ft^{-1}; $\alpha = 0.4°$.

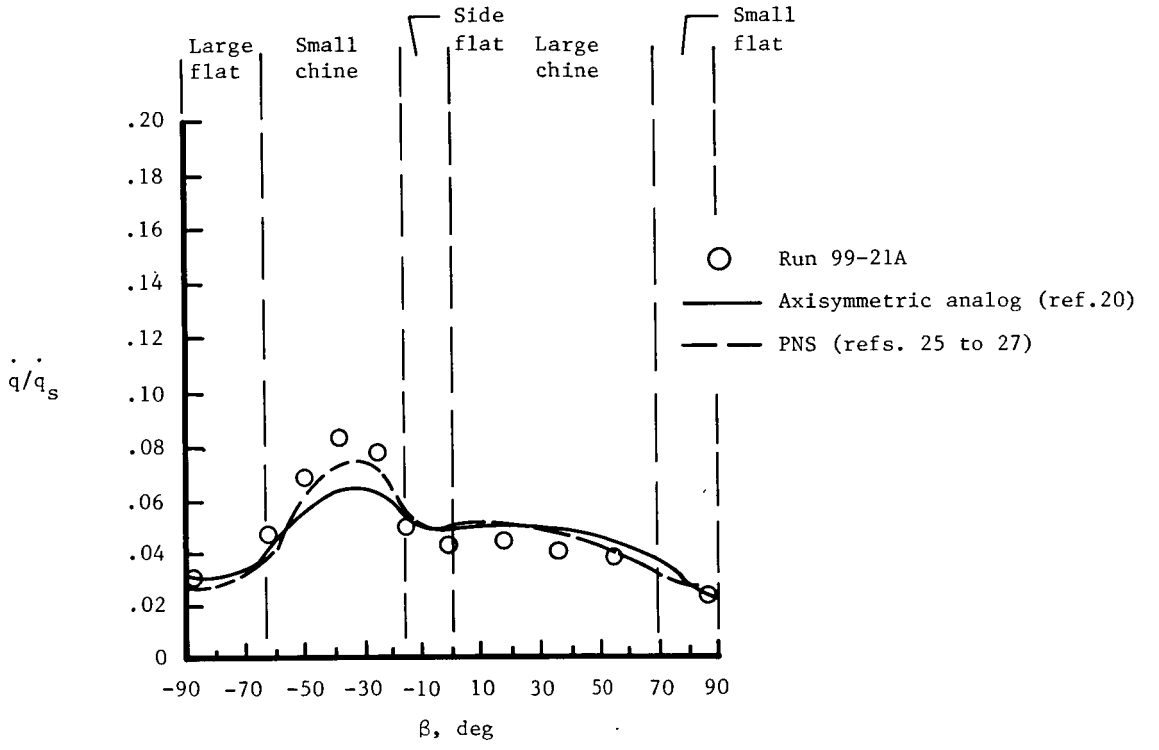

(a) $x/r_n = 7.21$.

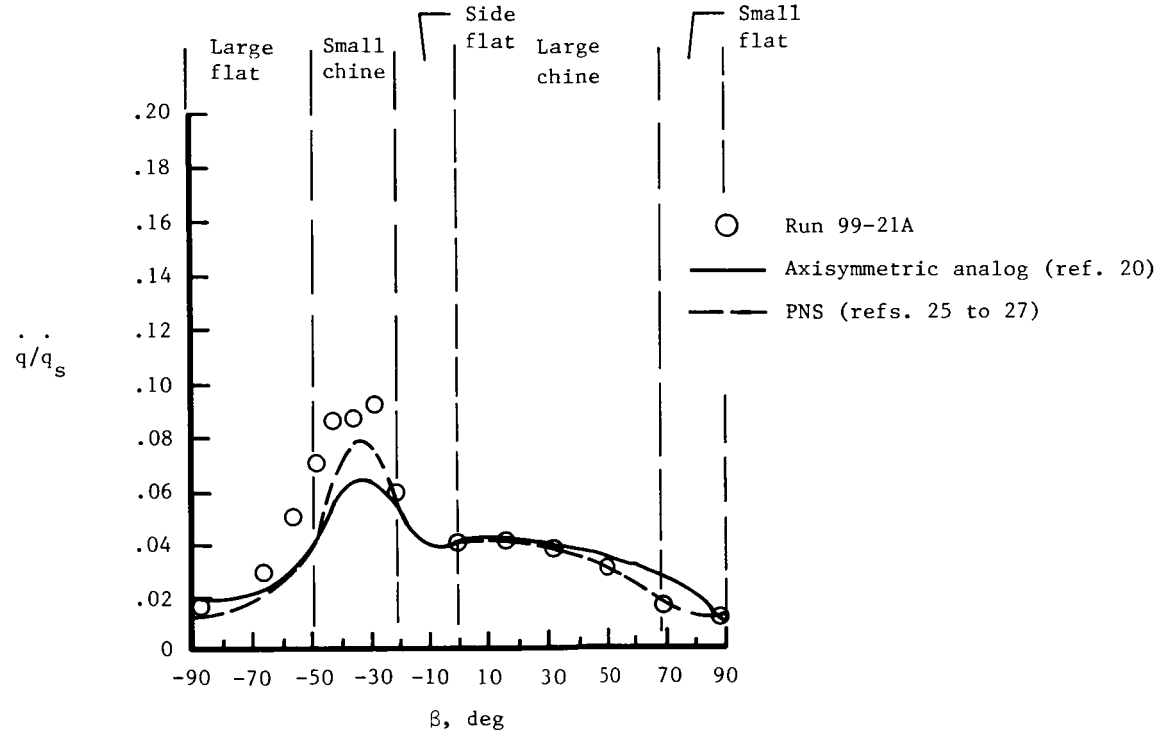

(b) $x/r_n = 16.88$.

Figure 25. Measured and predicted laminar circumferential heating-rate distributions. $N_{Re} = 0.4 \times 10^6$ ft^{-1}; $\alpha = 0.4°$.

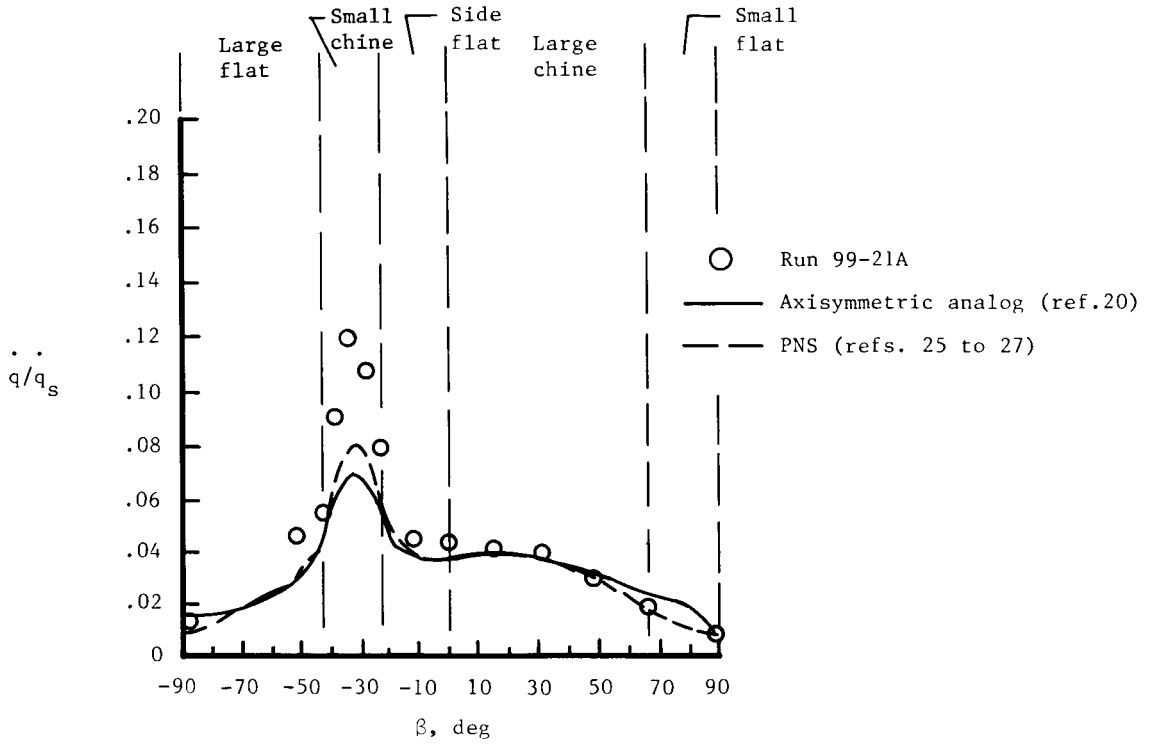

(c) $x/r_n = 25.88$.

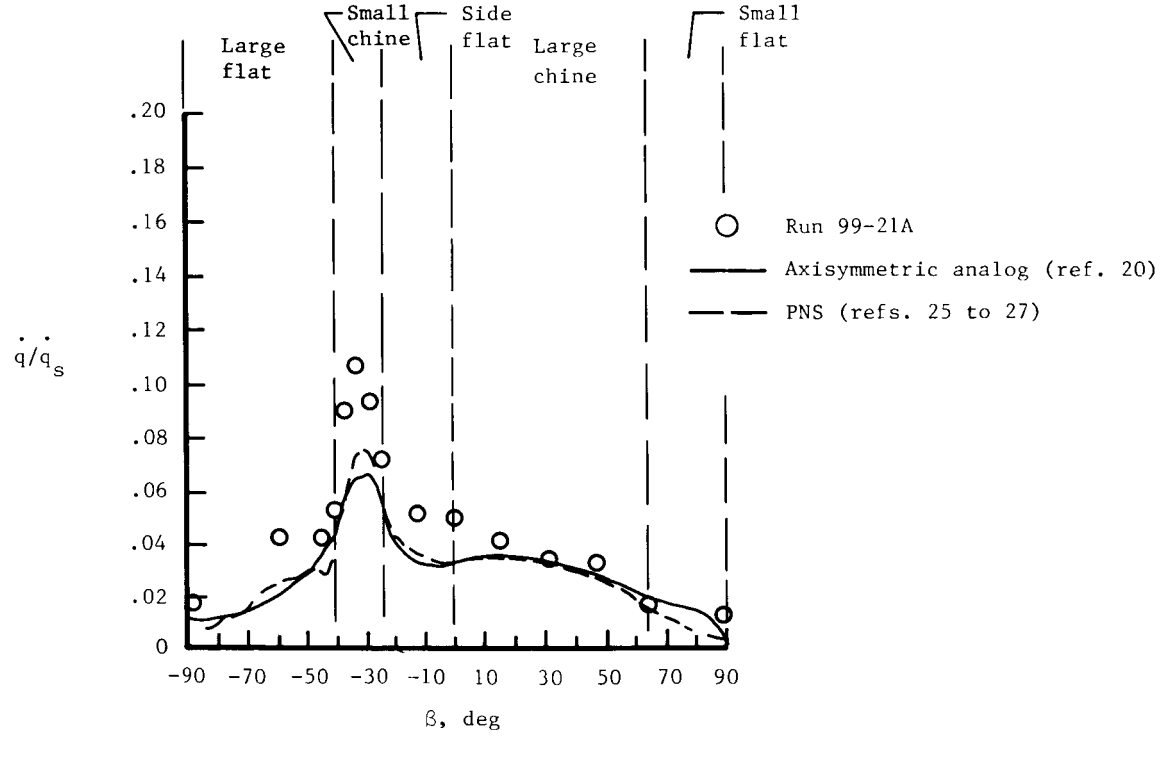

(d) $x/r_n = 34.88$.

Figure 25. Concluded.

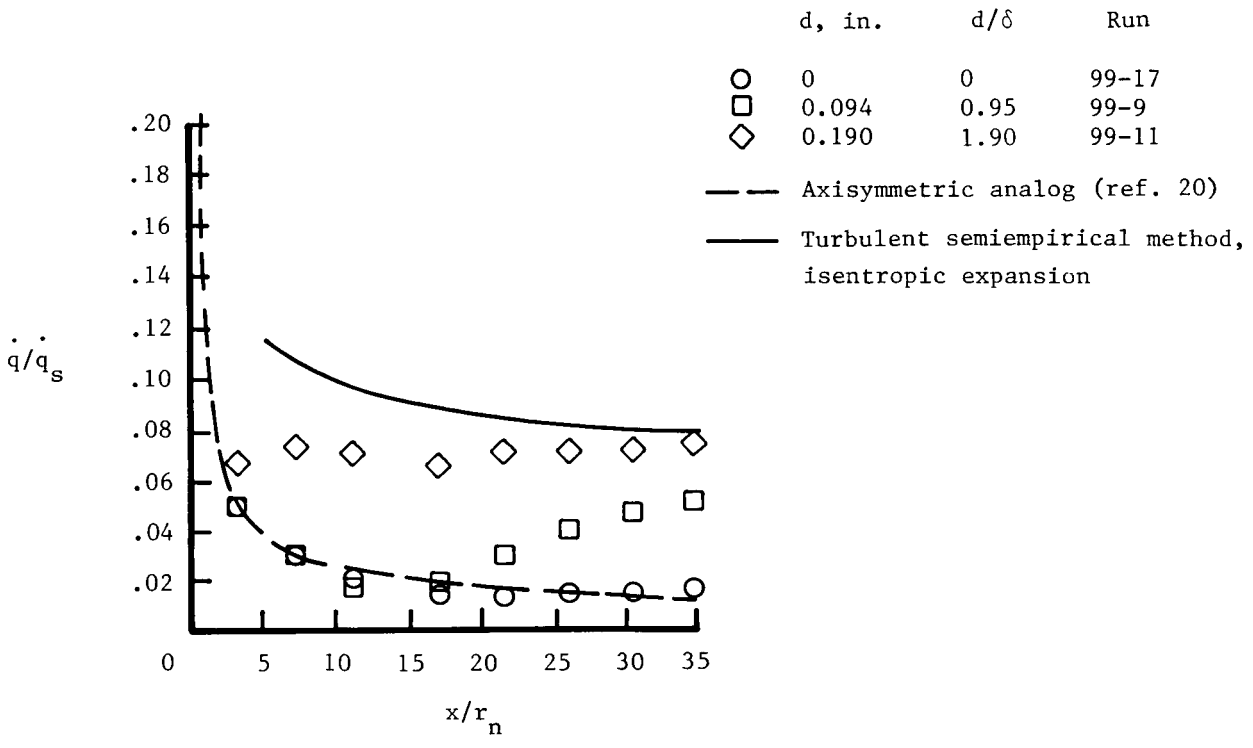

(a) $\beta \approx -90°$.

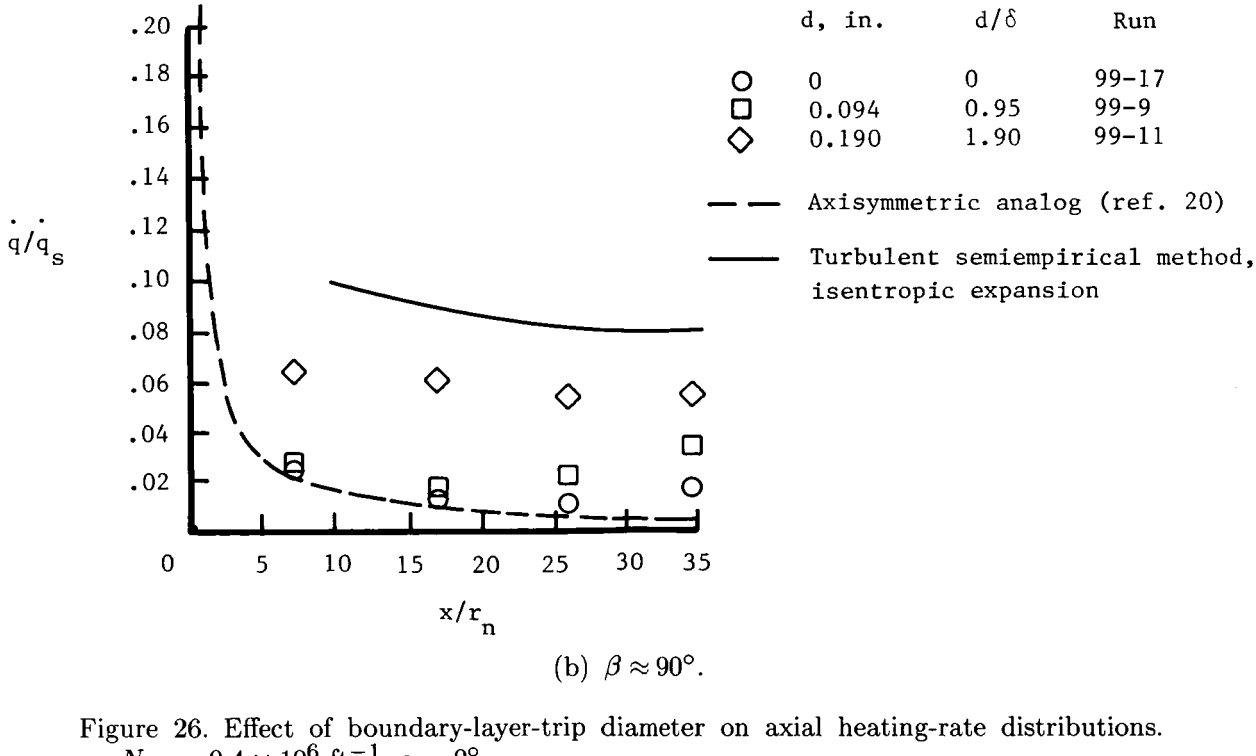

(b) $\beta \approx 90°$.

Figure 26. Effect of boundary-layer-trip diameter on axial heating-rate distributions. $N_{Re} = 0.4 \times 10^6$ ft^{-1}; $\alpha = 0°$.

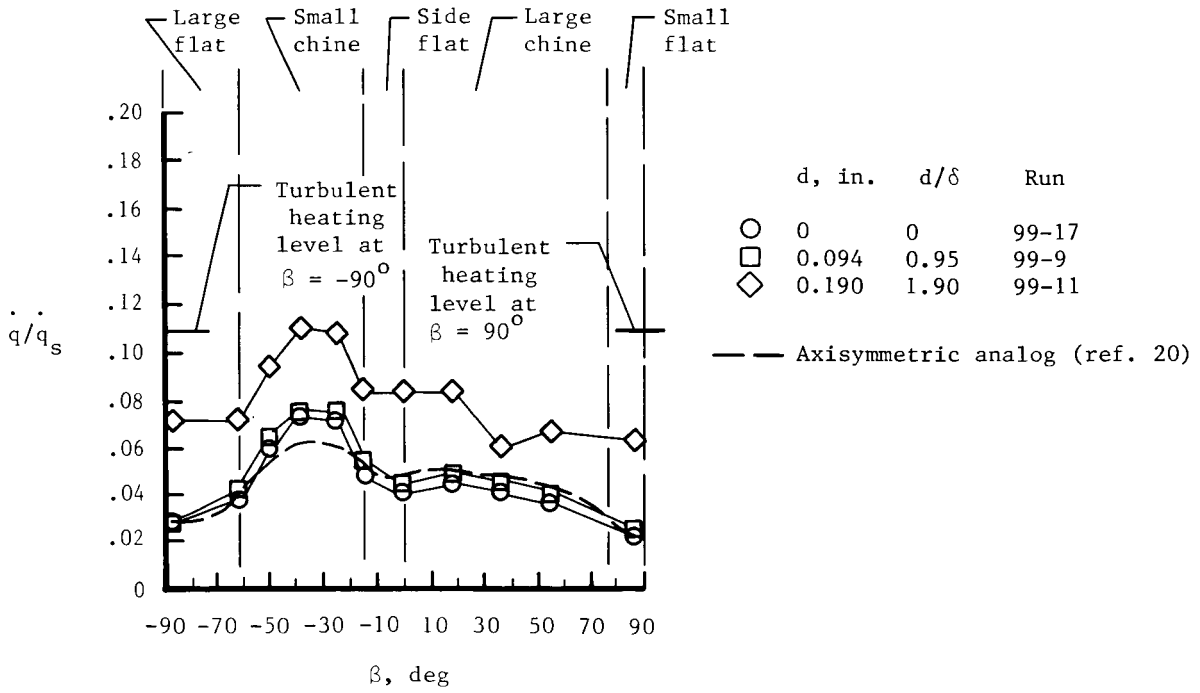

(a) $x/r_n = 7.21$.

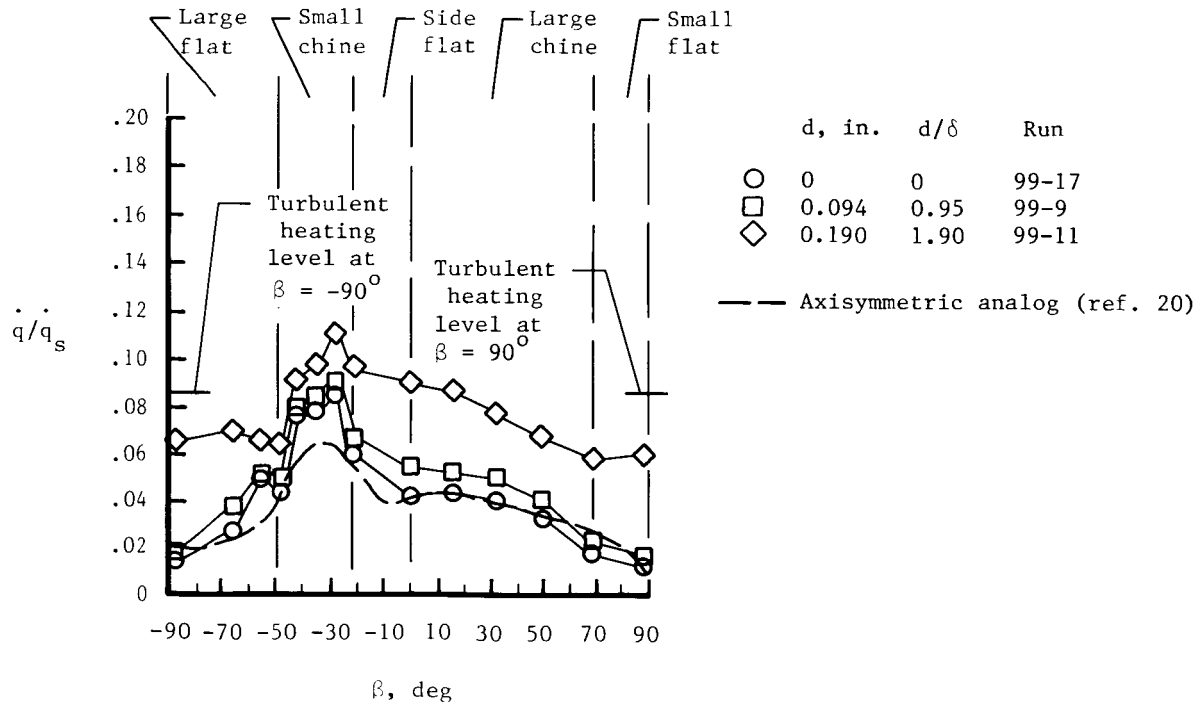

(b) $x/r_n = 16.88$.

Figure 27. Effect of boundary-layer-trip diameter on circumferential heating-rate distributions. $N_{Re} = 0.4 \times 10^6$ ft^{-1}; $\alpha = 0°$.

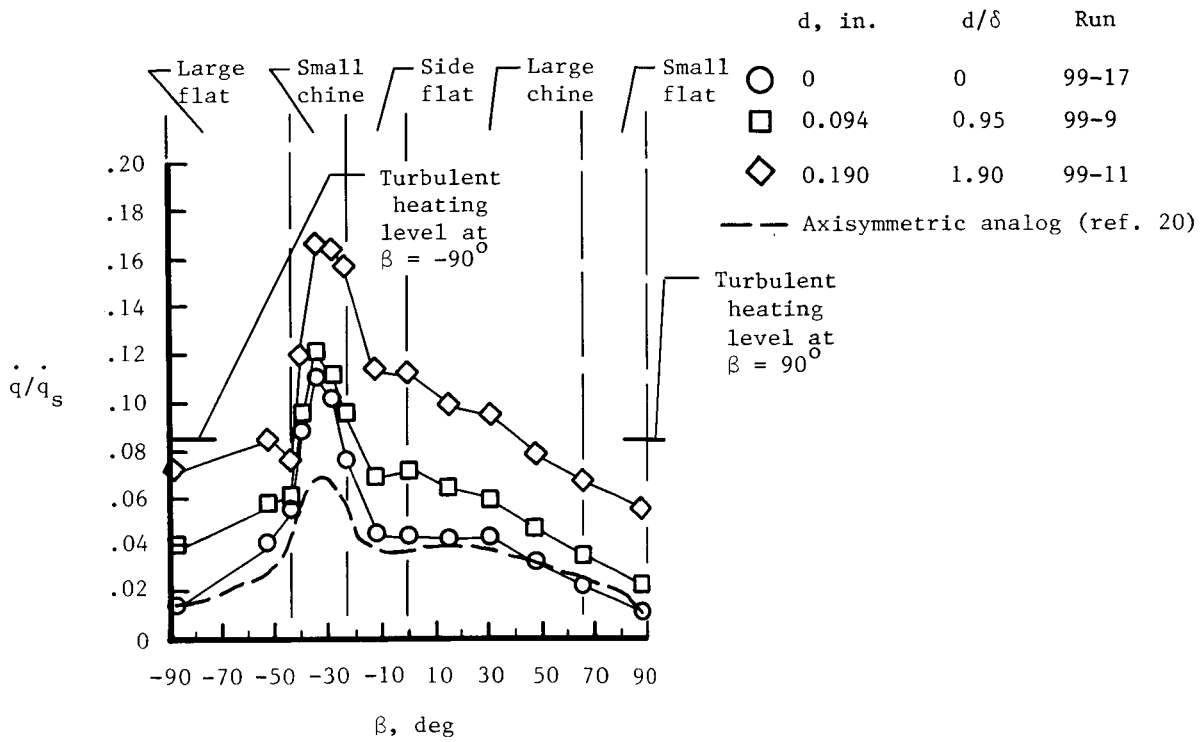

(c) $x/r_n = 25.88$.

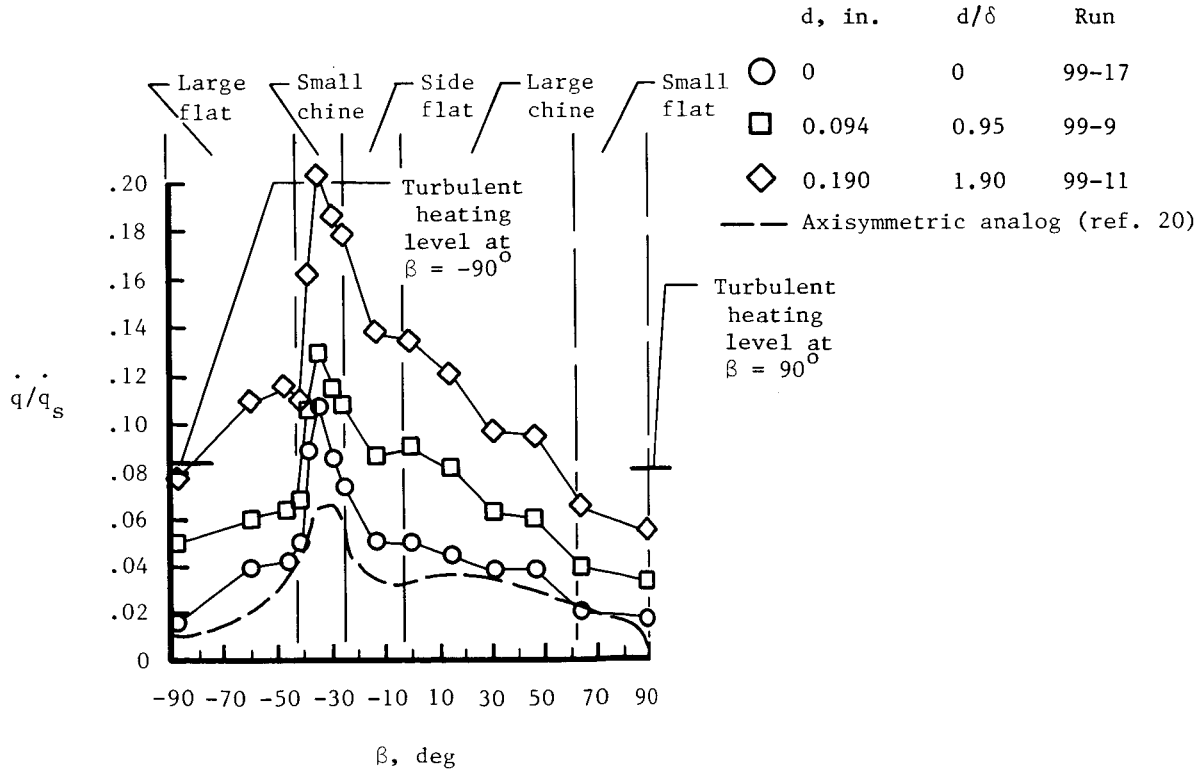

(d) $x/r_n = 34.88$.

Figure 27. Concluded.

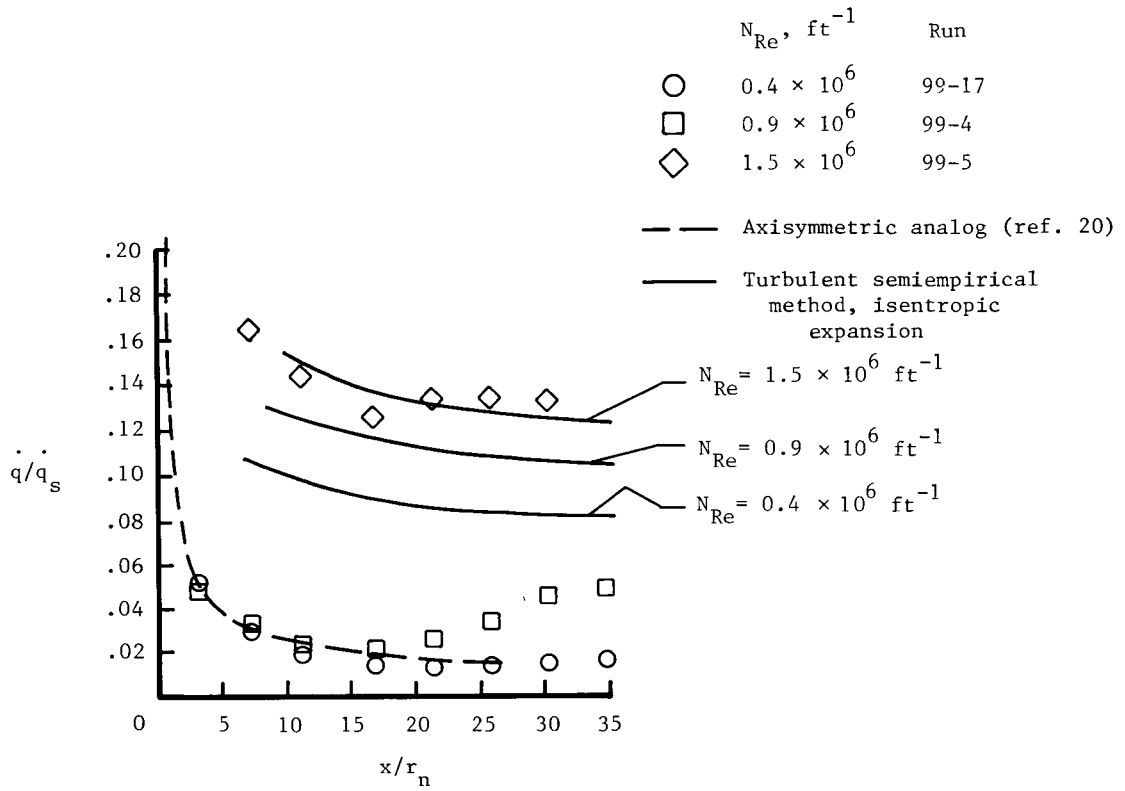

(a) $\beta \approx -90°$.

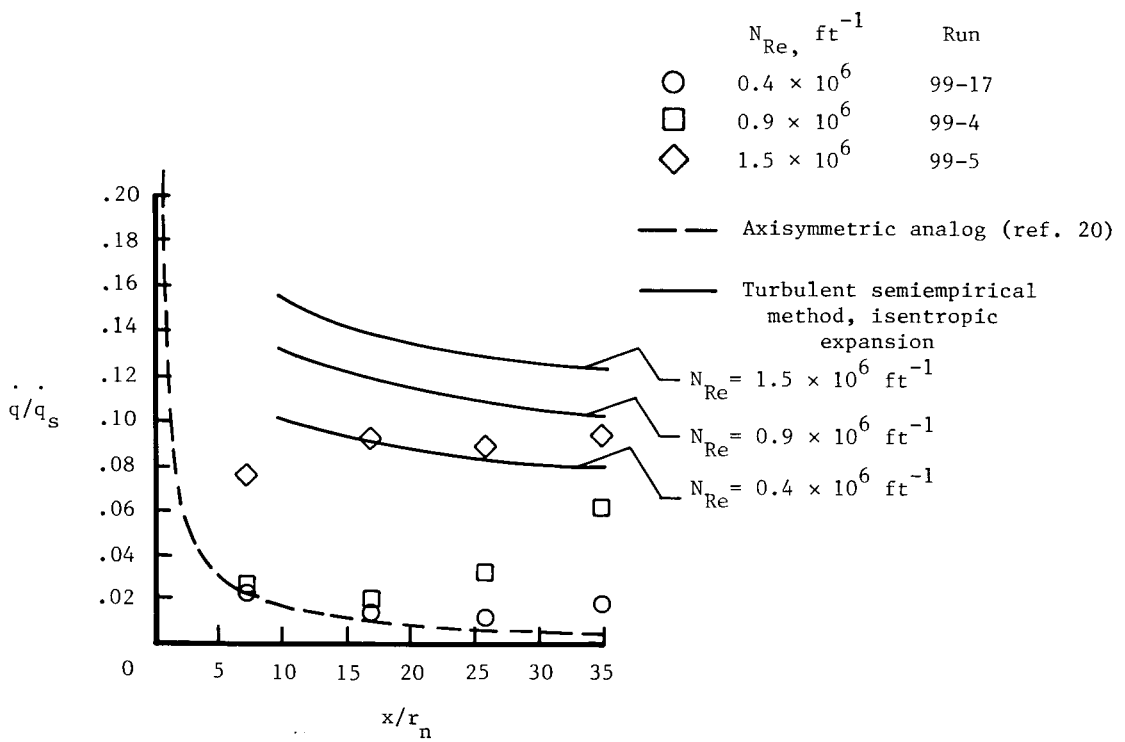

(b) $\beta \approx 90°$.

Figure 28. Effect of free-stream Reynolds number on axial heating-rate distributions. $\alpha = 0°$; no trips.

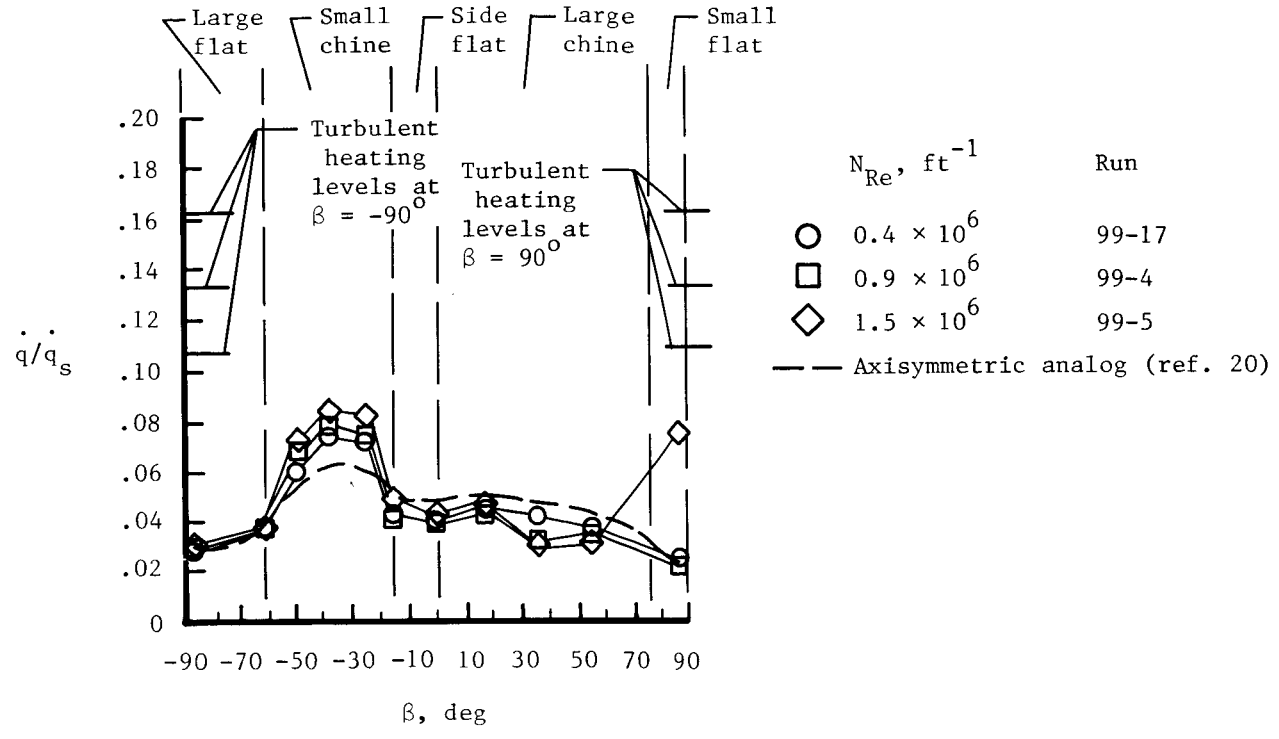

(a) $x/r_n = 7.21$.

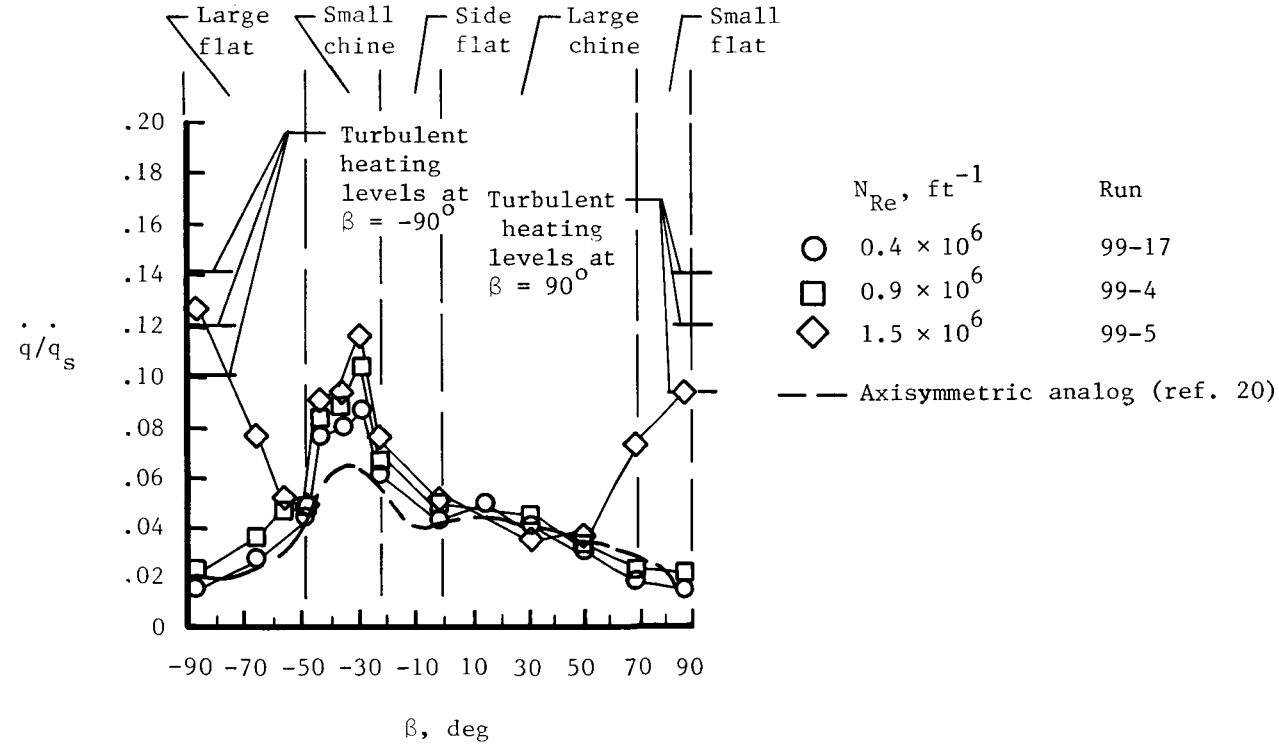

(b) $x/r_n = 16.88$.

Figure 29. Effect of free-stream Reynolds number on circumferential heating-rate distributions. $\alpha = 0°$; no trips.

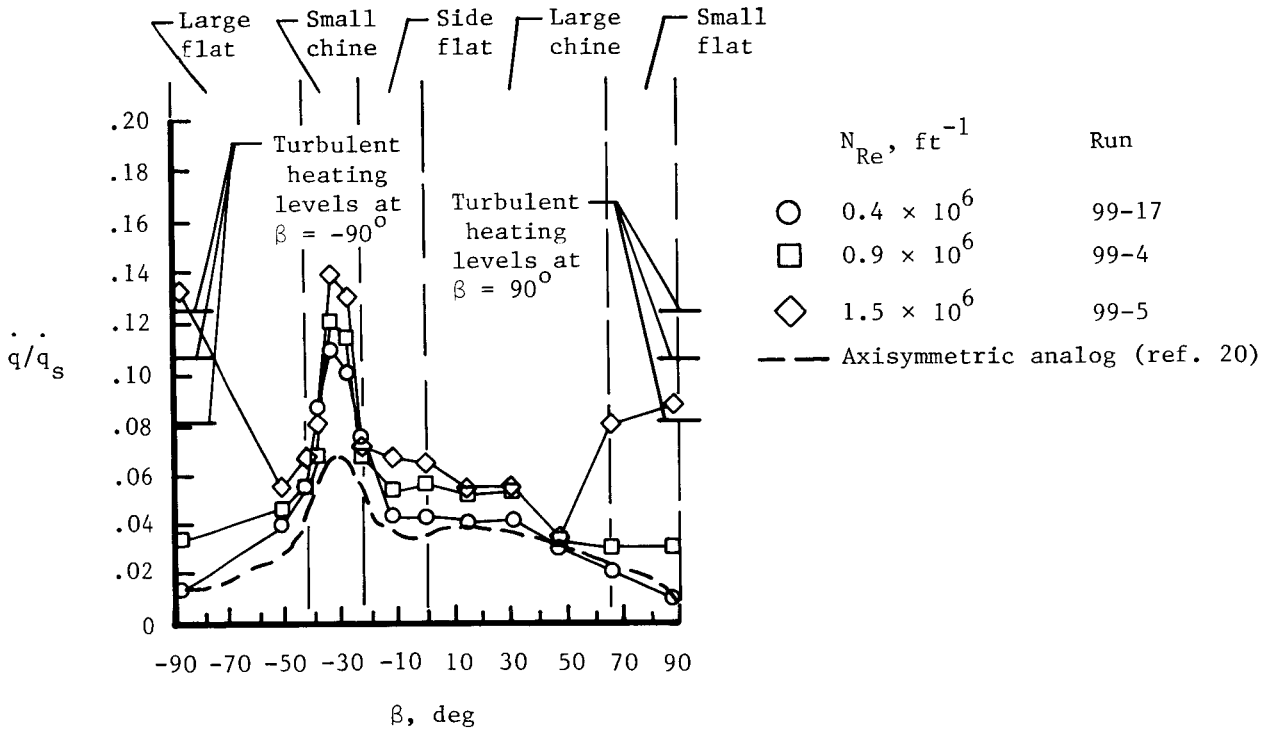

(c) $x/r_n = 25.88$.

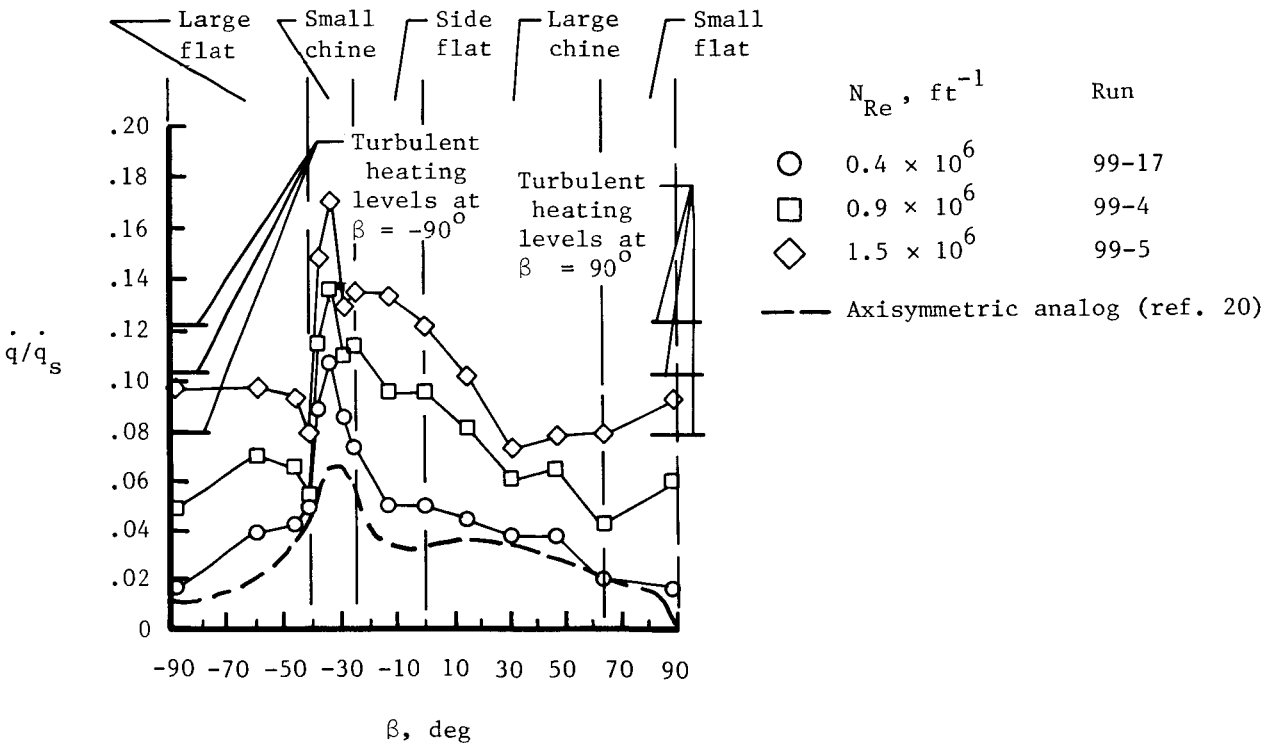

(d) $x/r_n = 34.88$.

Figure 29. Concluded.

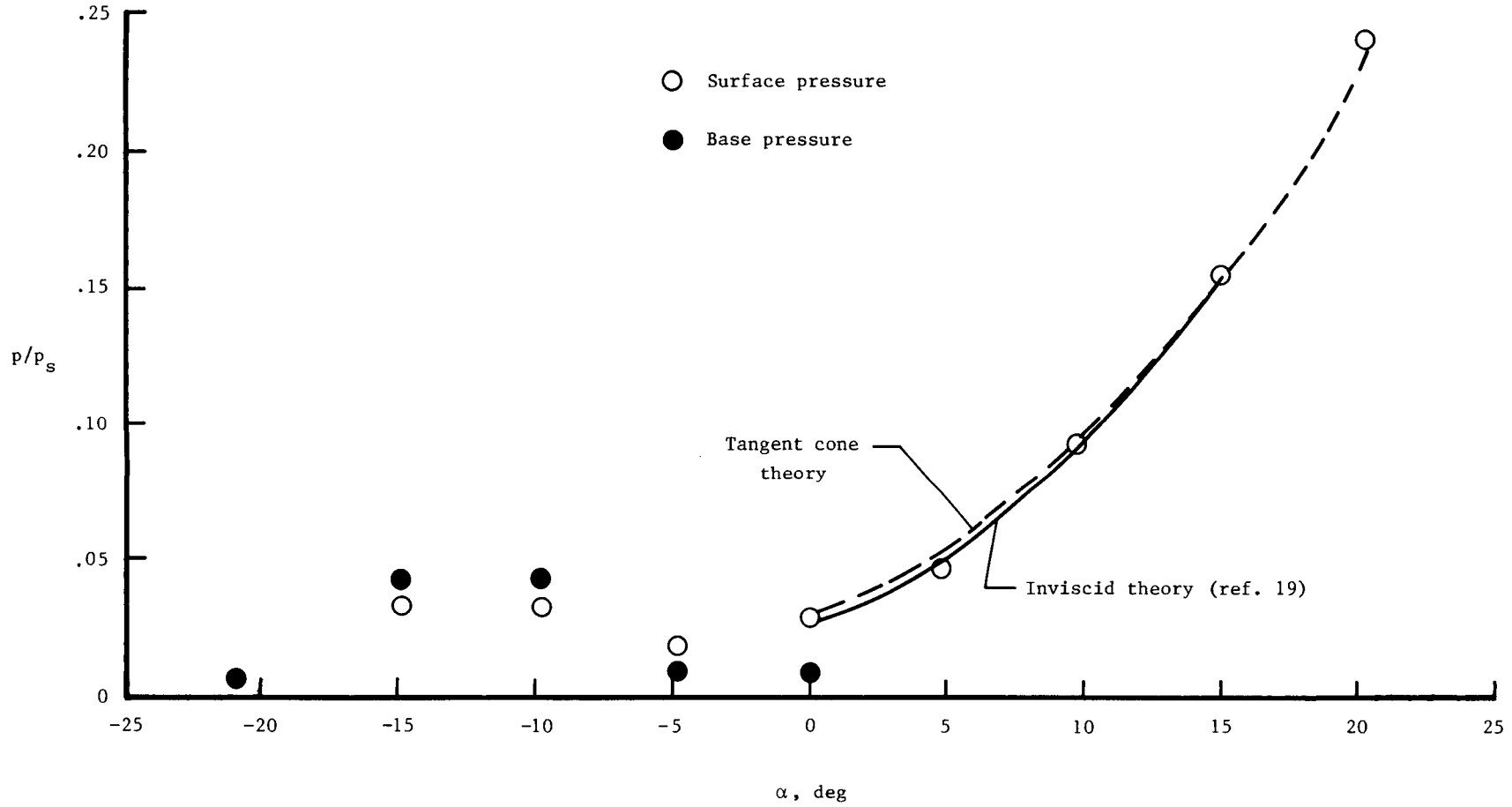

Figure 30. Effect of angle of attack on surface pressures. $x/r_n = 21.04$; $\beta = -90°$; $N_{Re} = 1.5 \times 10^6$ ft^{-1}; 0.094-in-diam trips.

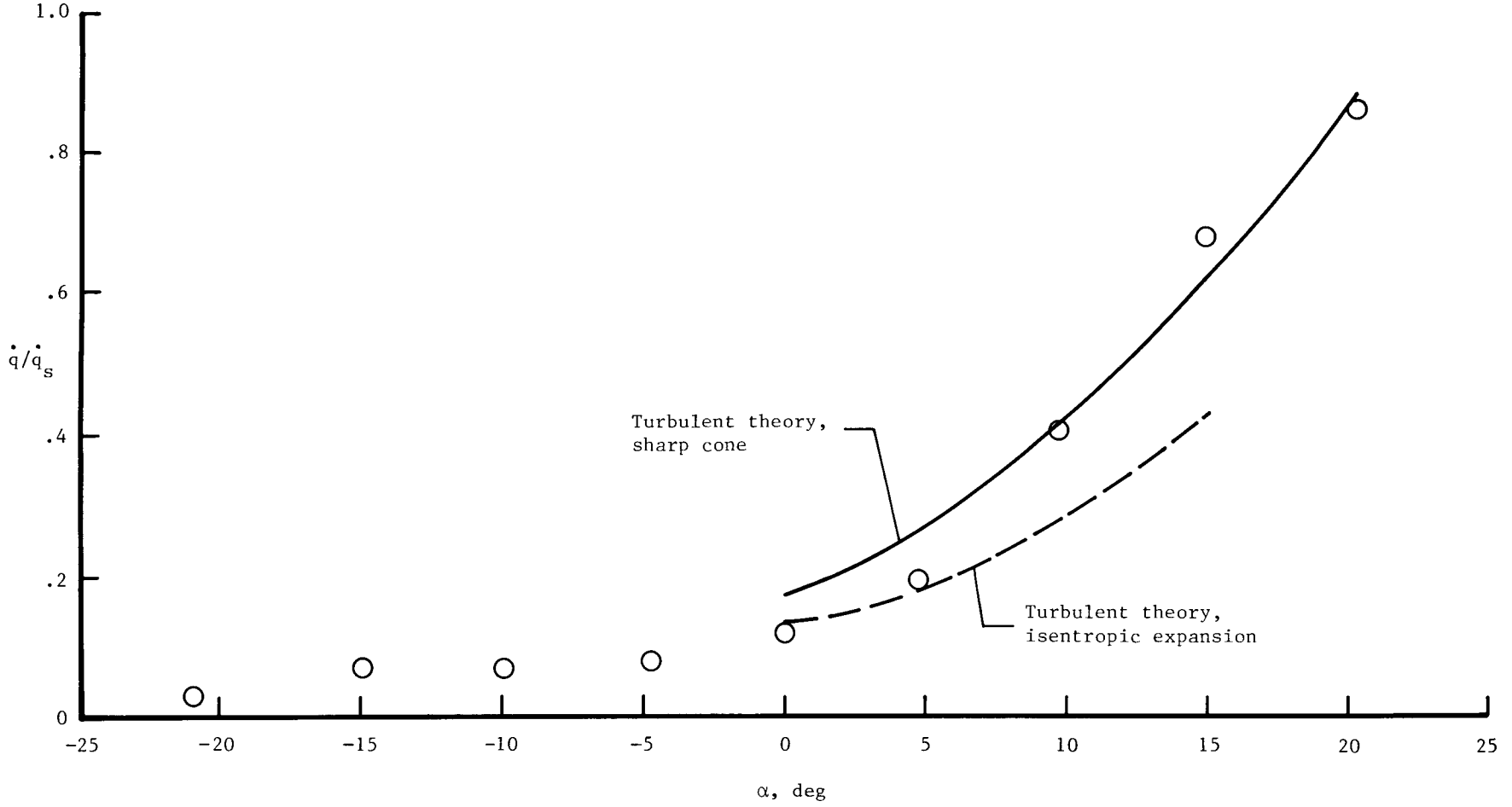

Figure 31. Effect of angle of attack on surface heating rates. $x/r_n = 21.38$; $\beta = -90°$; $N_{Re} = 1.5 \times 10^6$ ft^{-1}; 0.094-in-diam trips.

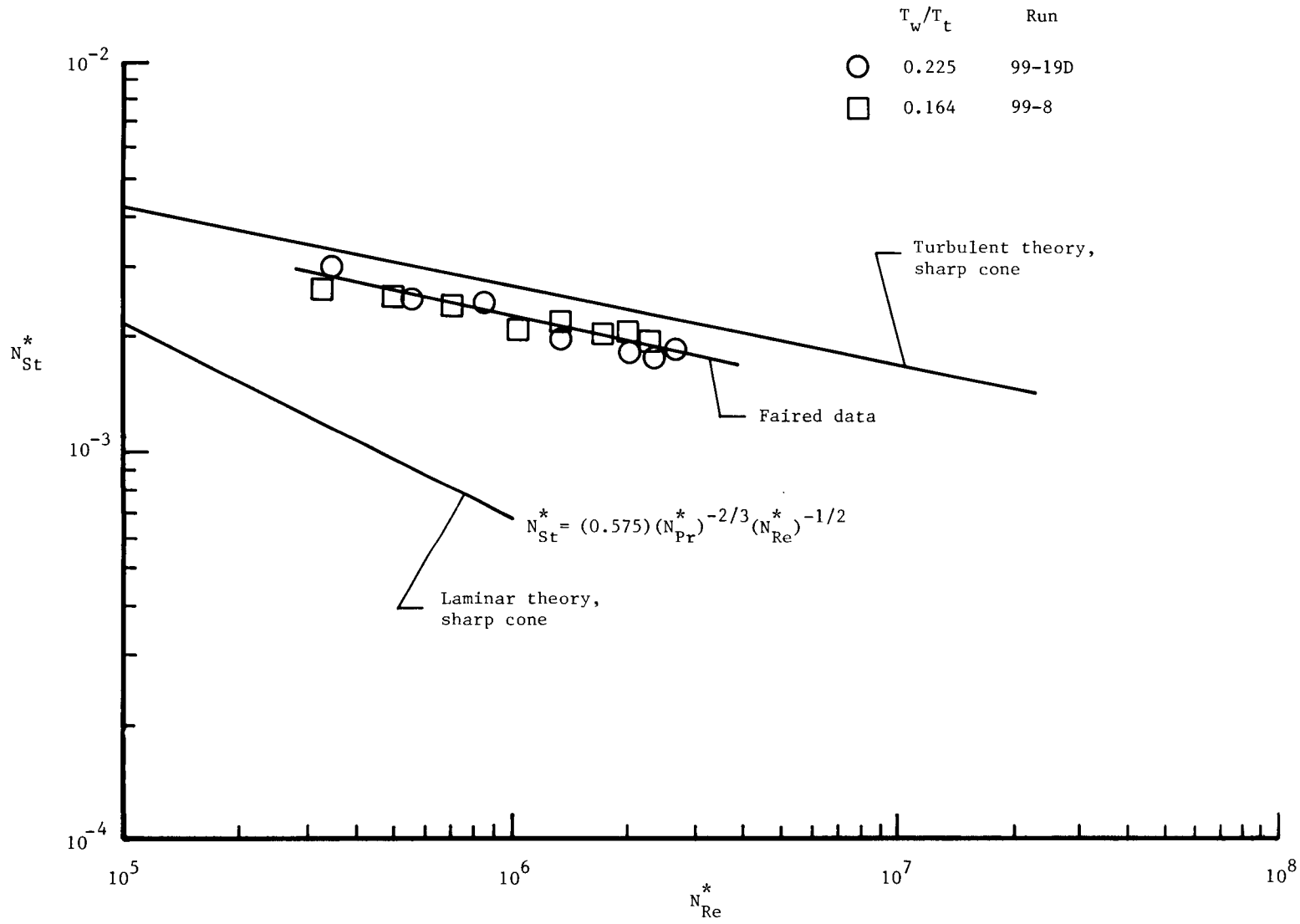

(a) Total temperature. $\alpha = 0°$; tripped boundary layer.

Figure 32. Correlation of effects of flow variables along $\beta = -90°$ symmetry line.

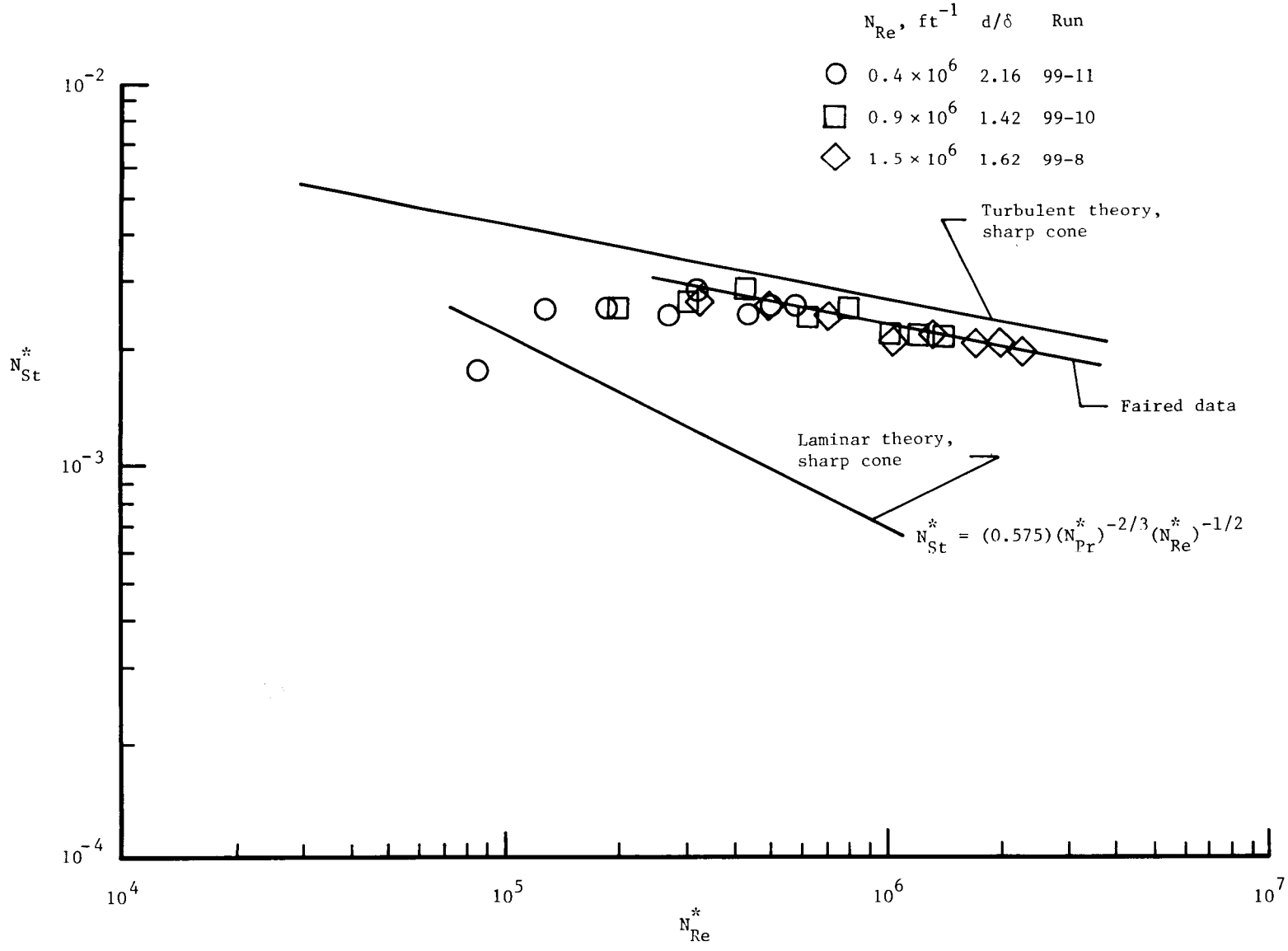

(b) Free-stream Reynolds number. $\alpha = 0°$; tripped boundary layer.

Figure 32. Continued.

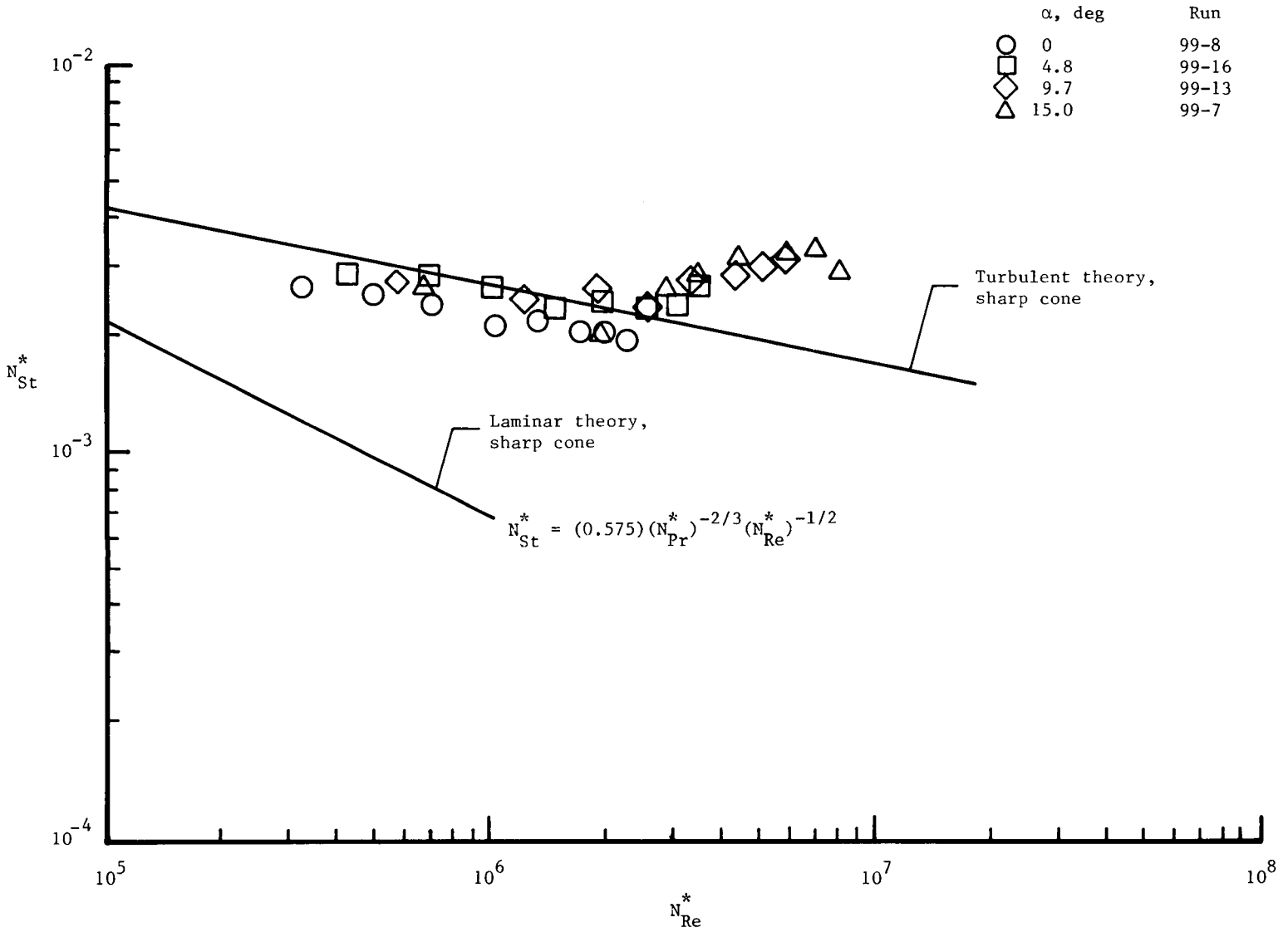

(c) Angle of attack.

Figure 32. Concluded.

Standard Bibliographic Page

1. Report No.	2. Government Accession No.	3. Recipient's Catalog No.
NASA TP-2641		

4. Title and Subtitle	5. Report Date
Aerothermal Evaluation of a Spherically Blunted Body With a Trapezoidal Cross Section in the Langley 8-Foot High-Temperature Tunnel	April 1987
	6. Performing Organization Code: 506-40-21-01
7. Author(s): Cindy W. Albertson	8. Performing Organization Report No.: L-16096
9. Performing Organization Name and Address: NASA Langley Research Center, Hampton, VA 23665-5225	10. Work Unit No.
	11. Contract or Grant No.
12. Sponsoring Agency Name and Address: National Aeronautics and Space Administration, Washington, DC 20546-0001	13. Type of Report and Period Covered: Technical Paper
	14. Sponsoring Agency Code

15. Supplementary Notes

16. Abstract

A model to be used in flow studies and curved thermal protection system (TPS) evaluations has been tested in the Langley 8-Foot High-Temperature Tunnel at a nominal Mach number of 6.8. The purposes of the study were to define the surface pressure and heating rates at high angles of attack (in support of curved metallic TPS studies) and to determine the conditions for which the model would be suitable as a test bed for aerothermal loads studies. The present study was conducted at nominal total temperatures of 2400°R and 3300°R, dynamic pressures from 2.3 to 10.9 psia, and free-stream Reynolds numbers from 0.4×10^6 to 1.7×10^6 ft^{-1}. The measurements consisted primarily of surface pressures and cold-wall (530°R) heating rates. Qualitative comparisons between predictions and data show that for this configuration, aerothermal tests should be limited to angles of attack between 10° and −10°. Outside this range, the effects of free-stream flow nonuniformity appear in the data, as a result of the long length of the model. However, for TPS testing, this is not a concern and tests can be performed at angles of attack ranging from 20° to −20°. Laminar and naturally turbulent boundary layers are available over limited ranges of conditions.

17. Key Words (Suggested by Authors(s))	18. Distribution Statement
Curved thermal protection systems Nonaxisymmetric body Laminar flow Turbulent flow Flow field predictions Pressure Heat transfer	Unclassified—Unlimited Subject Category 34

19. Security Classif.(of this report)	20. Security Classif.(of this page)	21. No. of Pages	22. Price
Unclassified	Unclassified	79	A05

For sale by the National Technical Information Service, Springfield, Virginia 22161

NASA-Langley, 1987